TRANSIENT GAS JETS INTO LIQUID

Thesis by
Jane Ming-Chin Lin

In Partial Fulfillment
of the Requirements for the Degree of
Doctor of Philosophy

California Institute of Technology
Pasadena, California

1987
(Submitted 25 July 1986)

To my parents, who taught me the value of education

ACKNOWLEDGMENTS

I would like to thank everyone who has made this research effort possible. I am indebted to Professor Bradford Sturtevant for his guidance, patience, and motivation throughout the course of the work. I would also like to thank Professor Sturtevant and Mr. Charles Sale for their invaluable editorial assistance during the preparation of this manuscript.

Finally, I am grateful to all my friends and colleagues at GALCIT for their constant encouragement and support.

This research was supported by the Department of Energy, Division of Chemical Sciences, under Project Agreement DE-AT03-80ER10634.

ABSTRACT

An experimental investigation of the development of high velocity, impulsively initiated gas jets into liquid was conducted in an effort to understand some of the physical processes that occur for a jet of very light fluid into a dense ambient atmosphere. Four gases, refrigerants 12 and 22, nitrogen, and helium were injected into water at nozzle exit Mach numbers from 1.0 to 2.2.

The study showed that a gas jet into water develops in at least three stages: startup, transition, and global steady state. The startup is characterized by bubble growth; the growth rate is well predicted by classical bubble-growth theory. Jet transition is marked by axially directed flow, which penetrates through the startup bubble and which forms a cylindrical protrusion along the axis of symmetry. A combination of strong recirculating flow and liquid entrainment causes the startup bubble to deflate and to lift off and move downstream. In the steady state, instantaneous photographs show small-scale fluctuations of the jet boundary, but time-averaged photographs show the expected conical spreading of the steady jet; the measured spreading angles range from 18-25 degrees.

However, the most significant finding of this study is that under some conditions, the gas jet into liquid never reaches the global steady state. Instead, the jet boundary exhibits chugging: large nonlinear oscillations which lead to irregular collapses of the gas column followed by explosive outward bursts of gas. The unsteadiness observed is much more violent than the familiar fluctuations typical of constant-density jets. The length scale of the motion is generally on the order of several jet diameters; the time scale is on the order of the period for bubble collapse.

It was found that the amplitude and frequency of chugging are strongly dependent on the ratio of the liquid density to the gas density, the jet Mach number, and the operating pressure ratio. The conditions under which unsteadiness occurs were determined experimentally. In particular, a quantitative measure of jet susceptibility to unsteadiness has been established. Steady jets can be achieved in two ways: by being discharged from deLaval nozzles (increasing the exit Mach number) or by being overpressured.

The unsteady behavior is modeled as the collapse of a bubble in liquid; comparisons of collapse times show good agreement. A mechanism for the unsteadiness is discussed. It is proposed that the chugging is the response of the jet boundary to a pressure difference between the jet and surrounding liquid, which arises as the result of the rapid expansion of a light fluid into a dense ambient atmosphere. The flow is shown to be similar to the discharge of a gas from a nozzle into a channel of larger cross section. An upper limit to the pressure difference is determined based on estimates of the minimum base pressure for such channel flows; a lower limit is established for the collapse time. All experimental values are within the bounds. The derived values indicate that the pressure differences between the jet and liquid may be more than 90 percent of the ambient pressure.

TABLE OF CONTENTS

LIST OF FIGURES

LIST OF TABLES

LIST OF SYMBOLS

Symbol	Description
a	Sound speed
A	Nozzle exit area
A^*	Nozzle throat area
b	Local jet width
B	Startup bubble width
c	Disturbance wavespeed, $c = c_r + ic_i$
d	Local diameter
D	Nozzle diameter
D^*	Scaled diameter, $\left[\frac{\rho_j}{\rho_a}\right]^{1/2} D$
F	Froude number, $\frac{\rho_j U_e^2}{(\rho_a - \rho_j) g D}$
h	Height of secondary jet
H	Startup bubble height or jet pinchoff location
J	Momentum, ρU_e^2
k	Wavenumber
L	Duct length
M	Mach number
M_e	Exit Mach number
M_s	Shock Mach number
n	Mode
N	Pulse width
P	Pressure
P_1	Pressure measured upstream of nozzle throat
P_2	Pressure measured in water near nozzle exit
P_o	Gas reservoir pressure
P_o^*	Reservoir pressure at pressure-matched condition

$\bar{P}_o$ Normalized operating pressure ratio, $\frac{P_o}{P_o^*}$, (Figure 4.13)

P_w Base pressure

$\bar{P}_w$ Normalized base pressure, $\frac{P_w}{P_o}$

ΔP Pressure difference, $P_a - P_b$

r Radial coordinate

r_1 Radial distance from pressure transducer to bubble boundary

R Nozzle radius

Re Reynolds number, $\frac{U_e D}{\nu}$

T Experimental run time

t Time

t_b Bubble collapse time, Equation (4.4)

t_j Visually measured jet collapse time

t_w Jet collapse time based on $(P_w)_{min}$

Δt Time increment from Equation (4.2)

U Velocity

W Channel width

Wb Weber number, $\frac{\rho U_e^2 D}{\sigma}$

x Axial coordinate

Y Nondimensional frequency from spatial stability analysis, $\frac{\omega R}{U}$

z Nondimensional wavespeed and amplification rate from temporal stability analysis, $\frac{c_r}{U} + i\frac{c_i}{U}$

α Diffusion angle, full angle

β Density ratio, $\frac{\rho_a}{\rho_j}$

χ Nondimensional wavenumber from temporal and spatial stability analyses, αR

γ Ratio of specific heats

Γ Intermittency, defined in Equation (4.2)

ρ Density

ν Kinematic viscosity

ω Frequency

ϕ Ratio of nozzle area to duct cross-sectional area, $\left(\frac{D}{W}\right)^2$

σ Surface tension coefficient

ξ Defined in Equations (A.1b), (A.1c), (A.2b), and (A.2c)

Subscripts

a Ambient

b Bubble

c Centerline

e Nozzle exit

g Gas

i Imaginary part of a complex variable

j Jet

l Liquid

o Reservoir

r Real part of a complex variable

Chapter 1
INTRODUCTION

1.1. Motivation.

The present work is an experimental investigation of the transient behavior of impulsively initiated high velocity gas jets into liquid. The objectives of this study are (i) to classify the stages of development from initiation to steady state, (ii) to identify the mechanism responsible for unsteady behavior in the jet initial region, and (iii) to investigate the effects of gas density, Mach number, and operating conditions on the jet behavior.

This study was motivated by the desire to understand the behavior and the physical processes that occur for an impulsively initiated jet of very light fluid into a dense ambient atmosphere. Currently, there is no quantitative and detailed theory of high momentum gas jets into water, yet such two-phase jets occur frequently in industry and in nature. Most studies of jets, such as those by Abramovich (1963) and Squire & Trouncer (1944), have dealt mainly with single-phase homogeneous fluid systems. For a two-phase system, such as a gas jet into liquid, the ratio of the ambient fluid density to jet fluid density may be two orders of magnitude larger than that for a single-phase system. Thus, it would not be surprising if the two systems behaved quite differently. For example, a jet of gas into liquid may exhibit characteristics representative of both jet and bubbling processes.

Previous work on the discharge of gas into liquid has shown that the flow may be classified into three regimes: bubbling, irregular bubbling, and jet. The governing parameters for the regimes are the Reynolds number, the Froude number, and the Weber number, to account for the effects of viscosity, buoyancy, and surface tension, respectively. They are defined as

$$Re = \frac{U_e D}{\nu}$$

$$Fr = \frac{\rho_j U_e^2}{(\rho_a - \rho_j) g D}$$

$$Wb = \frac{\rho_j U_e^2 D}{\sigma},$$

where U_e is the jet exit velocity, D is the nozzle diameter, ρ_a and ρ_j are the ambient and jet densities, ν is the kinematic viscosity of the gas, and σ is the surface tension coefficient. Two additional dimensionless parameters of significance are the density ratio, ρ_a/ρ_j, and the operating pressure, P_o/P_a (i.e., the ratio of the gas reservoir pressure to the ambient pressure). For gas/liquid systems, ρ_a/ρ_j is much greater than one. The Mach number, which is a measure of the momentum flux, follows from a combination of the gas density, the pressure, and the equation of state. Table 1.1 shows qualitatively the range of dimensionless parameters characterizing the three regimes.

Table 1.1. Flow Regimes of Gas into Liquid

Regime	Re	Fr	Wb	M_e
Bubbling	low	low	low	$\ll 1$
Irreg Bubbling	interm	interm	interm-high	< 1
Jet	high	high	high	≥ 1

References: Jackson(1964), Calderbank(1956), Leibson et al.(1956), Tross(1974), Bell et al.(1972).

The Mach number is more appropriately used in the jet regime where Re, Fr, and Wb are large and the effects of viscosity, buoyancy, and surface tension are negligible. This latter regime is the area of interest for the present work.

In the bubbling regime, changes in Re, Fr, and Wb have significant effects on the flow behavior. In this regime, the gas flow rates are low, and bubbling occurs. From an upward pointing nozzle, single spherical bubbles or trains of bubbles are generated and detach from the exit. Bubbles are generated at an orifice because the buoyancy force increases as the size of the bubble increases, until eventually, the bubble rises above the orifice and pinches off. The emphasis of the studies in this area has been on predicting the size and frequency of bubble formation as a function of flow rate. Jackson (1964) reviewed the literature in this field and has shown that the phenomenon of bubble formation is quite complicated. The bubbling process is influenced strongly by the properties of both the liquid and the gas supply.

In the irregular bubbling regime, changes in Re, Fr, and Wb still have significant effects on the flow behavior. The flow rate of the gas from the orifice is typically subsonic. The bubbles formed at the orifice are not spherical, and the sizes are independent of the orifice diameter. The bubbles coalesce close to the exit plane, take on an irregular elongated shape, and quickly break up into smaller bubbles of various sizes. These irregular bubbles form an apparent "jet," which was observed and photographically documented by Calderbank (1956) and Leibson et al. (1956).

In the jet regime, changes in Re, Fr, and Wb no longer have significant effects on flow behavior, and Mach number is the only remaining parameter that can cause changes in the flow. Few researchers have examined the flow behavior in this regime, and currently, a detailed and quantitative theory does not exist. The investigations that have

been made can be divided into two subcategories: reactive and nonreactive systems. The present work is concerned with the latter category. The reactive case involves flow with condensation, such as steam into water (Kerney et al., 1972; Kiceniuk, 1952), or flow with chemical reaction, such as chlorine into molten sodium (Igwe et al., 1973; Themelis et al., 1969). A nonreactive system involves gas discharge into liquid without phase change or chemical reaction. Studies of nonreactive systems have emphasized measurements of the mean flow properties in the far field of the fully developed jet. Up until the work presented in this thesis, the various stages of jet development, such as the startup and transition, evidently had not been explored.

1.2. Outline of Present Work.

In this study, high velocity submerged gas jets were discharged impulsively into water, allowed to develop and reach a quasi-steady state. Impulsive discharge means that the time scale for the initial pressure increase at the start the of flow is much shorter than the time scale for the gas flow or for the jet growth. The jet momentum flux was so great that buoyancy and viscosity effects were negligible. Surface tension was also negligible except at length scales much smaller than the jet diameter. High-speed photography and fast-response transducers were used to document the features of the different stages of jet development.

The study showed that a gas jet into water develops in at least three stages: startup, transition, and global steady state. The startup is characterized by bubble growth, where the directed momentum to the liquid is small and the gas motion is radially outward. The growth rate is reasonably well predicted by classical bubble-growth theory. The transition is marked by axially directed flow, which penetrates through the startup bubble and which forms a cylindrical protrusion along the axis of symmetry. It is found that as the jet grows, a combination of strong recirculating flow and entrainment

causes the startup bubble to deflate and to lift off and move downstream. In the steady state, the gas flow is steady and the jet spreads smoothly from the nozzle. Instantaneous photographs show small-scale fluctuations of the jet boundary, but time-averaged photographs show the expected conical spreading of the jet; the measured spreading angles range from 18-25 degrees.

However, the most significant result of this study was that under some conditions, a gas jet into liquid never reaches a quasi-steady state; instead, "chugging" occurs. While chugging is commonly associated with strong oscillations of the source reservoir, in this study, this is not the case. Here, chugging is the result of an instability of the jet boundary; the reservoir pressure remains steady. Chugging is a large nonlinear oscillation of the jet which lead to the irregular collapse of the gas column followed by an explosive outward burst of gas. This unsteady behavior is much more violent than the familiar fluctuations typical of constant-density jets. The length scale of the unsteady motion is generally on the order of several jet diameters; the time scale is on the order of bubble collapse times.

It is speculated that the unsteadiness is the response of the jet boundary to a pressure difference between the jet and ambient fluids. The pressure difference arises from the rapid expansion of a light fluid into a heavier one. The flow is shown to be similar to the discharge of a gas from a nozzle into a channel of larger cross section. An upper limit for the pressure difference was determined based on estimates of the minimum base pressure from such channel flows. Similarly, a lower limit was established for the jet collapse time. All experimental values were within the limits. The derived values indicate that the maximum instantaneous pressure differences between the jet and liquid may be more than 90 percent of the ambient pressure.

The conditions under which chugging occurs were determined experimentally. In particular, some practical estimates of jet susceptibility to unsteadiness were established. It is found that the tendency toward instability is strongly dependent on the gas density as well as on the flow conditions such as exit Mach number and operating pressure.

In Chapter 2, the experimental facility and instrumentation used to examine the short- and long-time behavior of these jets are described. Two facilities were fabricated, a water tank/reservoir system and a shock-tube apparatus. The water tank/reservoir facility was used to survey all the stages of jet development; the shock-tube apparatus was used to examine more closely the jet startup and transition.

In Chapter 3, the results of the experiments are reported, and the various stages of jet development are presented with photography and pressure measurements. For the startup phase, findings from both the water tank/reservoir and shock-tube experiments are given. In the shock-tube experiments, a small secondary jet developed on the gas/liquid interface. This feature is caused by shock focusing and is the direct result of the near-ideal impulsive acceleration by the shock wave.

In Chapter 4, the character of the jet unsteadiness is presented, and a physical model for jet column collapse is given. In addition, the effects of flow parameters on the unsteadiness are quantified, and the conditions under which steady jets exist are described. Finally, the proposed mechanism for chugging is discussed.

1.3. Previous Related Work.

In previous studies of nonreacting two-phase jets of a gas into liquid, the emphasis has been on understanding mixing and entrainment characteristics of the fully developed jet. Tross (1974) examined the far-field characteristics of submerged air jets in water and measured

the velocity profile, void fraction, and dynamic pressure. He investigated the entrainment characteristics of the two-phase jet and modified the entrainment law of Morton (1965) for turbulent plumes. The exit Mach number of his jets ranged from 1.5 to 6. His results indicate that the velocity profile, void fraction, and dynamic pressure of an air jet in water exhibit reasonable self-similarity. The entrainment properties are similar to single-phase jets when adjustments are made for variable density effects.

Bell et al. (1972) investigated how sonic nitrogen jets submerged in water impinge on a wall. Nozzle diameter, distance from the nozzle exit to the wall, and cross flow were examined for their effects on the jet impingement characteristics. Measurements were made of the jet diffusion angle and of the amount of droplet entrainment. The spreading angle of the free jet was found to be approximately 24 degrees, independent of the nozzle diameter and operating pressure. The same spreading angle was observed by Themelis et al. (1969) for reacting jets of chlorine in molten sodium. Homogeneous gas jets also have a spreading angle in the range of 18-25 degrees.

Few investigators have studied the unsteadiness of the interface of a gas jet into liquid known as chugging. Tross (1974) noted that at sonic conditions and at conditions slightly above sonic, an air jet into water exhibits unsteadiness and chugging. The chugging was eliminated when the Mach number of the flow was increased above about 1.5. Tross postulated that the liquid entering the orifice constricts the outward flow of gas, allowing pressure buildup upstream of the constriction, causing rapid ejection of gas from the orifice. However, no evidence was provided. Indeed, at such high velocities, liquid backflow into the nozzle seems unlikely; a simple calculation shows that the drag force on a sphere of liquid having a radius equal to, say, one tenth the nozzle diameter, would be on the order of 1000g!

Bell et al. (1972) and Kiceniuk (1952) also observed unsteadiness in the behavior of gas jets into liquid. Bell et al. noted the extensive breakup of the nitrogen/water interface in a cross flow, where large droplets of liquid were torn from the interface and entrained into the jet column. The Kelvin-Helmholtz instability was suggested as the mechanism for the interfacial breakup. Kiceniuk, in a study of vapor injection from a high pressure source through deLaval and convergent nozzles into water, reported that, for air into water, expansions of the gas outside of the nozzle are always present regardless of the stagnation pressure used.

In addition to experimental observations, many authors, including Rayleigh (1892), Batchelor & Gill (1963), Lessen et al. (1965), Zak et al. (1984), and Michalke (1970, 1977), have investigated the stability of an interface between fluids of different density. Recently, Michalke (1984) conducted an extensive review of the literature on the spatial stability of single-phase axisymmetric jets. Zak et al. discussed the stability of coflowing jets but restricted their attention to low velocities. Batchelor & Gill examined the temporal stability of a cylindrical vortex sheet to azimuthally periodic disturbances in inviscid incompressible flow; Lessen et al. modified the theory for the compressible case.

At high jet velocities, gas compressibility is an important consideration. In the present study, an effort was made to understand the effects of Mach number. To do this, the analysis by Lessen et al. was modified for the case where the ambient fluid is much more dense than the jet fluid. The intent was not to develop a new stability theory but to compare the experimentally measured pinchoff scales with the theoretically predicted wavelengths of the most amplified disturbance. The results of this analysis are discussed in the Appendix.

Chapter 2
EXPERIMENTAL FACILITY AND INSTRUMENTATION

2.1. Introduction.

Two facilities, a water tank/reservoir system and a blow-down shock tube, were fabricated for this investigation. The water tank/reservoir system was used to examine the later stages of jet development, while the shock tube was used to investigate the early times. Fast-response pressure transducers and high-speed photography were used in both facilities to document the detailed features of the transient behavior and the different stages of jet development.

2.2. Water Tank and Reservoir Facility.

The water tank/reservoir facility, shown in Figure 2.1, consists of a water tank, high pressure gas reservoir, fast-acting solenoid valve, and a nozzle. The rectangular water tank is 66 cm long, 30 cm wide, and 40 cm deep and is fabricated of plexiglass. A large plastic bag 90 cm deep is attached to the tank to contain splashing water. Mounted below the tank is a 0.04 cubic meters aluminum reservoir chamber. This vessel can be evacuated to 0.3 atmosphere absolute or pressurized to more than 12 atmospheres. The reservoir is fed with various gases through a flexible 0.635 cm hose from highly pressurized gas cylinders fitted with pressure regulators. Located within the tank are the fast-acting solenoid valve and nozzle. The valve has a 0.635 cm (1/4") orifice and can be operated at pressure differentials up to 14 atmospheres. In operation, flow is initiated by the opening of the valve; gas is discharged upward into liquid.

2.2.1. Nozzles. To achieve sonic and supersonic flow velocities, a convergent nozzle and three deLaval nozzles were fabricated. A schematic of a deLaval nozzle is shown in Figure 2.2. The throat diameter, D^*, for all nozzles is 0.32 cm (1/8"), and the ratio of the exit

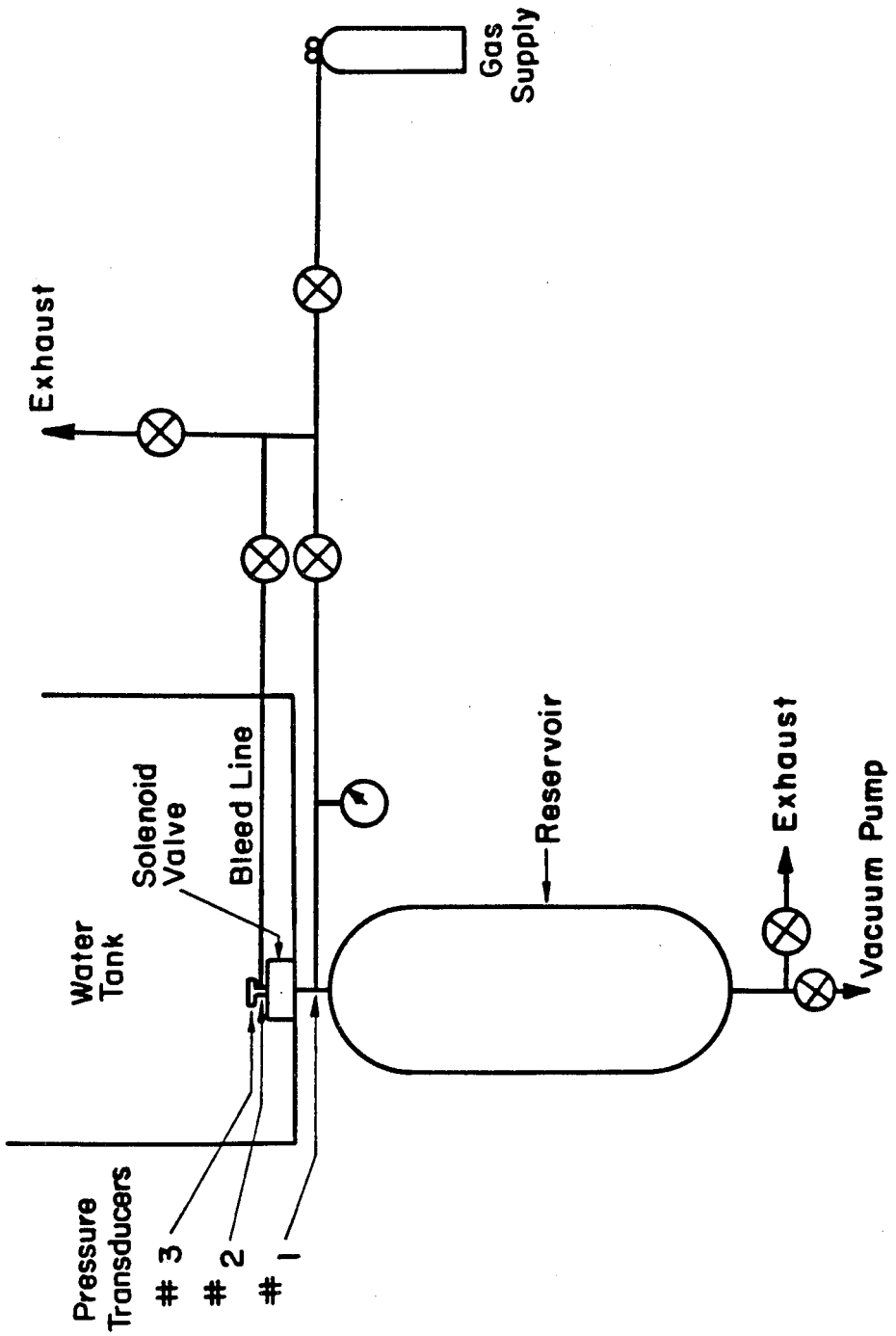

Figure 2.1 Water tank and reservoir assembly.

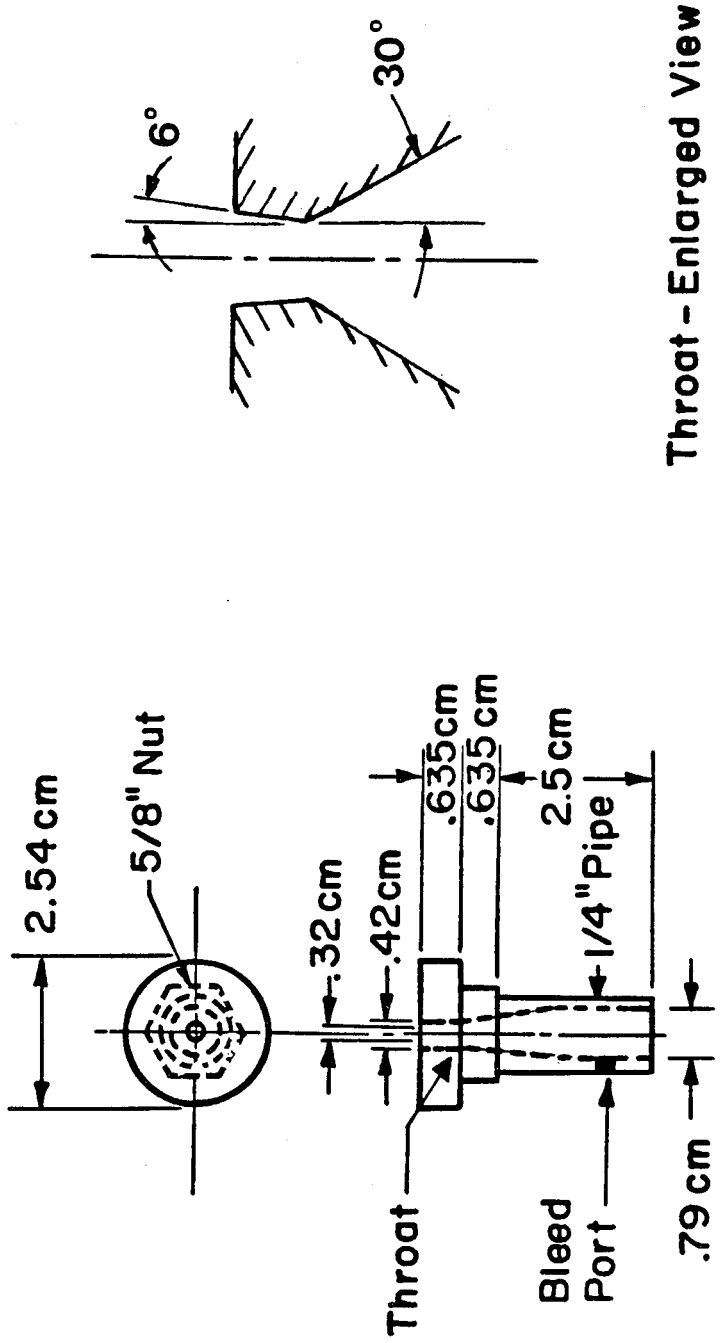

Figure 2.2 Schematic of A/A^* = 1.75 deLaval nozzle.

area to the throat area, A/A^*, ranges from 1.0 to 1.75. This permits exit Mach numbers up to 2.2. The converging and diverging sections of the deLaval nozzles are conical with half angles of 30 and 6 degrees, respectively. A small gas bleed port is located along the side wall of the convergent section. This port allows small amounts of gas to be fed into or evacuated from the nozzle for fine adjustment of the initial interface between the gas and liquid.

One concern, in view of the small nozzle size, is the thickness of the boundary layer at the nozzle exit. Therefore, estimates of the maximum boundary layer thickness were made. Two methods were utilized: Thwaites' method for axisymmetric geometry (White, 1974), and a method developed by Coles (1957) for two-dimensional, laminar, compressible flows. Both methods predicted the maximum displacement thicknesses to be less than 3.5 percent of the throat radius.

2.2.2. Gases. Four different gases, helium, nitrogen, and refrigerants 22 and 12, were discharged into water. The gas properties, namely, the ratio of specific heats, γ, and the sound speed, a, are shown in Table 2.1. The ratio of the liquid density to the gas density, ρ_a/ρ_j, is also indicated. The values range from 195 to 6250.

Table 2.1. Sonic Exit Velocity

Gas	ρ_a/ρ_j	γ	a (m/sec)
Helium	6250	1.67	1080
Nitrogen	869	1.40	353
Refrigerant 22	271	1.18	193
Refrigerant 12	195	1.14	153

2.2.3. Operation. To begin the experiment, the reservoir is evacuated and filled with gas (e.g., to 3 atmospheres). The tank is then filled with distilled water to a height of 30 cm. The solenoid valve is opened via a solid state relay directly controlled by the operator or by an input pulse. The jet is fired to clear liquid out of the nozzle and to establish a small bubble at the nozzle exit. The reservoir is then filled with gas to the desired operating pressure. A small amount of gas is bled into the nozzle to adjust the shape of the meniscus. The electronics and optics are then readied. Finally, the room is darkened and the camera readied for photography. An experimental run can begin; the jet is fired.

For subsequent runs, the same procedure is repeated, beginning with the filling of the reservoir to the desired operating pressure.

2.3. Pressure Measurements.

Fast-response piezoelectric pressure transducers were used to record the development of the gas jet into liquid. The pressure signal provides information about the transient behavior as well as serves as a trigger for photography. The transducers used are Model 113A21 and 112A21 manufactured by PCB Piezotronics, Inc. They are flush-mounted at three locations on the apparatus as shown in Figures 2.1 and 2.2. The first transducer is located near the reservoir chamber; the second is found downstream of the solenoid valve, just upstream of the nozzle throat; and the third is located on a baffle, in the water near the nozzle exit. The face of this third transducer is parallel with the orifice plane and is offset 1.6 cm from the jet centerline so as not to interfere with the flow.

The piezoelectric transducer is sensitive to a wide range of frequencies (0.5 Hz to over 100 kHz) and has excellent high-frequency response characteristics (1 μsec response time). However, the low-frequency response is somewhat limited by its discharge time constant

characteristic. This limiting feature can be briefly described as follows. When acted upon by say, a step function increase in pressure, the transducer produces a voltage increase as the output signal. With time, the voltage gradually dissipates even though there is no change in the pressure. The decay rate depends on the discharge time constant of the transducer. For Model PCB 113A21 and 112A21 transducers, the time constant is one second. This means that in one second, the voltage will decrease to a fraction of its peak value. The result is a signal that is lower than the actual pressure at later times. For a step function decrease in pressure, similar behavior occurs. Initially the output signal will decrease to reflect the pressure decrease. But following this, as the voltage dissipates, the signal gradually increases, returning to its starting (preloaded) value. This results in a signal that is higher than the true pressure at later times.

The pressure signals are directly recorded by a Nicolet Explorer III digital oscilloscope and stored on minifloppy magnetic disk. The data are then transferred to a PDP 11/23 computer via a GP-IB interface for analysis. Figure 2.3 shows the instrumentation diagram.

2.4. Photography.

Two photographic techniques, shadowgraphs and high-speed motion pictures, were used to document the detailed behavior of the gas jets into liquid. Both photographic setups are shown in Figure 2.4.

2.4.1. Shadowgraph Visualization. The shadowgraph visualization incorporates high-sensitivity film and a short-duration light source for minimal exposure time to produce high-resolution pictures. A Graphex-type camera with a 135 mm focal length lens and Polaroid type-47 film (ASA 2000) were used to record the image of the developing jet. The lens distance was adjusted to give a magnification of 1.0 to 1.3. The lens aperture setting was typically f11.

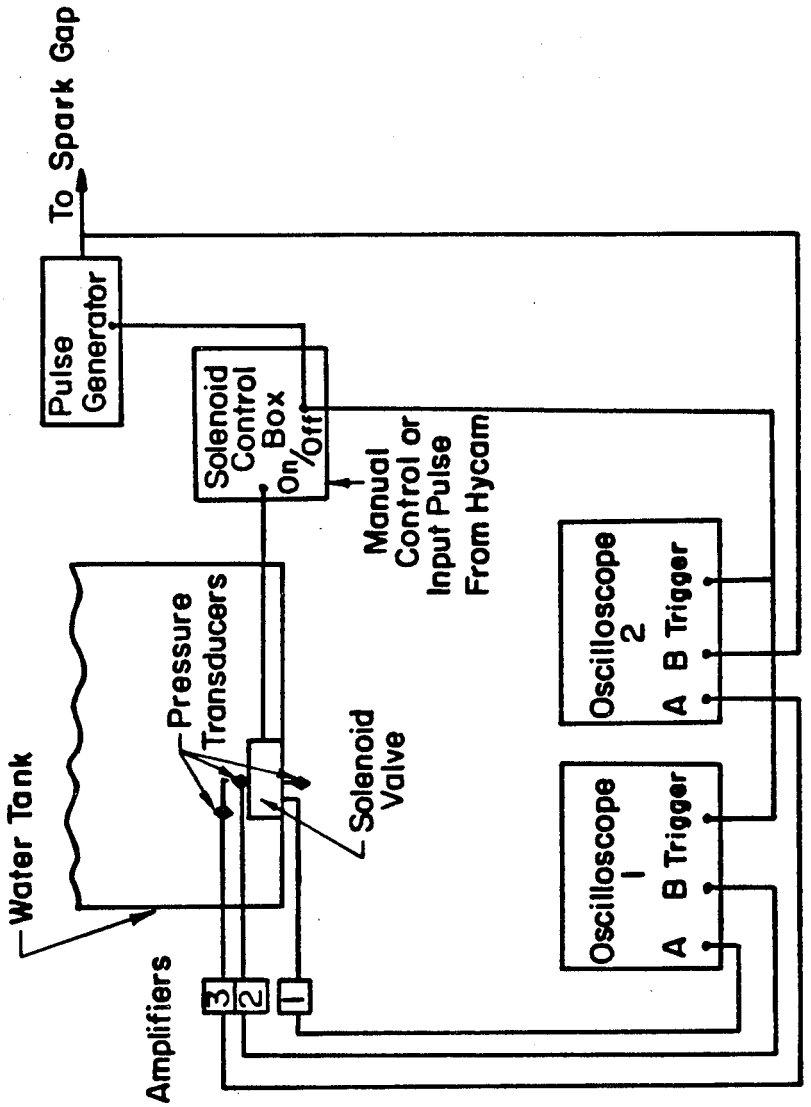

Figure 2.3 Instrumentation diagram.

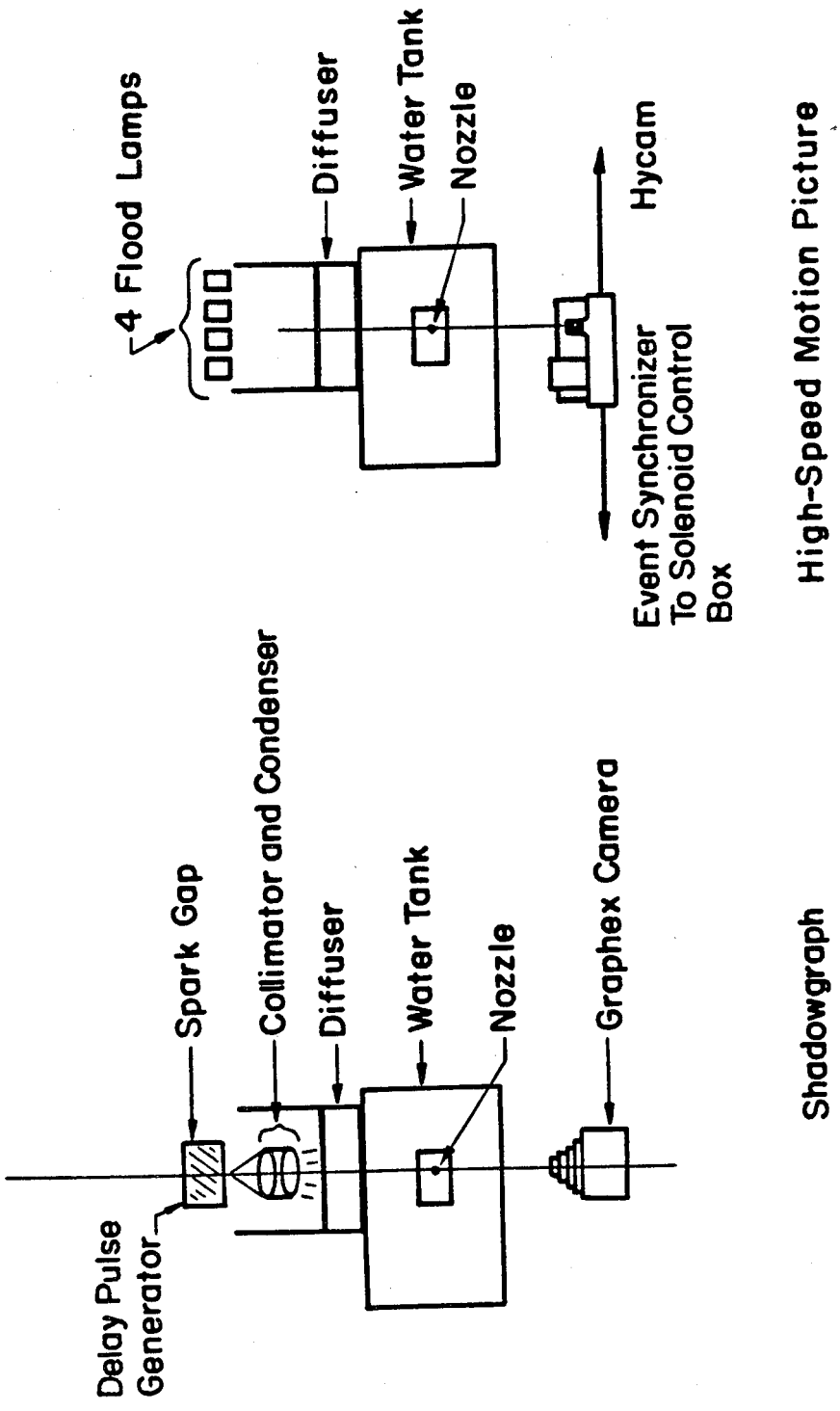

Figure 2.4 Photographic setup.

A spark gap was used as the primary light source. The spark gap produces a linear spark (approximately 6 cm long, 1 μsec duration) between two electrodes in a 90%/10% Argon/Air mixture. The gap was operated at 7 kV and was triggered by a 2 kV voltage pulse applied to the lower electrode. A collimator/condenser was used to collect the light onto a diffuser. The diffuser is a rectangular box, 23 cm x 23 cm x 10 cm, with plates of ground glass at two ends and lined on the inside with a diffuse reflector (dull side of foil). The jet is backlit, with the light source 48 cm from the nozzle.

At the start of a run, the room is darkened and the camera shutters are opened. The signal from the opening of the solenoid valve initiates the gas flow and triggers the oscilloscopes and a delay generator. The delay generator, which was set to delay times between five milliseconds and one second, sends a pulse to trigger the spark gap. As the gap fires, the image of the jet is recorded.

2.4.2. High-speed Motion Picture. In addition to shadowgraphs, the behavior of gas jets into liquid was documented by high-speed movies. The advantage of high-speed motion pictures over shadowgraphs is that all stages of jet development can be recorded in a single run. The motion picture photographic setup is shown in Figure 2.4. Again, the jet is backlit; both the light source and the camera are located 60 cm from the nozzle.

The motion picture camera used was a 16mm high-speed, full-frame HYCAM II, Model 410064, manufactured by RedLake Corporation. This camera utilizes an eight-sided rotating prism for optical compensation. The framing rate is variable from 20 to 11000 frames per second (fps). Higher framing rates are achievable with a quarter-frame system and with a 32-sided rotating prism.

Two features of the HYCAM are worth mentioning: the event synchronizer and the LED timing lights generator. In operation, the HYCAM requires a finite run time to reach the correct high framing rate. Therefore, it is necessary to start the camera before starting the event. The event synchronizer can be conveniently used for that purpose. When a certain length of film passes through the camera, the synchronizer provides a 10 volt pulse, which can be used to trigger the event. The length of film is adjustable by the user.

The LED timing lights generator (TLG) produces light pulses at 100, 1000, and 5000 hertz, which can be used to mark the edge of the film as the film progresses through the camera. The markings provide an accurate method for timing of the frames.

For this investigation, the HYCAM was used at a framing rate of 4000 fps with the standard 1/2.5 shutter and a 75 mm focal length lens. The exposure time was 100μsec. A lens aperture setting of $\underline{f}$5.6 and a magnification of 0.8 give the optimum tradeoff between depth of field and resolution for the light given. The light source for the motion pictures is four flood lamps providing 4000 watts of continuous power. The lamps are used in conjunction with the ground glass diffuser described earlier. The images are recorded on Kodak 4x Negative (ASA 400) and 4X Reversal (ASA 320) films.

A run with the motion picture camera is begun by loading the camera in the darkened room. The flood lamps are then turned on and the camera is started. When the camera reaches the preset framing rate, the event synchronizer sends a pulse to trigger the solenoid valve, which fires the jet. The opening of the valve triggers the oscilloscopes to record the pressure data.

2.5. Shock-tube Facility.

A blow-down shock tube was constructed to provide a precisely controlled gas supply and a well-defined starting condition for study of the early stages of jet development. In the setup, shown in Figure 2.5, the shock tube is placed over a tank of water such that the driven section is partially submerged. When the tube was fired, gas exhausts downward into the tank.

The shock tube consists of three main parts: the driver section, the cutting mechanism, and the driven section (Figure 2.5). The driver section has a circular cross section and is 152 cm long. The tube diameter is 5 cm for nearly the entire length but contracts to 1.27 cm near the diaphragm. This contraction acts as a nozzle to accelerate the flow.

The cutting mechanism consists of crossed knife blades, each 1.27 cm wide, 0.635 cm high, and recessed 0.08 cm from the diaphragm plane. The cutter is located on an 18 cm diameter, 1.27 cm thick plate which serves as a baffle for the outflowing gas. Originally, the shock tube was designed so that the flow would expand immediately into water. However, tests indicated that immediate expansion did not allow sufficient time for the shock to develop. Also, the petals of the rupturing diaphragm disturbed the flow significantly. Therefore, to eliminate those undesired effects, a longer driven section was fabricated. The resulting driven section is a spool-like attachment with a central hollow tube and two end plates. One plate is mounted to the driver; the other serves as a baffle for the orifice. The section is 15.3 cm long and has the same inner diameter (1.27 cm) as the contracted driver section. The available test time using this extension is 500 μsec. The test time is defined here as the time from the shock arrival at the interface to the time of the arrival of a subsequent wave. To allow for a longer test time, a second extension was fabricated. This second extension is 30 cm long and has an inner diameter of 0.635 cm.

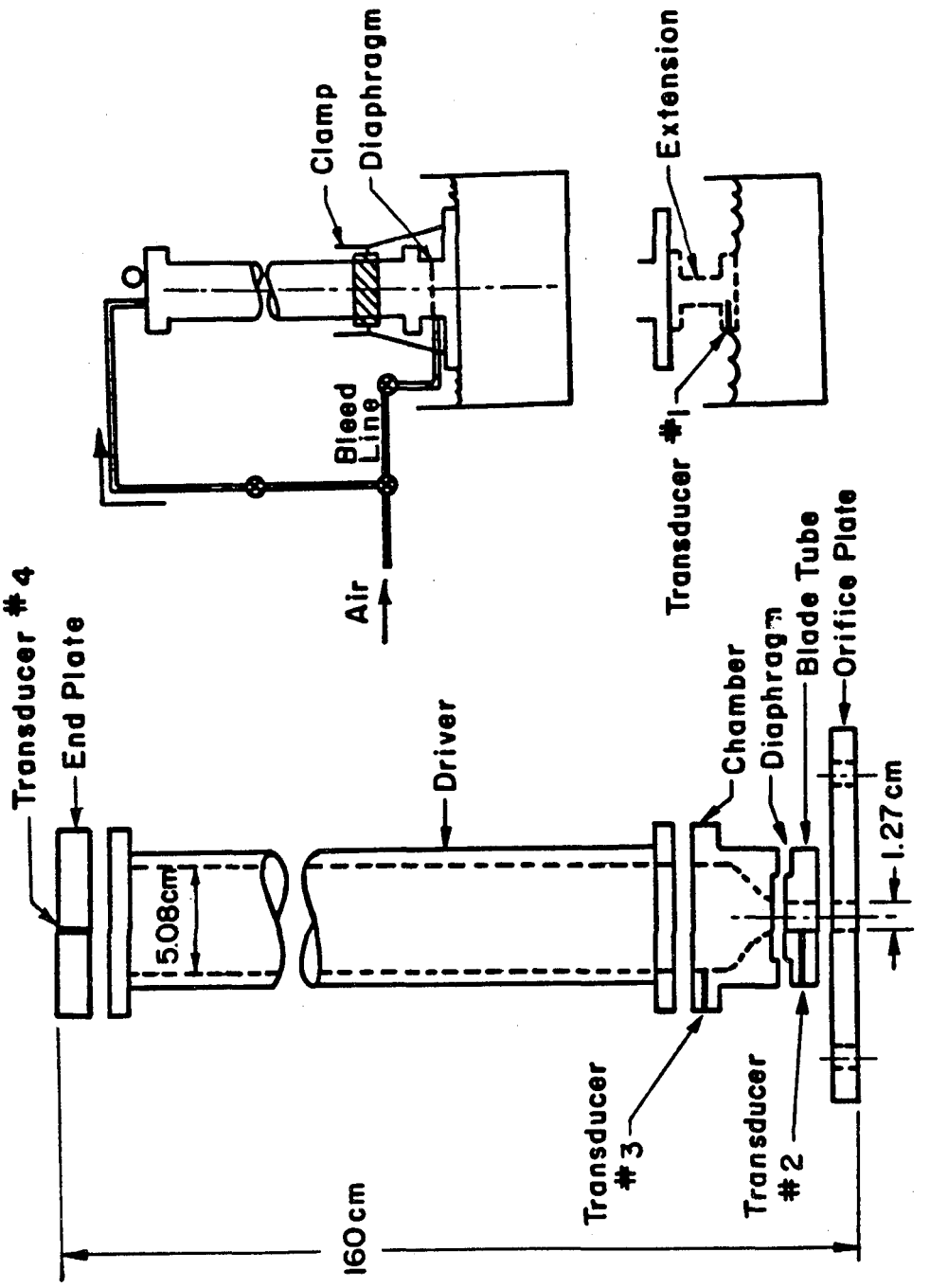

Figure 2.5 Schematic of the blow-down shock tube.

The diaphragms are aluminum foil sheets of 18, 38, and 50 μm thickness. These sheets are coated with Krylon acrylic to prevent leaks from fine porous holes (diameters on the order of 5 μm), which occur naturally. It was critical that leaks be prevented, for any minute seepage of gas significantly altered the shape of the meniscus and prevented a repeatable initial condition. When leaks did occur, fine bubbles could be seen on the gas/liquid interface.

The pressure instrumentation and photographic techniques used in the shock tube facility were the same as those previously described for the jet injection system. The instrumentation diagram is shown in Figure 2.6. Pressure measurements were taken at four locations, shown in Figure 2.5: at the end wall of the driver section, just upstream of the nozzle-like contraction, at the knife blades, and 0.125 cm from the exit in the driven section. The pressure measurement taken near the knife blades was used as the trigger for the oscilloscopes and delay generator. The arrival of the shock detected by the transducer near the open end was used as the trigger for photography and for timing. The time elapsed from the shock arrival and the output of the delay generator to trigger the light source was assigned as the jet development time.

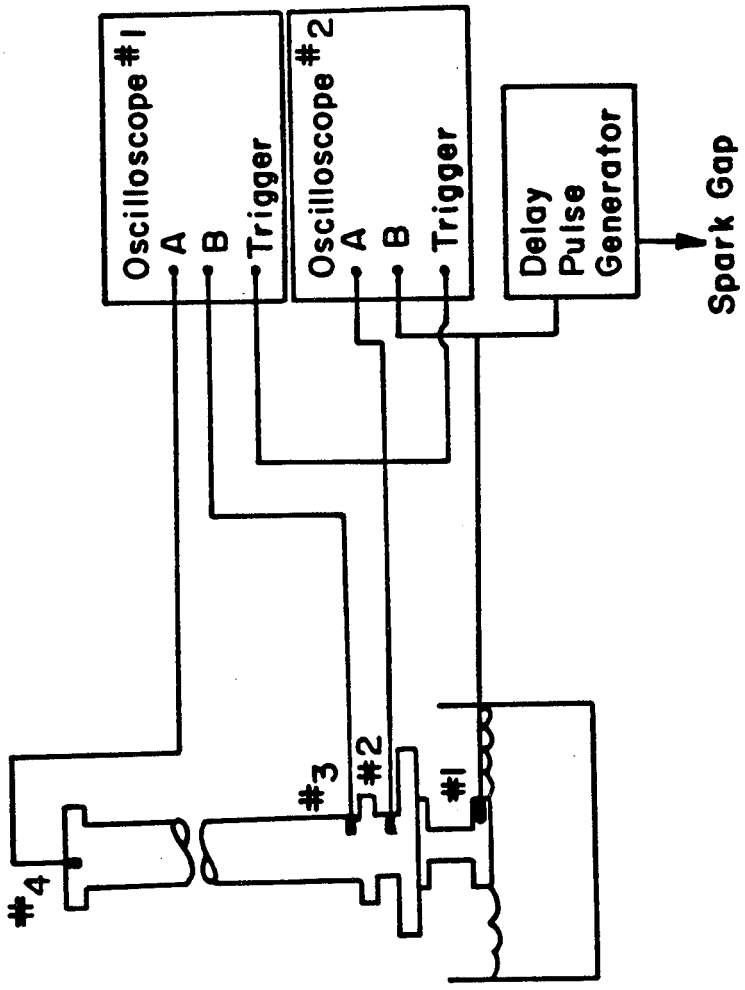

Figure 2.6 Shock tube instrumentation.

Chapter 3
STAGES OF JET DEVELOPMENT

3.1. Introduction.

In this chapter, experiments are reported whose purpose was to examine the development of impulsively initiated high velocity gas jets into water. A selection of photographs and pressure traces are presented to provide a survey of the various physical processes that occur in each stage of development. The details of the unsteady behavior known as chugging will be discussed in the next chapter.

The experiments were conducted in two phases. In the first phase, the jet startup process was investigated. Nitrogen was injected downward from a blow-down shock tube into stationary water. The incident Mach numbers, M_s, were 1.4, 1.9, and 2.2. Two initial conditions of the jet were considered at each Mach number. The initial condition refers to the configuration of the gas/liquid interface just prior to firing. In one configuration, a large hemispheric bubble with a diameter the size of the orifice served as the interface. In the second configuration, the interface was a meniscus caused to form inside the nozzle. The interface was produced by carefully evacuating nitrogen gas from the shock tube driven section such that the lowest point of the concave surface was located at the plane of the nozzle exit.

In the second experimental phase, all later stages of jet development were investigated. Particular attention was given to jet transition, steady state, and departure from steady state. For the purposes of this phase, a fast-opening solenoid-actuated valve is sufficient for initiating the flow. Helium (He), nitrogen (N2), and refrigerants 22 (R22) and 12 (R12) were injected upward into water at jet Mach numbers ranging from 1.0 to 2.2. For each gas and nozzle, a range of operating pressures was tested. The experimental conditions are summarized in

Table 3.1. Listed are the different gases, the nozzles, the design exit Mach numbers, M_e, and the operating pressure ratios, P_o/P_a (i.e., the ratio of the reservoir pressure to the ambient presure). The pressure-matched conditions are marked by "+". The untested pressure-matched conditions are also listed for reference. At each condition, the jet was fired four to ten times to obtain a large sampling of data. In each case, a hemispheric bubble attached to the nozzle served as the initial interface between the gas and liquid. Each firing lasted about two seconds and constituted a single test run.

3.2. Jet Startup.

Figure 3.1 shows a series of photographs taken at early times during the development of a shock-initiated nitrogen jet into water. Each shadowgraph depicts the startup of a different jet. The elapsed time from the arrival of the shock at the nozzle exit is listed below each photograph. Although the jets were actually discharged downward in these experiments, they are presented here in the upward direction to be consistent with the jets from the second phase of experiments. Prior to each run, the shape of the gas/liquid interface (the meniscus) was carefully adjusted to insure repeatability. In this case, the shape of the initial interface is a large hemispheric bubble. The bubble diameter is equivalent to the diameter, D, of the nozzle.

The jet startup is characterized initially by radial outward propagation of the gas/water interface, which we call bubble blowing. The gas motion is evidently accompanied by extensive recirculation in the bubble, and there is little axial momentum transmitted to the liquid. Up to approximately 600 μsec, the surface of the startup bubble is smooth except for the development of a small bubble along the jet axis. This bubble is believed to be a secondary jet that forms as the result of the shock-initiated flow. The characteristics of this secondary jet and the mechanism for its initiation are discussed later.

Table 3.1. Experimental Conditions

Gas		Nozzle Area Ratio, A/A^*			
		1.00	1.11	1.50	1.75
R12	M_e	1.00	1.37	1.75	1.90
	P_o/P_a	4.06	4.06	$(4.84)^+$	$(6.22)^+$
		3.38	3.38	3.72	4.06
		3.25	2.72^+	3.18	2.97
		2.84			
		2.36			
		1.74^+			
R22	M_e	1.00	1.37	1.77	1.92
	P_o/P_a	5.08	5.42	5.42	$(6.57)^+$
		4.74	5.28	$(5.08)^+$	5.42
		3.72	4.74	4.74	4.40
		3.04	4.40	4.40	3.11
		2.36	4.06	3.75	2.70
		1.76^+	3.72	3.04	
			3.38		
			2.79^+		
N2	M_e	1.00	1.40	1.86	2.04
	P_o/P_a	5.08	7.80	7.80	$(8.37)^+$
		4.40	7.12	6.44	5.29
		3.59	5.16	6.28^+	4.27
		3.24	4.74	5.08	3.64
		2.36	4.40	4.40	2.91
		$(1.89)^+$	3.52		
			$(3.18)^+$		
He	M_e	1.00	1.44	1.97	2.20
	P_o/P_a	6.44	5.04	$(7.96)^+$	$(11.1)^+$
		4.74	4.40	5.76	4.40
		4.06	3.70^+	4.40	3.38
		2.31	2.70		
		2.05^+			

$^+$ indicates pressure-matched condition

$()^+$ indicates untested pressure-matched condition

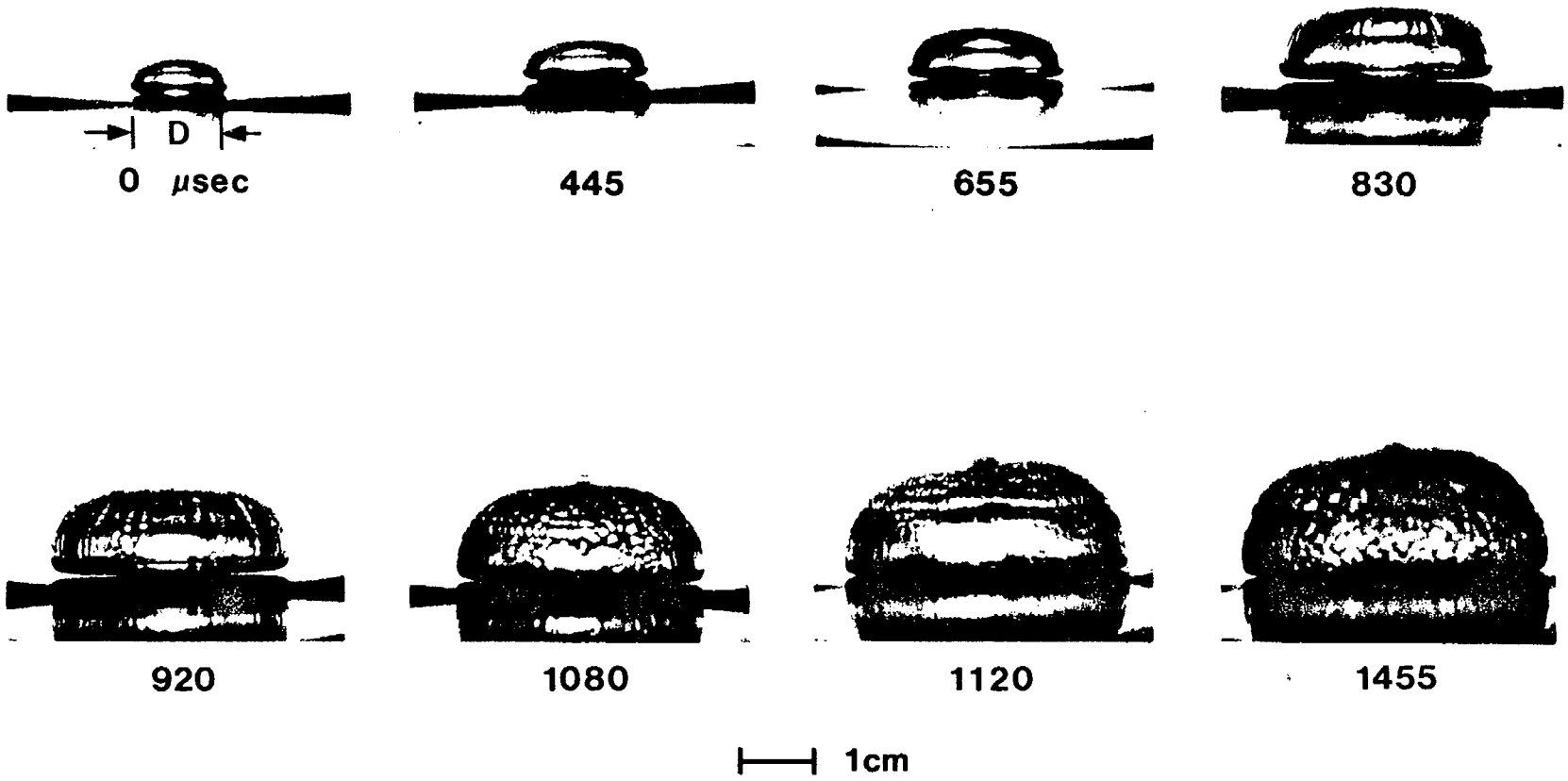

Figure 3.1 Startup of a shock-initiated M_s = 1.4 nitrogen jet. Hemispheric bubble at t=0. Nozzle diameter, D = 1.27 cm.

As the jet grows, the bubble surface is subject to large radial accelerations, so distortions develop as a consequence of the Rayleigh-Taylor instability. Thus, the effects of acceleration seem to predominate, and evidence of the Kelvin-Helmholtz instability at this stage is not visible. The interface velocity is on the order of 20 m/sec. Sometime between 0 and 600 μsec, small-scale roughness is initiated on the bubble surface. The roughness is barely visible at 655 μsec. However, by 830 μsec, the distortions can be seen clearly as longitudinal striations that originate near the bubble base and converge at the bubble centerline. The orientation of the distortions is indicative of the radially outward motion of the gas. The wavelengths of the perturbations are initially on the order of 0.03-0.1D at 830 μsec. However, as the bubble growth increases, the length scales also increase, and the longitudinal pattern breaks up into more random disturbances. At 1100 μsec, surface distortions separate the bubble into two distinct regions: a bubble base, which shows large-scale roughness, and a bubble cap, which shows circumferential waves. The large-scale wrinkling on the base is the remnant of the longitudinal perturbations which had earlier covered the entire bubble surface; the circumferential waves are evidently newly developing features of the Rayleigh-Taylor instability. Regularly spaced lobes or beads in each layer of the cap show the three-dimensionality of the instability. The length scales of the beads are on the order of 0.08-0.12 times the bubble height, H. The spacing of the striations increases and the beads become more prominent as the bubble grows.

3.2.1. Effect of Initial Condition. Figure 3.2, like Figure 3.1, is a series of photographs depicting the jet startup. The flow conditions are the same as in the previous case, except that here only a small portion of the initial gas/liquid interface can be seen outside the nozzle, as indicated by the photograph marked t=0. The jet startup is again characterized by bubble growth, and the general features of development are unchanged despite the difference in initial condition.

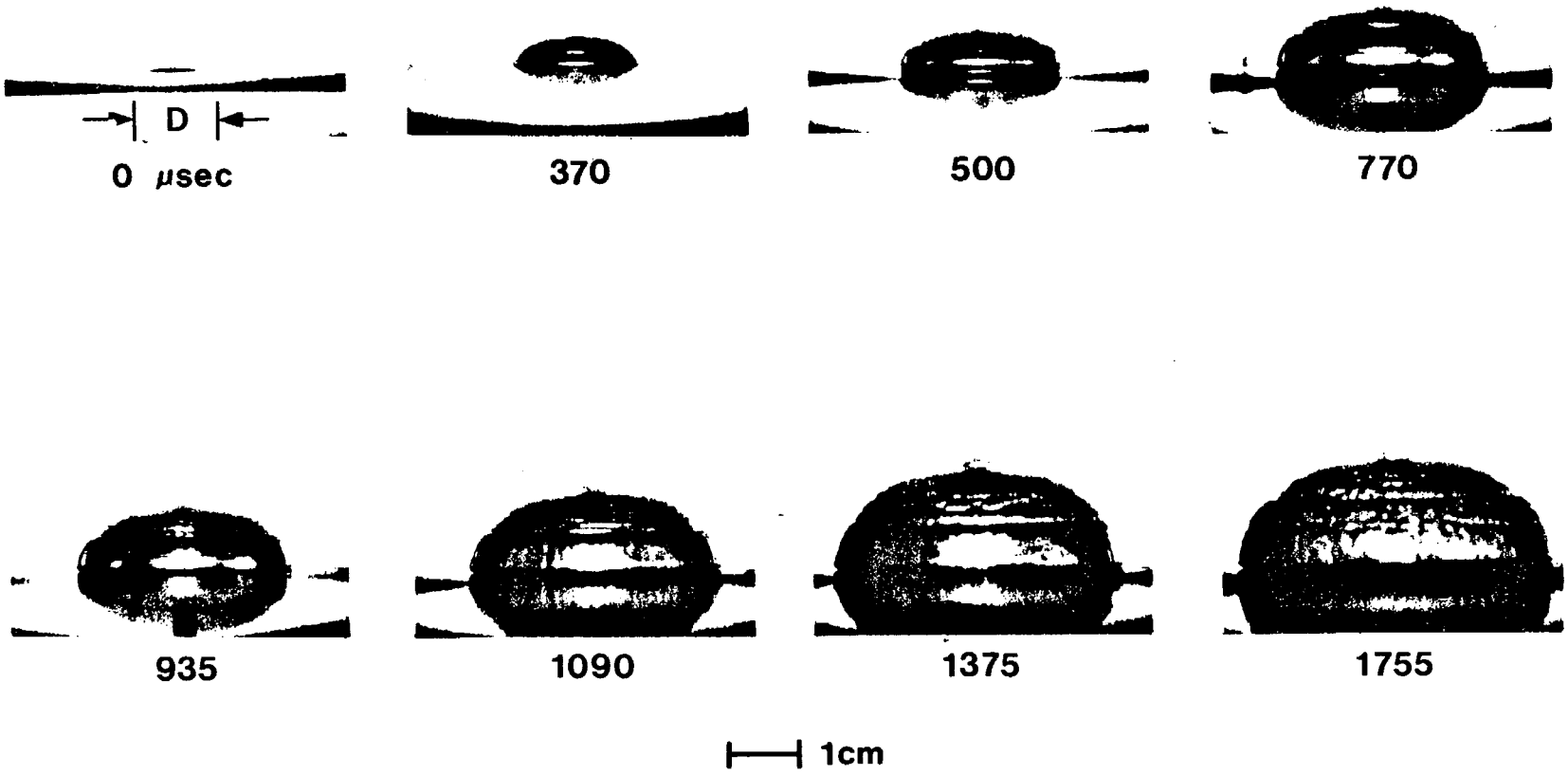

Figure 3.2 Startup of a shock-initiated M_s = 1.4 nitrogen jet. Slight protrusion at t=0. Nozzle diameter, D = 1.27 cm.

The bubble surface is again smooth initially, in this case, up to 400 μsec, after which longitudinal and circumferential distortions develop. The secondary jet along the primary jet axis is also evident. At 600 μsec, two bubble halves, the base and the cap, appear. Circumferential perturbations on the bubble cap can be seen clearly in all photographs after 600 μsec; the longitudinal streaks, however, are less distinct and can be seen only on the bubble base. The spacing of the streaks measured at 770 μsec are about 0.08D; the length scales of the circumferential striations are 0.08-0.12H. These scales are similar to those for the jet startup depicted in Figure 3.1. As the bubble grows, the wrinkling and the smallest scales on the surface of the bubble base are smoothed out by the effects of surface tension. Eventually after 1200 μsec, the circumferential roughness covers the entire jet surface.

3.2.2. Effect of Incident Shock Strength. Figure 3.3 shows the initiation of a nitrogen jet where now the incident Mach number is 2.2. The growth is reminiscent of that for the jet shown in Figure 3.1; similarities include bubble blowing, the appearance of a secondary jet, and surface distortions. However, differences in the detailed features of the bubble surface are also apparent. For example, at 112 μsec, disturbances that originate from the nozzle lip and that appear as small knobs at the bubble base are clearly evident here but were not distinct in Figures 3.1 and 3.2. These perturbations have length scales of 0.05D and gradually develop into longitudinal streaks at 200 μsec. Some time between 112 μsec and 200 μsec, circumferential waves are initiated. By 200 μsec, two "rings" form on the upper half of the bubble surface. These rings persist as the jet grows and give the illusion of a cap. At 280 μsec, a fishscale-pattern roughness forms just beneath the rings. Three types of distortions are now evident: the longitudinal streaks at the bubble base, the two rings, and the fishscale pattern. Later, the distortions break up into relatively uniform, fine-scaled (~ 0.1D) roughness over the entire bubble surface, similar to the jets in Figure 3.1 and 3.2. At 618 μsec, a crease forms

Figure 3.3 Startup of a shock-initiated M_s = 2.2 nitrogen jet. Nozzle diameter, D = 1.27 cm.

across the middle of the bubble as the first sign of the axially developing gas flow.

3.2.3. Bubble Growth. The evolution of the jet is illustrated in Figure 3.4. The jet width, B (normalized by the nozzle diameter D), and height, H (normalized by the the nozzle radius, R = D/2), are shown as functions of normalized time, $U_e t/D$. Three sets of data for nitrogen jets at different shock Mach numbers are plotted in the figure. Initially, the jet grows linearly in both the lateral and axial directions; the interface thus maintains a hemispherical shape. The outward motion of the interface is 20-30 m/sec. However, after $U_e t/D = 50$, the lateral growth begins to taper off, while the axial growth rate increases, implying an axial elongation of the original hemispherical interface. By $U_e t/D = 200$, the bubble height is almost twice the scaled width.

At these early times, the growth of the jet is reasonably well predicted by classical bubble growth theory (see Plesset & Prosperetti, 1977). According to the theory, the growth of the bubble radius is initially dominated by the inertia of the liquid. If the pressure and temperature in each phase are assumed uniform and the gas is in thermal equilibrium with the liquid surface, the bubble radius grows linearly in time as

$$R_b = \left[\frac{2}{3}\left|\frac{P_b - P_a}{\rho_l}\right|\right]^{1/2} t + R_o \qquad (3.1)$$

where R_o is the initial radius, ρ_l is the liquid density, and P_b and P_a are the bubble and liquid pressures, respectively. Since for these early times, the jet grows hemispherically, the bubble radius is equivalent to the jet height, H, or one-half the jet width, B. If we denote R, the radius of the nozzle (i.e., D/2), as the initial jet radius, Equation (3.1) may be written in the following nondimensional

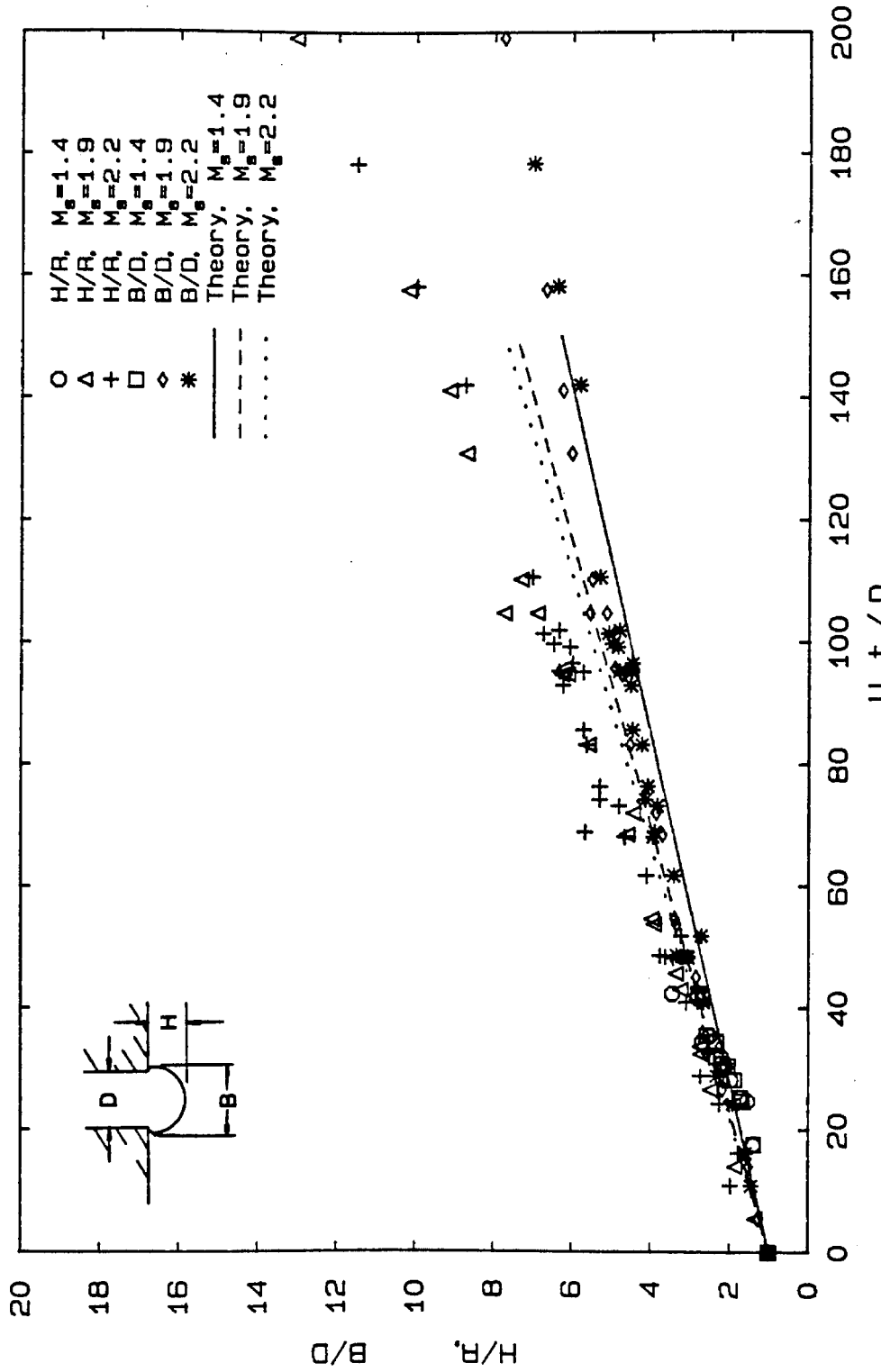

Figure 3.4 Comparison of jet development and bubble growth

form,

$$\frac{B}{D} = \frac{H}{R} = \left[\frac{2}{U_e}\right]\left[\frac{2}{3}\left[\frac{P_b - P_a}{\rho_l}\right]\right]^{1/2}\left[\frac{U_e t}{D}\right] + 1. \qquad (3.2)$$

The theoretical bubble sizes computed from Equation (3.2) from the known initial pressure and diameter are shown by the solid and dashed lines in Figure 3.4. At the early times, the experimental data and theory are in good agreement. However, above $U_e t/D$ of 50, the theory underpredicts the axial development, although the lateral spreading continues to show reasonably good agreement, at least up to $U_e t/D$ of 80.

At small $U_e t/D$, when the growth of the jet is radially outward, one would expect the gas acceleration to cause surface distortions which are uniformly distributed around the bubble through the action of the Rayleigh-Taylor instability. However, at later times, when the flow direction changes, the axially moving gas is more likely to cause surface deformations near the upper half of the bubble. Table 3.2 shows the times at which surface distortions are initiated for the different jets.

Table 3.2. Onset of Distortions

M_s	$U_e t/D$	
	Longitudinal	Circumferential
1.4	21	42
1.9	23	44
2.2	31	48

If the listed times in Table 3.2 are compared with the growth of the

jet in Figure 3.4, it becomes evident that longitudinal perturbations do indeed form when the bubble growth is equal in all directions, while circumferential perturbations develop when the growth becomes axially directed. This correlation of the onset time and the orientation of the surface deformations with the direction of bubble growth confirms the hypothesis that the distortions arise through the action of the Rayleigh-Taylor instability.

3.2.4. Secondary Jet.

3.2.4.1 Argument for secondary jet development. One distinct feature of the jet startup is the appearance of a small bubble at the tip of the growing jet. The protrusion is believed to be a secondary jet that is produced as the result of shock focusing. The development can be deduced from a simple geometric acoustic argument as follows. The impingment of the shock wave on the gas/liquid interface can be visualized as the interaction of a plane acoustic pulse with a cylindrical lens. Figure 3.5(a) is a schematic representation of the startup process. Shown in frame (a) is the incident shock wave traveling downwards in the shock tube towards the bubble surface. The wave impinges on the surface and reflects. The wavefronts of the reflected waves are marked in Figure 3.5(b) and (c). The arrows, which show the direction of gas motion, indicate that locally at the bubble tip, there is a net component of flow downwards along the jet centerline. The axially directed flow and the local high pressure initiate a new gas jet into liquid, which again develops as a growing bubble. By the time the reflected wavefront is in the configuration shown in frame (d), the secondary jet should be apparent.

Comparison of the predicted times for the initiation of the secondary jet with the times measured from experiment, validates this argument. For example, Figure 3.6(a) shows the growth of the secondary jet as a function of time as measured from experiment. Extrapolation of the jet height, h, to zero indicates that initiation occurs at

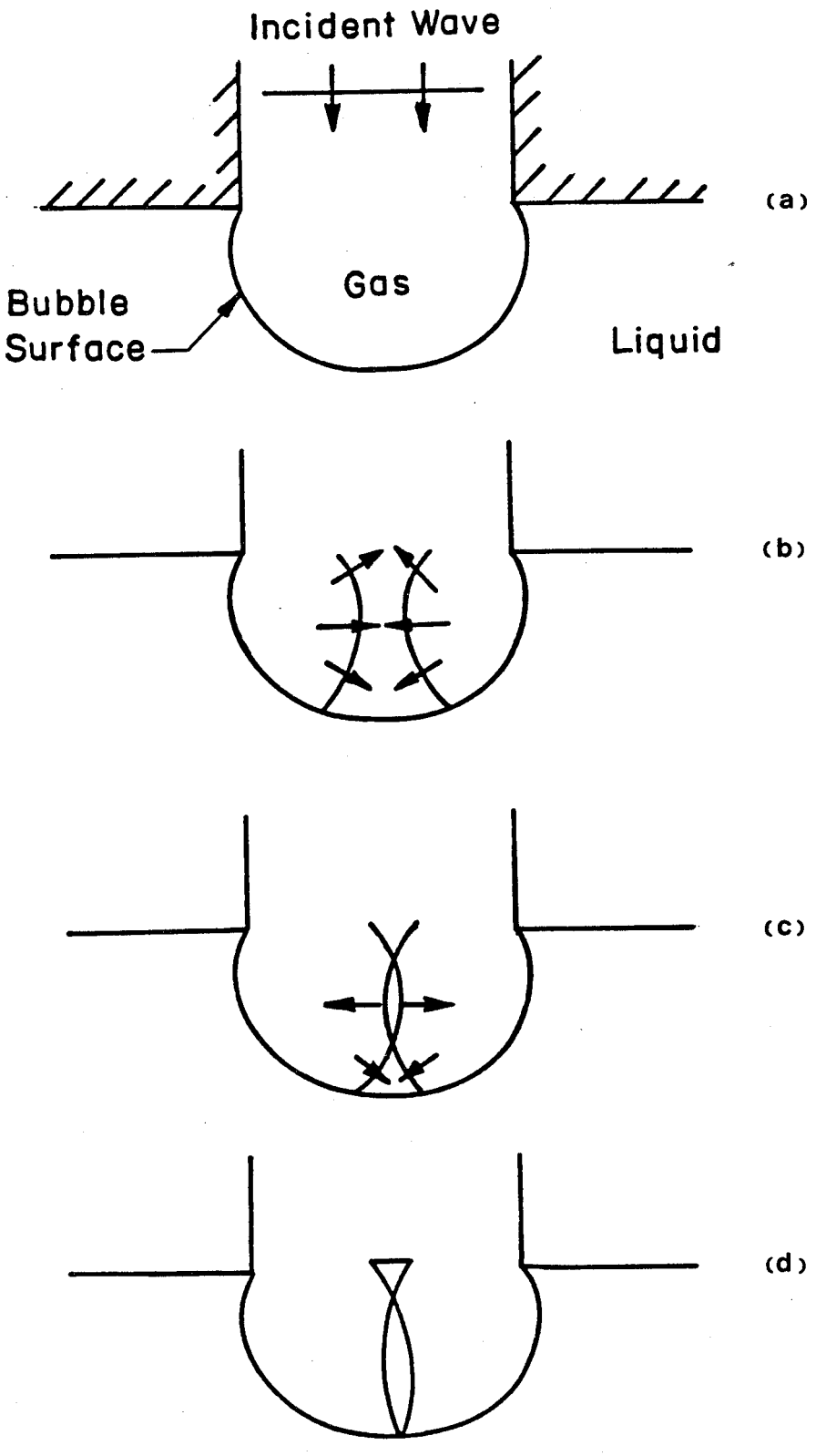

Figure 3.5 Schematic representation of wavefront propagation

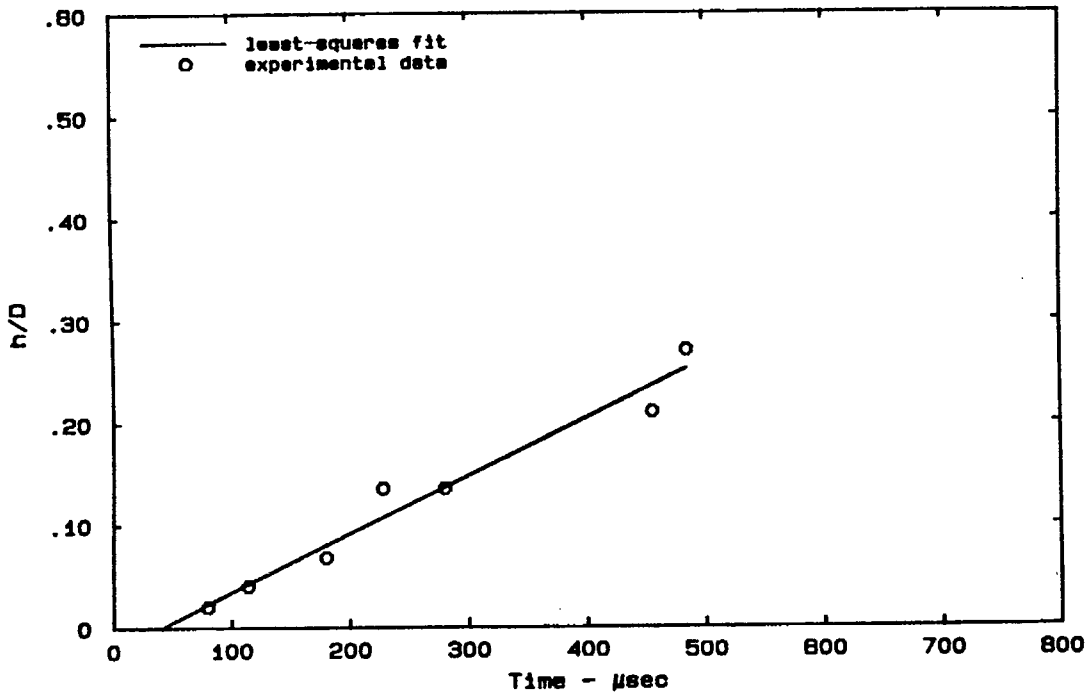

(a)

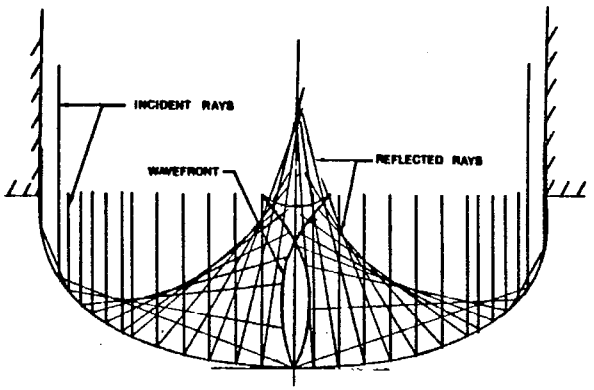

(b)

Figure 3.6 Evolution of secondary jet,
(a) Secondary jet height as a function of time,
(b) Ray diagram.

approximately 30 μsec. Figure 3.6(b) shows the ray diagram of the startup bubble on which the secondary jet develops. Two families of rays are indicated in the figure. The parallel lines from the top are the incident rays; the lines converging inside the bubble near the centerline are the reflected rays. The wavefronts of the reflected rays at 32 μsec are marked in the figure by the darkened lines. According to the geometric acoustics argument, the secondary jet should be initiated when the reflected wavefront is in the configuration shown *(compare with Figure 3.5(d))*. *Indeed*, the estimated time of 32 μsec from ray tracing compares well with the 30 μsec time from experiment.

3.2.4.2 Features of the secondary jet. Many features seen in the primary jet development are also seen in the secondary jet development. Initially, both jets grow linearly, as illustrated by Figures 3.4 and 3.6. However, the secondary jet is much weaker than the first; its growth rate is only 7 m/sec as compared to 20-30 m/sec for the primary jet. Both jets also appear as growing hemispheric bubbles. This can be seen by comparing the enlarged view of the jet in Figure 3.7 with Figure 3.1. In addition, the strong symmetry of the configuration has the effect that the secondary jet appears to emerge from a nozzle, just as the primary one. Figure 3.7 shows what appears to be a stem connecting the two jets. The stem serves as the nozzle from which the gas discharges and feeds the secondary startup bubble. Furthermore, like the primary jet, the secondary jet develops a small protrusion, which presumably is the growth of a third jet. Both jets also experience large radial accelerations, which lead to similar deformations of the bubble surface through the action of the Rayleigh-Taylor instability. These distortions have length scales on the order of 0.1H in the primary jet and 0.1h for the secondary jet, where h = 2 mm, as shown in *Figure 3.8*.

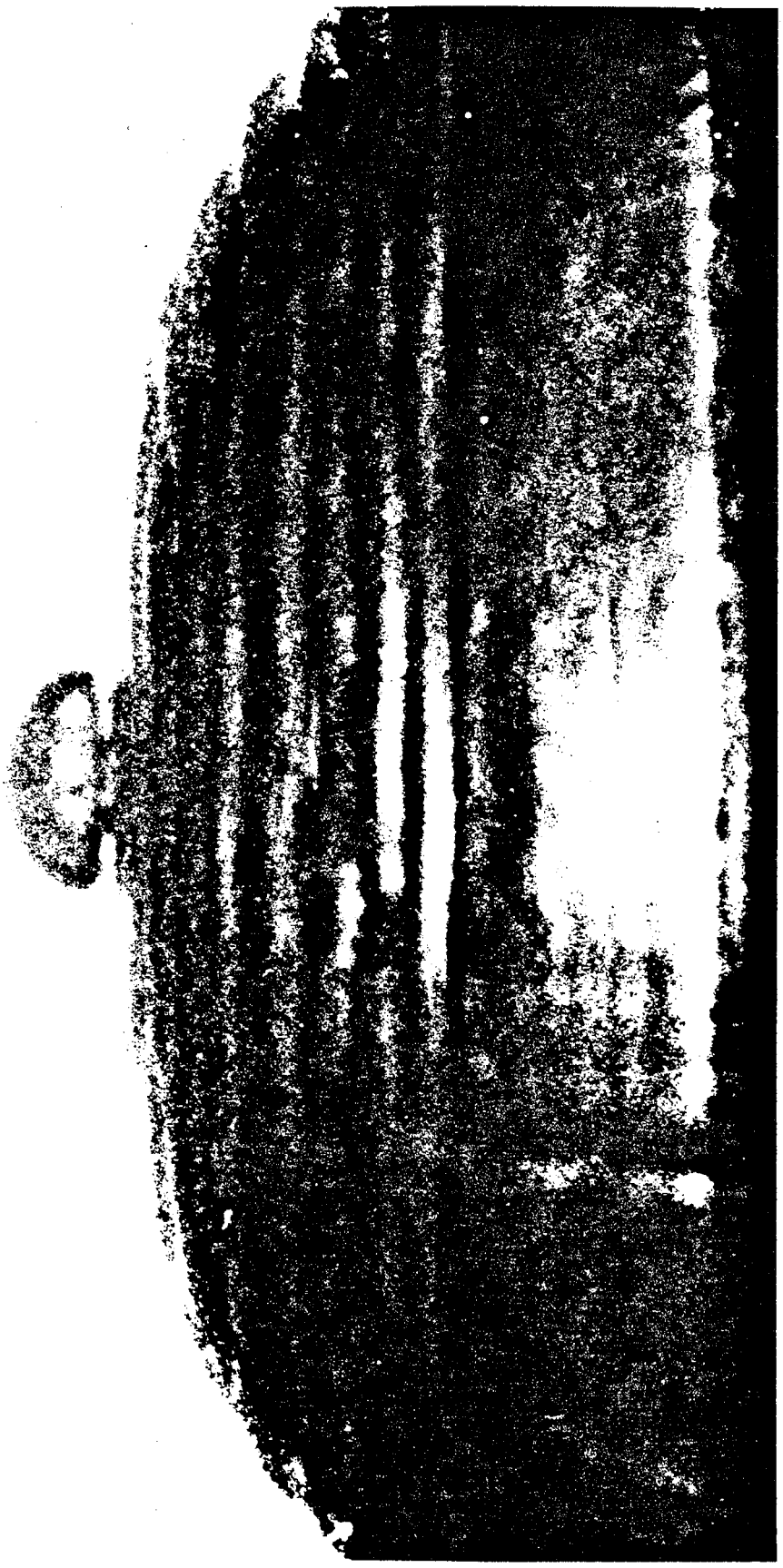

Figure 3.7 Enlarged view of secondary jet. Nozzle diameter, D = 1.27 cm.

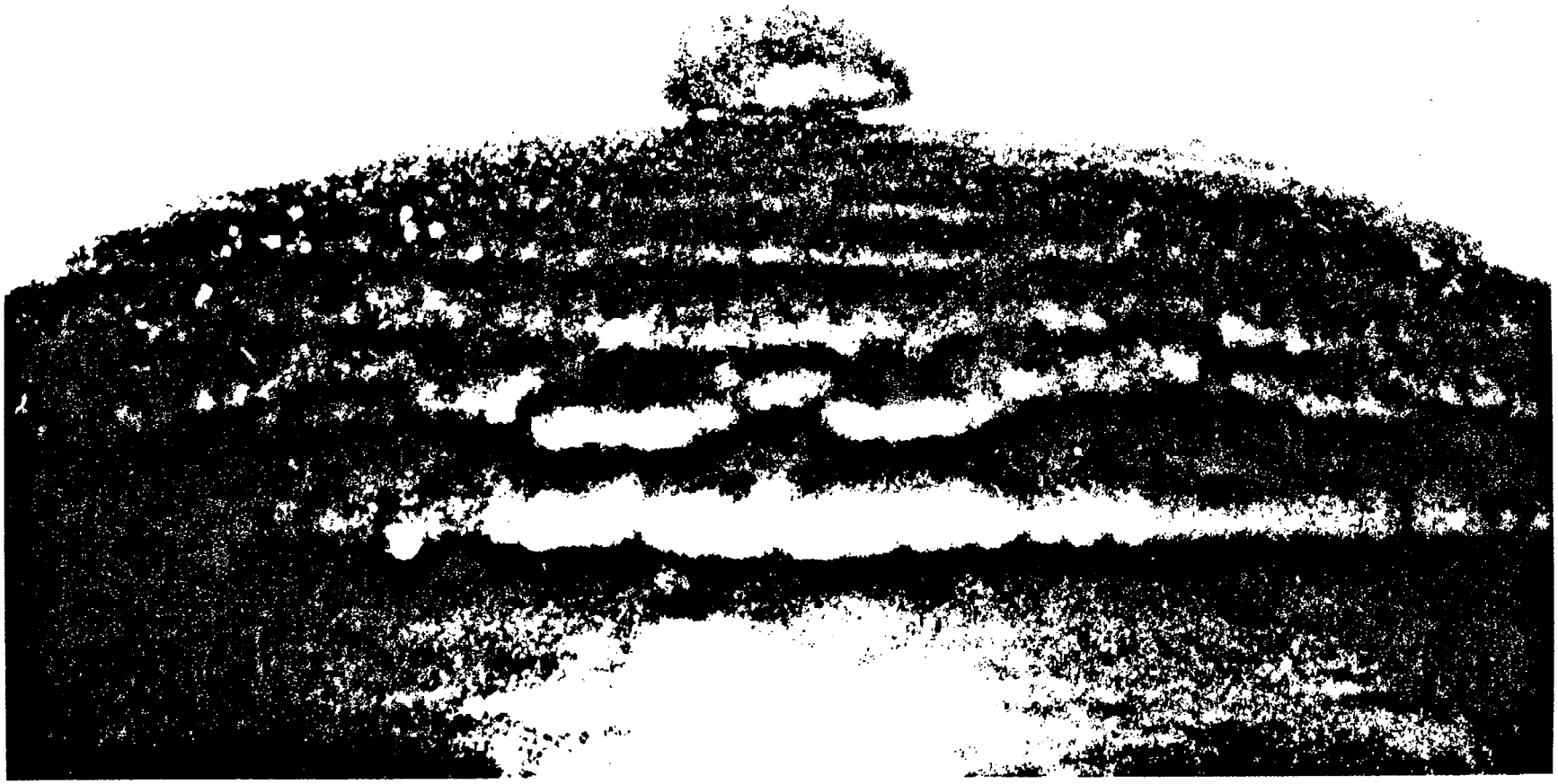

Figure 3.8 Development of surface distortions on secondary jet. Nozzle diameter, D = 1.27 cm.

3.3. Jet Transition.

Jet transition is the second phase in the development of an impulsively initiated gas jet in liquid. Figures 3.9 and 3.10 illustrate the sequence of events which occurs for nitrogen jets. The transition stage begins when the surface of the startup bubble is completely roughened. The gas from the nozzle penetrates the startup bubble and forms a cylindrical protrusion along the axis of symmetry, as shown at 1.2 msec in Figure 3.9. Later, the gas/liquid interface of the growing jet is roughened by azimuthal structures that form at the tip and that develop continuously as the jet lengthens. Also evident are fine-scale distortions superimposed on these larger structures. The smaller scales are of order 0.1D, while the scales of the larger structures are generally greater than 2D. Although the roughness appears randomly oriented and many length scales are present, the length scale of the smallest perturbation appears to remain relatively constant throughout the transition stage. Motion pictures of the developing jet show that the azimuthal structures move upstream, toward the base of the jet. This motion suggests that there is strong recirculating flow between the axially moving gas and the relatively stationary outer liquid and that these azimuthal structures arise through the action of the Kelvin-Helmholtz instability.

After 2.8 msec ($U_e t/D = 108$), the lateral growth of the base bubble ceases at a constant diameter of approximately 11D. However, the jet continues to grow axially. Except for the rounded tip, the cylindrical protrusion has a constant diameter of about 6.8-7.2D.

By 4 and 5 msec, the base of the jet begins to deflate, caused by a combination of the recirculating gas flow within the jet and the liquid entrainment near the nozzle. The location of the transition between the bubble base and the cylindrical protrusion becomes less distinct. At 5.82 msec, the radially inward motion can be seen to produce a slight pinching of the jet column at a downstream location of 3D. As gas continuously feeds the jet, the cylindrical protrusion

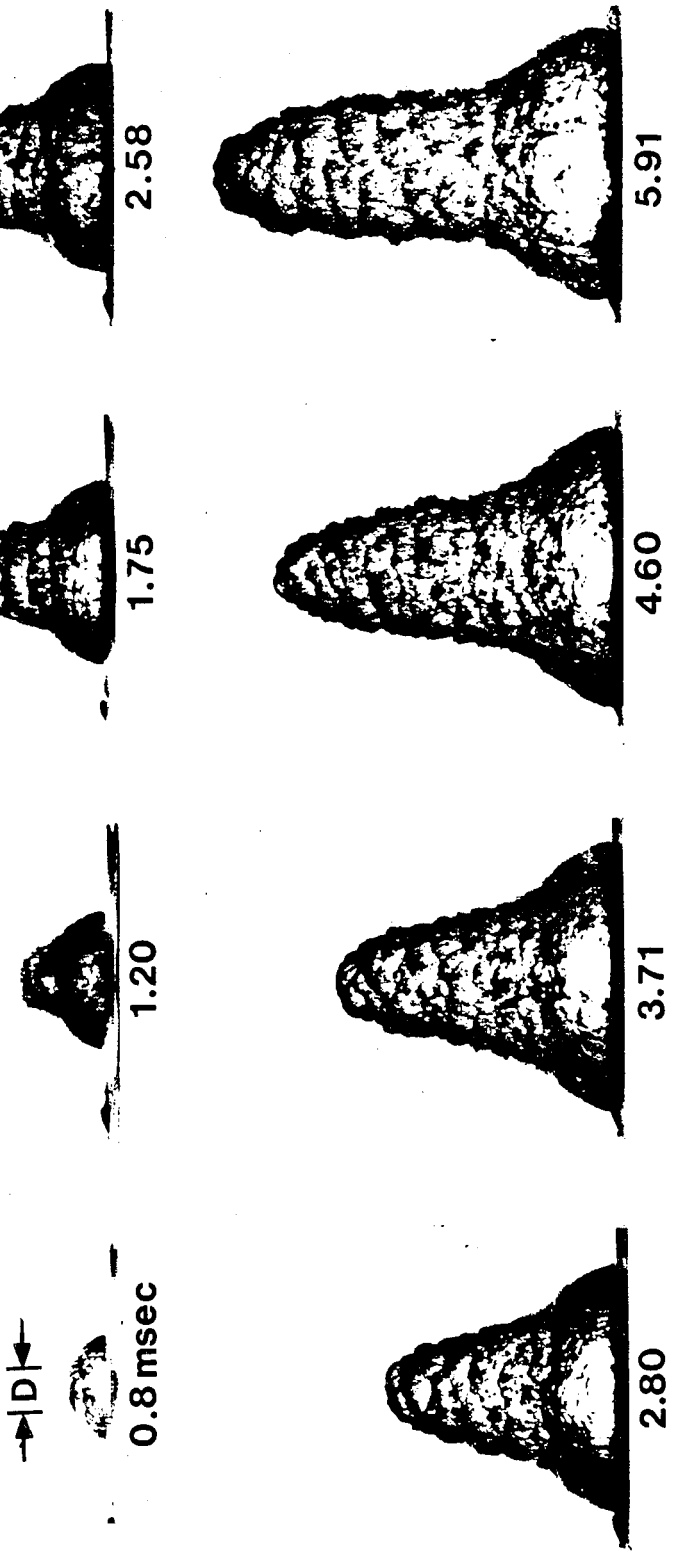

Figure 3.9 Transition stage for M_s = 1.4 nitrogen jet. Nozzle diameter, D = 1.27 cm.

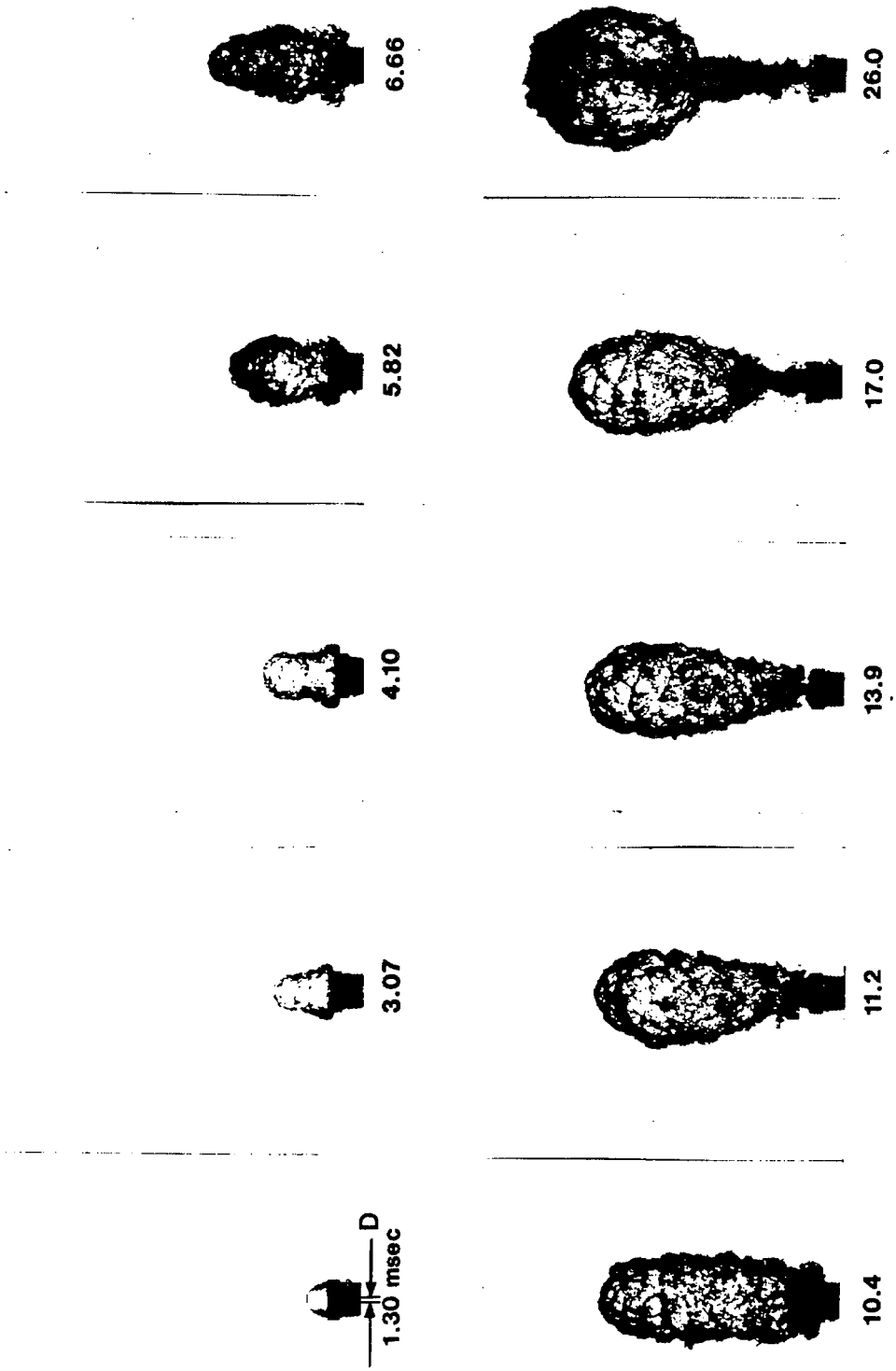

Figure 3.10 Overview of transition stage. M_e = 1.4 nitrogen jet. Nozzle diameter, D = 0.34 cm.

inflates into a large sphere, which by 10.8 msec lifts away from the nozzle. As the bubble moves downstream (at 17.0 msec), a small cloud of gas is left behind at the nozzle exit. Eventually, that cloud of bubbles is entrained into the gas column.

3.3.1. Effect of Gas Density. The development of helium and refrigerant-12 jets is compared in a series of photographs shown in Figures 3.11 and 3.12. Both jets are issuing from convergent nozzles at $M_e = 1.0$. The first noticeable difference in the two sets of photographs is the size of the growing jets. The size difference is the result of different volume flow rates. In this case, the volume flow rate of the helium jet (8.6 liters per second) is over seven times larger than that for the refrigerant-12 jet (1.2 liters per second).

However, with the exception of size, the jets have a similar appearance. During transition, each jet develops a cylindrical protrusion that grows as the axially directed flow penetrates through the startup bubble. The boundary between the gas and liquid is roughened by both large- and small-scale distortions, again on the order of 0.1-2D. When the base of the jet begins to deflate (at 2.5 to 3.5 msec for the R12 jet and after 7.45 msec for the He jet), the gas column pinches slightly (at downstream locations of $x \sim 2D$ for the R12 jet and of $x \sim 5D$ for the He jet). This is illustrated in Figure 3.11 at 19.8 and 21.8 msec, and in Figure 3.12 at 4.3 msec. At the same time, the cylindrical protrusion expands into a more spherical shape. The radially inward motion of the deflating bubble persists until eventually the jet pinches off and lifts away from the nozzle. After liftoff, a small amount of gas remains near the nozzle exit, but this remnant is slowly entrained into the jet column and is swept downstream. From 21.8-30.3 msec, the azimuthal structures on the He/water interface lose their distinct appearance as the jet deflates and lifts off (Figure 3.11). These structures are smoothed out by surface tension into a more uniform pattern of distortions with length scales of 2D.

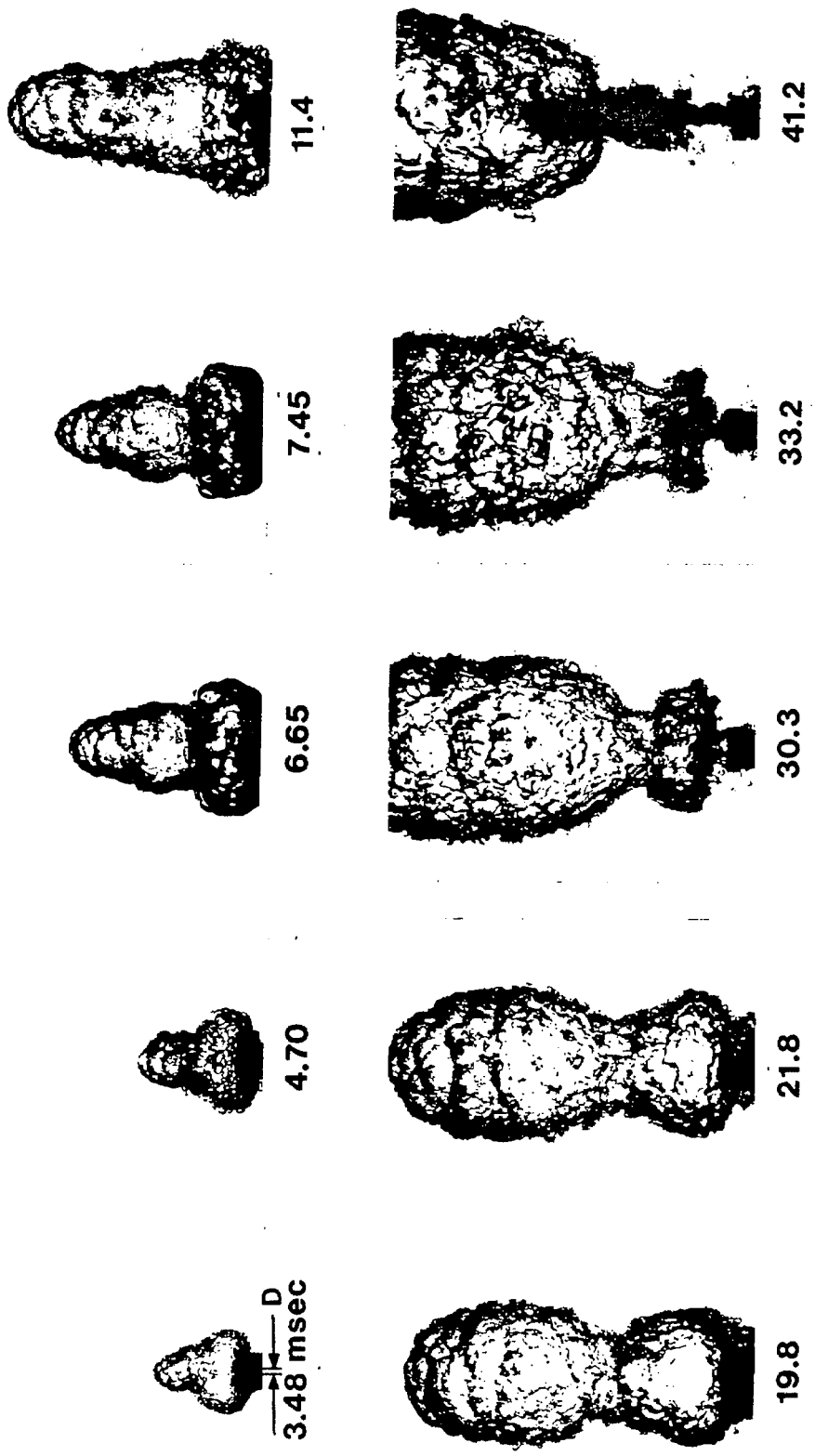

Figure 3.11 Development of M_s = 1.0 helium jet. Nozzle diameter, D = 0.32 cm.

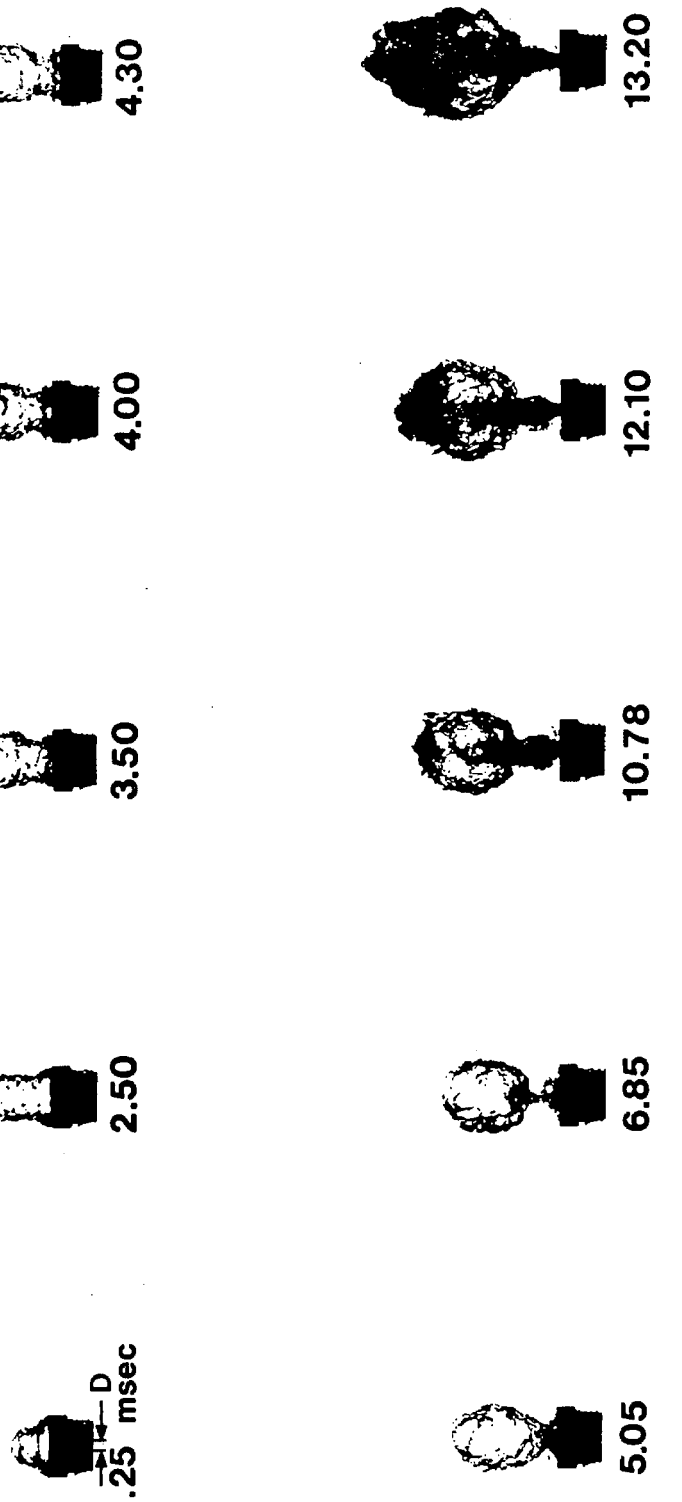

Figure 3.12 Development of M_e = 1.0 refrigerant-12 jet. Nozzle diameter, D = 0.32 cm.

The helium jet shows one other particularly interesting feature during transition. At 3 msec in Figure 3.11, the He startup bubble has grown large enough to completely surround the nozzle. This is unlike other jets whose startup bubbles do not extend beyond the baffle (see Figures 3.10 and 3.12). This unique behavior of the He jet, however, does not appear to affect its subsequent development.

At 4.7 msec, the bubble surface is covered with fine distortions (length scale ~ 0.5D), which have the appearance of small bubbles. From 4.7-6.65 msec, as both the jet and the bubble grow, the distortions become more pronounced; the length scales increase by nearly a factor of six, from 0.5D to 3D. Note that the surfaces of these now large-scale distortions are smooth and that at 6.65 msec, the startup bubble resembles a violently oscillating gas bubble just prior to breaking up into a cloud of gas. By 7.45 msec, three distinct types of surface roughness can be seen on the jet boundary: azimuthal structures at the tip of the cylindrical protrusion, fine-scale roughness at the midsection and on the azimuthal structures, and large-scale distortions on the startup bubble. Later, when the startup bubble deflates, the scales of the distortions decrease.

3.4. Global Steady State.

Steady state is the third stage in the development of a gas jet into liquid. In this stage, the gas flow is steady, and the jet spreads smoothly from the nozzle. However, it is observed that there are some conditions under which the jet is never steady, even globally. In those cases, the jet boundary exhibits large nonlinear oscillations, which frequently lead to the collapse of the gas column and the pinch-off of flow. These fluctuations often occur continuously and are much more violent than the fluctuations associated with constant-density jets. The details of this unsteady phenomenon will be discussed in the next chapter. Here, the global steady state is considered.

Figure 3.13 shows a set of typical time exposure photographs of R12, R22, N2, and He jets into water. The exposure time in each case is 1/10 sec. Except for the helium jet, all other jets have the characteristic conical spreading. The visual diffusion angles are about 24 degrees, typical of gas jets reported by other investigators (see Bell et al., 1972). The diffusion angle is defined as the angle formed by the intersection of straight lines which are visually fitted to the boundaries between the jet and ambient fluid. This is different from the spreading angle obtained based on velocity profile (e.g., see Brown & Roshko, 1974). The fact that the typical helium jet does not show the characteristic cone is due to the large-scale unsteady motion of the jet boundary. This unsteady behavior will be discussed later.

Figure 3.13 indicates that the boundaries for the R12 and R22 jets are well defined, and very little gas can be seen outside the jet cone. However, for the N2 jet, the boundary is more fragmented than the others, suggesting more extensive mixing between the gas and liquid. The fact that the lighter jet shows more vigorous mixing is consistent with the results by Tombach (1969), who studied inhomogeneous gas jets. Plotted in Figure 3.14 is the jet spreading angle as a function of operating pressure ratio, P_o/P_a. The data for the helium jet were obtained from time exposure photographs at the few test conditions where the jet was quasi-steady. At most of the operating pressure ratios considered in this study, the helium jet was unsteady. The unsteady conditions will be discussed in Section 4.3. Figure 3.14 indicates that again for all jets except helium, the range of spreading angles falls between 18-24 degrees.

While time exposure photographs show that in the time-averaged sense, a gas jet into liquid shows the characteristic spreading (in most cases), instantaneous photographs indicate that the detailed structure of the gas/liquid interface changes continuously. For example, the $M_e \approx 1.86$ nitrogen jet depicted in Figure 3.15 looks significantly different from one instant to another. The photographs indicate

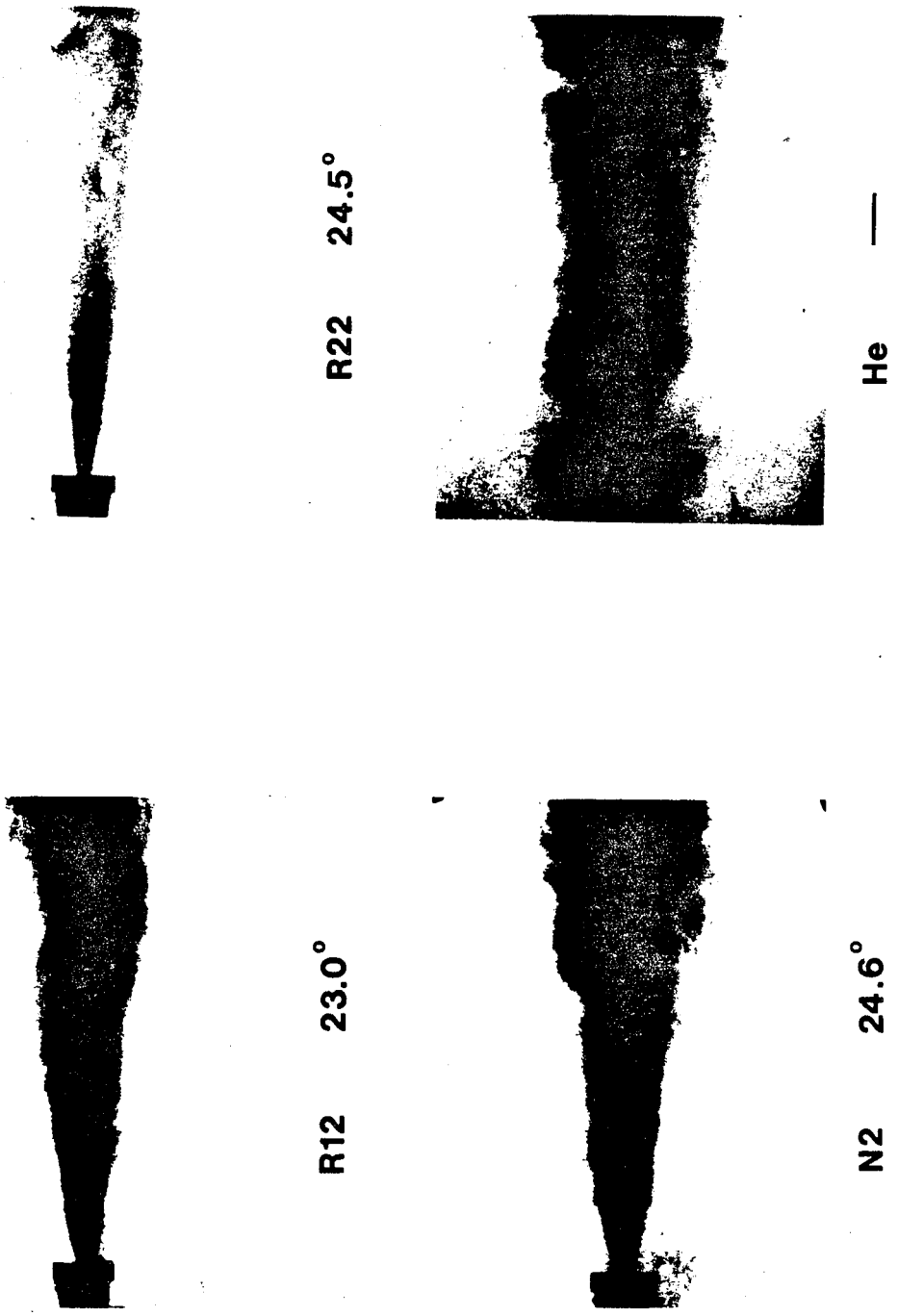

Figure 3.13 Time exposure photographs of R12, R22, N2, He jets.

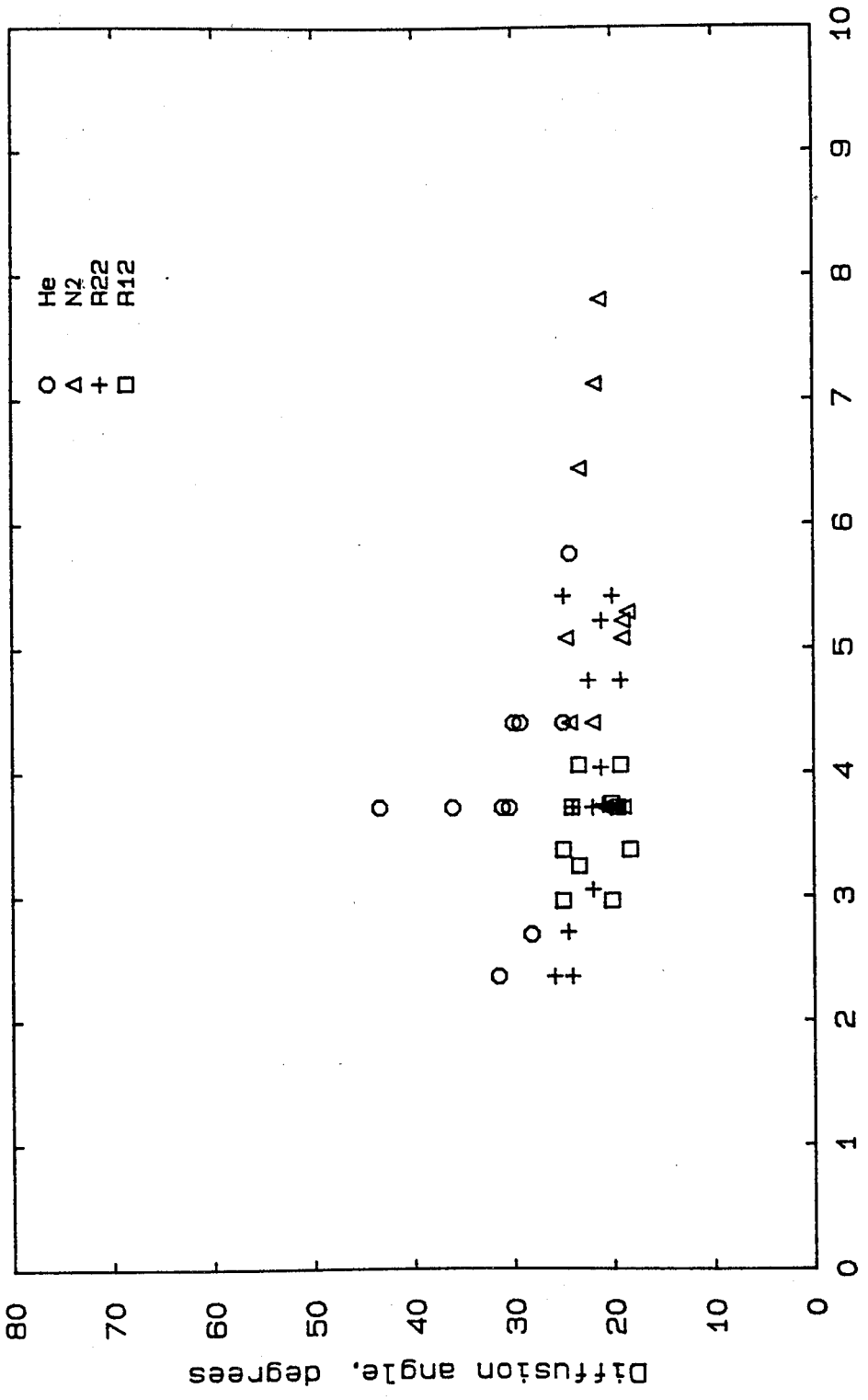

Figure 3.14 Jet diffusion angle.

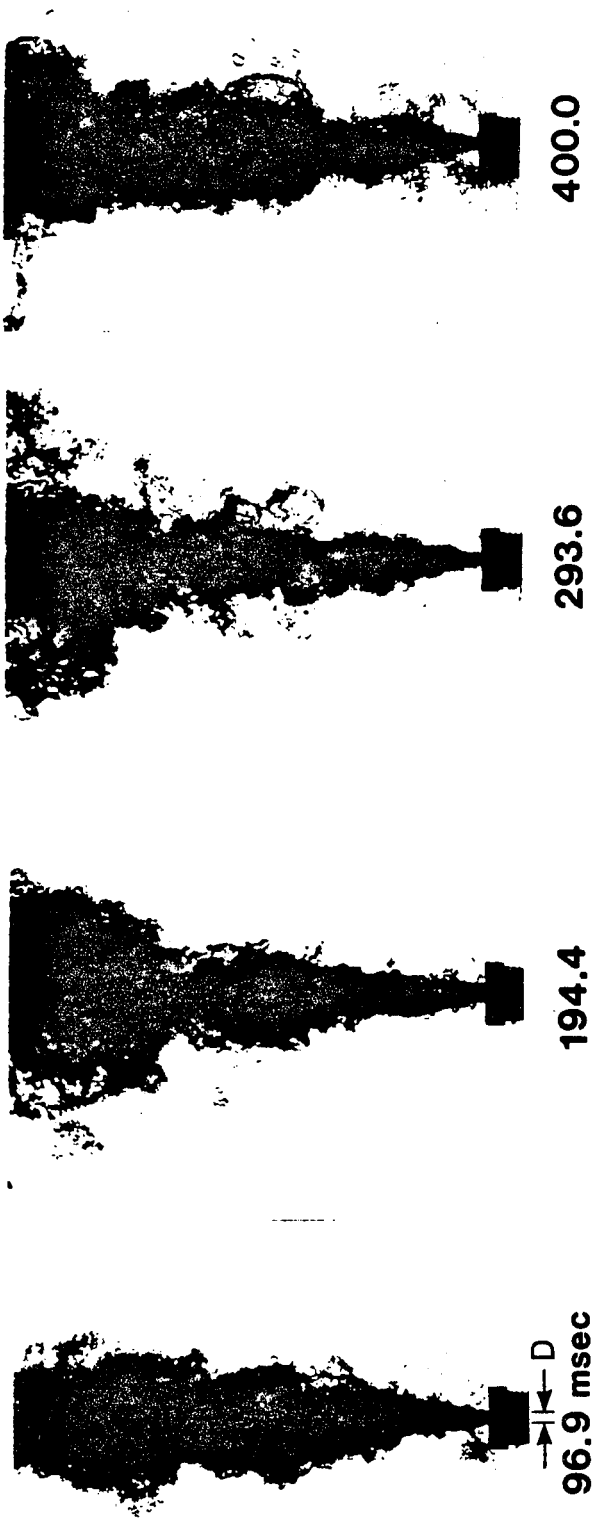

Figure 3.15 Instantaneous views of M_a = 1.86 nitrogen jet. Nozzle diameter, D = 0.38 cm.

that there is a distinct interface separating the gas and liquid for at least the first 3-4D, while beyond about 5D, a two-phase mixture forms. This is caused by extensive mixing and entrainment of liquid which occur almost immediately after the gas leaves the nozzle. The existence of small gas bubbles near the nozzle exit, as shown at 96.9 and 400 msec, is also indicative of this effect. Far downstream, the density contrast between the jet and ambient liquid is much reduced from what it was at the nozzle exit. The flow has also slowed substantially. Motion pictures reveal liquid droplets along the the jet axis at downstream locations beyond 8D. Measurements of droplet velocities indicate average values of 0.6-0.7 times the gas exit velocity.

The two-phase medium consists of gas bubbles of varying sizes typically on the order of 0.1D. However, a few bubbles can be as large as 8D (0.8 times the local jet diameter), as seen in the photograph at 400 msec in Figure 3.15. The boundary between the jet and surrounding liquid is greatly distorted. At one instant, a locally smooth interface (cf., left side of the photograph at 400 msec) may suggest mixing. At another instant (293.6 msec), streams of bubbles extend into the liquid, nearly perpendicular to the flow direction. Bubbles that are shed into the liquid beyond 0.5 local jet diameters remain there and slowly move downstream by buoyancy; those closer to the interface, are entrained into the jet and move with the jet velocity.

3.4.1. Pressure Signal. Figure 3.16 shows the typical pressure time history of a steady refrigerant-22 jet into water. In this case, the exit Mach number is 1.77. Three signals are shown. The first is the overpressure at the gas reservoir, P_0; the second is the pressure upstream of the nozzle throat, P_1; and the third is the overpressure in the water at the nozzle exit, P_2. All are normalized by the ambient pressure. Figure 3.16(a) indicates that except for the short 20 msec transient at the initiation of the flow, the normalized reservoir pressure (i.e., the operating pressure) remains nearly constant at the

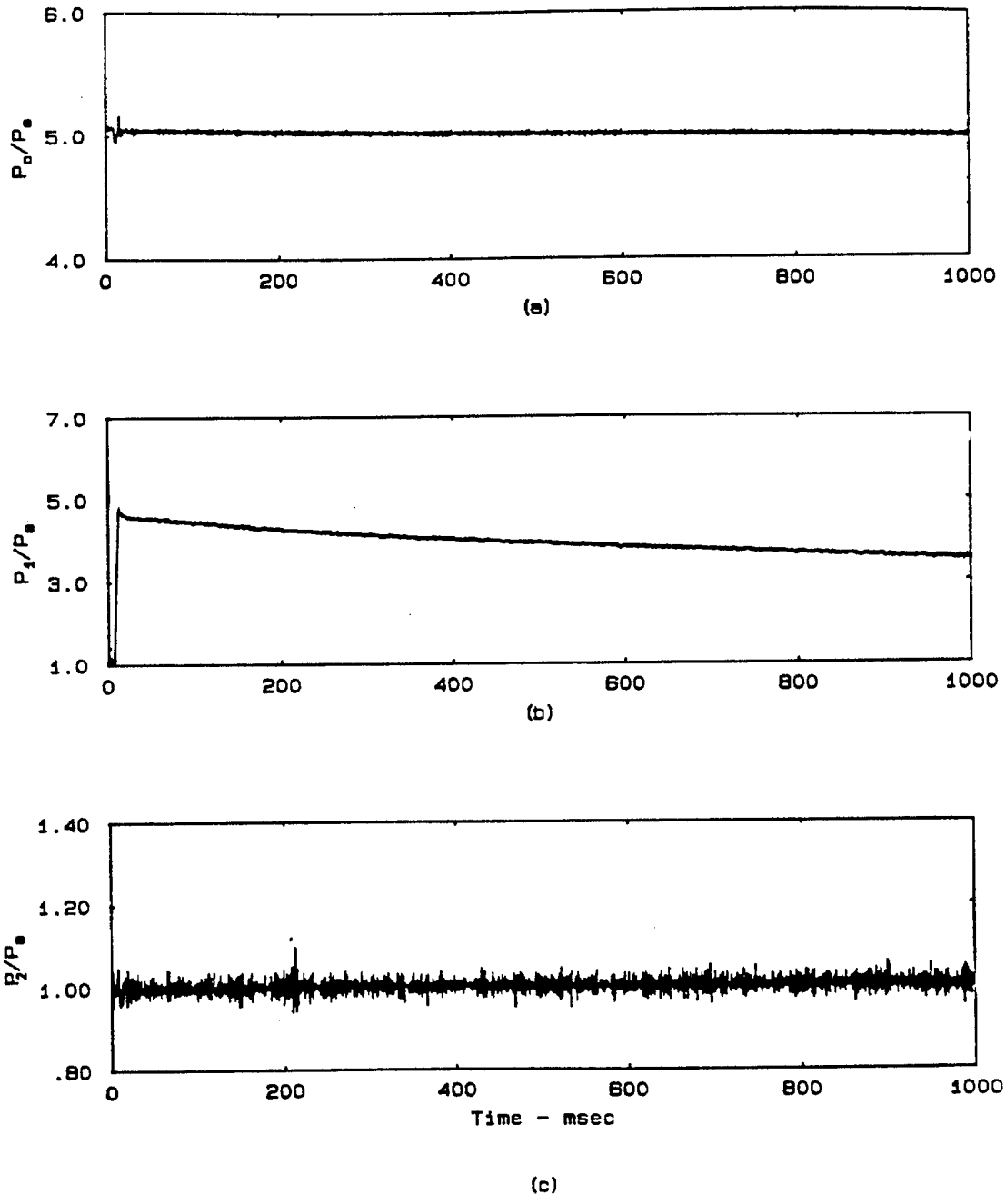

Figure 3.16 Pressure history of refrigerant-22 jet into water, $M_e = 1.77$,
(a) Reservoir pressure,
(b) Pressure upstream of nozzle exit,
(c) Pressure measured in water near nozzle exit.

starting value of 5.08. Similarly, Figure 3.16(b) shows a short transient of the normalized pressure upstream of the nozzle throat at the initiation of the flow where the pressure ratio, P_1/P_a, increases sharply from one and to slightly above 4.95. After that, the pressure is steady, decreasing gradually over the one second. The fluctuations of the gas supply and of the flow upstream of the nozzle throat are both well under 2 percent. Likewise, the signal from near the nozzle exit (Figure 3.16(c)) indicates a completely steady jet: It is constant except for the usual small pressure fluctuations associated with the turbulent jet. In this case, the fluctuations are less than 5 percent of the ambient pressure.

Note that the signals in Figures 3.16(a) and (b) show different decay rates after the initial transient. The difference can be attributed to the discharge time constant characteristic of the pressure transducers, as described in Chapter 2. In Figure 3.16(a), the pressure ratio of 4.95 at t = 1 sec is an optimistic measure of the final pressure of the reservoir. In Figure 3.16(b), P_1/P_a of 3.6 at one second is less than the actual upstream pressure.

The pressure history of an M_e = 2.02 nitrogen jet is shown in Figure 3.17. Like those of the R22 jet, the pressure of the gas reservoir and of the flow upstream of the nozzle (Figures 3.17(a) and (b)) is steady. However, it is evident that the fluctuations outside the exit are larger. The pressure changes are generally on the order of 10 percent but can be as large as 15 percent, as at 30 msec and 580 msec. These large fluctuations are consistent with behavior of the nitrogen jet suggested by the flow visualization. In particular, as shown in Figure 3.14, the boundary of the N2 jet is more fragmented than that of the R22 jet, suggesting greater motion at the N2 jet boundary

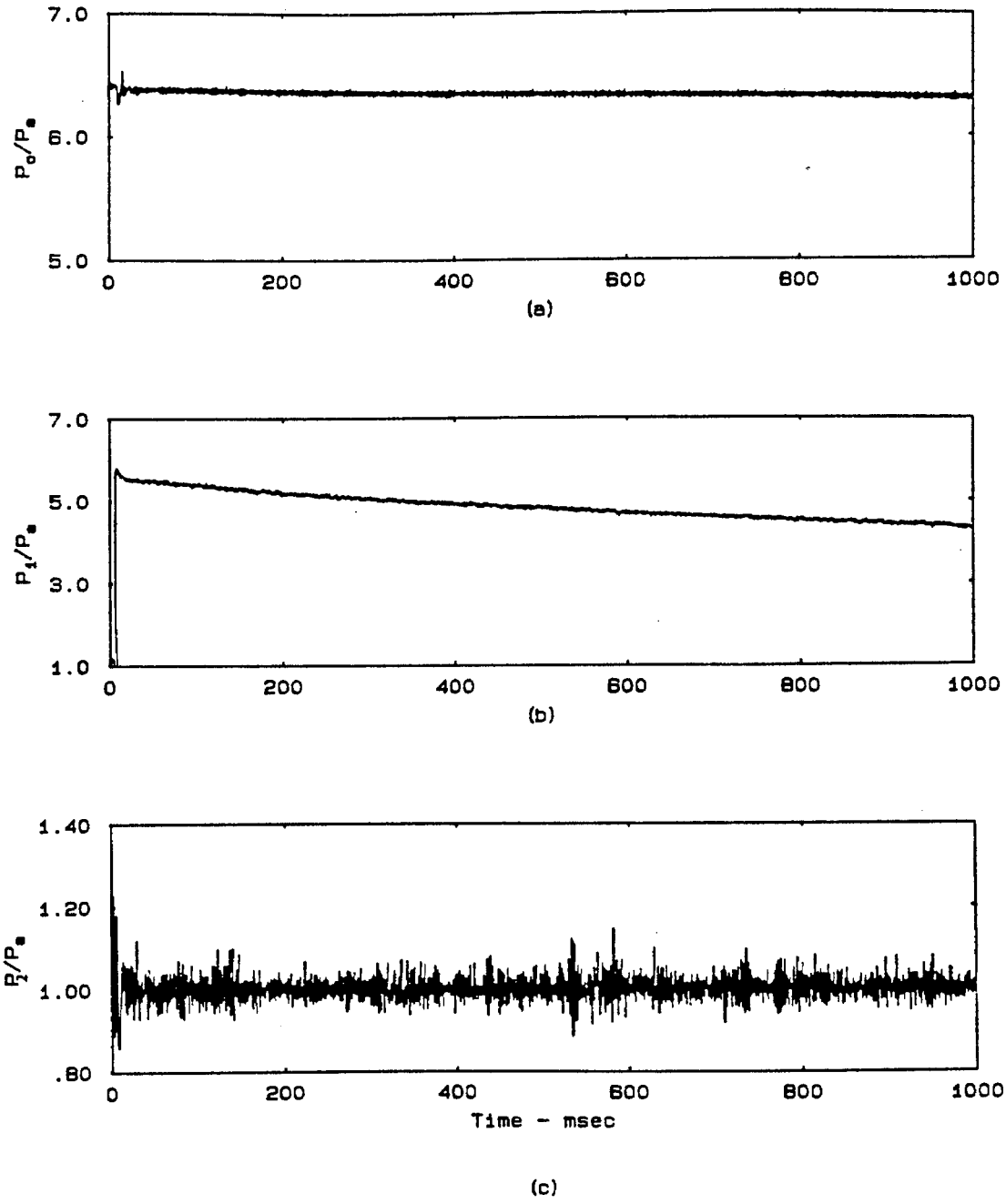

Figure 3.17 Presure history of nitrogen jet in water, M_e = 2.02,
(a) Reservoir pressure,
(b) Pressure upstream of nozzle exit,
(c) Pressure measured in water near nozzle exit.

3.4.2. Centerline Velocity Correlation. Estimates of the local jet velocity at different locations along the axis were made by following the motion of liquid droplets and of gas bubbles in sequential frames of high-speed films. The results indicate that the velocity decreases significantly with downstream distance. Given this fact, an effort was made to determine whether the measured centerline velocities, U_c, for these two-phase jets can be correlated in a manner similar for conventional jets (i.e., single-phase jets of gas into gas).

Similarity and dimensional arguments for momentum driven jets (e.g., see Chen & Rodi, 1980) predict the decay of centerline velocity and density (or temperature) to scale with

$$\frac{U_e}{U_c} \sim \frac{x}{D^*} \tag{3.3}$$

where

$$D^* = \left[\frac{\rho_j}{\rho_a}\right]^{1/2} D \quad .$$

Strictly speaking of course, the scaling laws are valid only when the densities of the jet and of the ambient fluids are approximately equal ($\rho_a/\rho_j \simeq 1$). However, if there is extensive mixing of jet and ambient fluids, far downstream, the local density ratio, ρ_a/ρ_j becomes close to unity and the scaling laws may be applicable (see Ricou & Spalding, 1961). Kerney et al. (1972) found Equation (3.3) to be applicable for steam jets into water. His measurements of U_c in the region downstream of the point where condensation is complete show direct correlation with x/D^*. Avery & Faethe (1974) showed that, in fact, Equation (3.3) is valid for a wide variety of jets. The scaling constant was found to be between 0.10 and 0.14.

Figure 3.18 shows the correlation of the normalized jet mean centerline velocity, U_e/U_c, with the scaled downstream distance, x/D^*. The experimental data of the present study and the scaling constants determined by three different investigators are shown. The scaling constant by Chen & Rodi is a recommended value based on data from many researchers. The approximate scatter of the data by Avery & Faethe and by Kerney et al. are noted by the vertical bars. The figure indicates that the measured velocity ratios are reasonably well correlated with x/D^*, although, as might be expected from the method used here, there is substantial scatter for R22 and R12 jets. For example, at $x/D^* \sim 100$, where the correlation is poor, most likely the jet and ambient fluids are not sufficiently well mixed such that ρ_a/ρ_j is still large and the scaling is thus invalid. Note that, although the effective scale is $x/D^* \sim 100$, the actual value of x/D is only about 6. However, at larger values of x/D^*, the correlation is better. In addition to insufficient mixing, the discrepancies for R12 and R22 jets may also be partially attributed to lack of clarity in the high-speed movies from which velocity data were obtained. Often it was difficult to distinguish clearly the liquid droplets within the gas column. Therefore, the measured velocities may not be reliable.

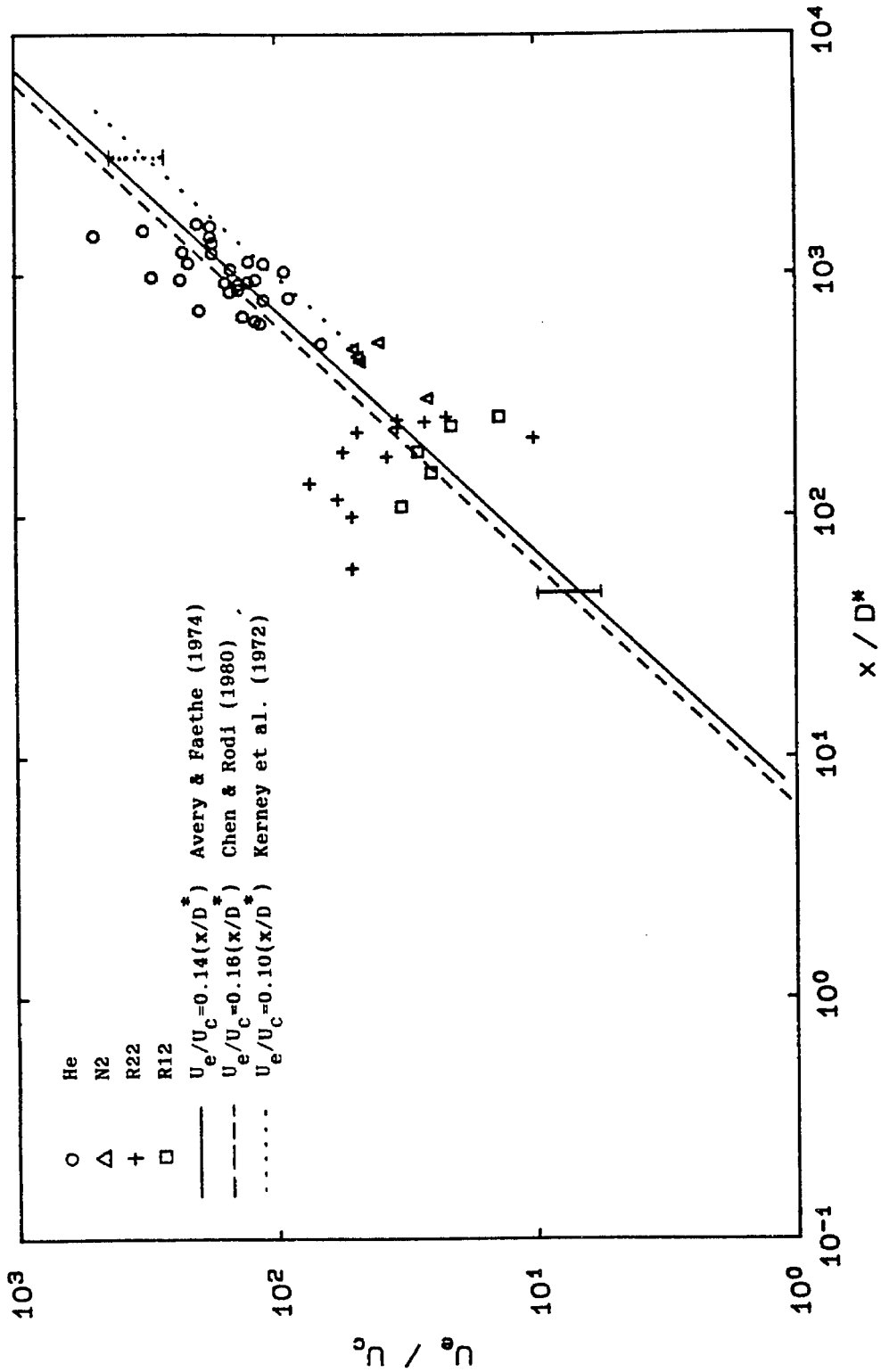

Figure 3.18 Correlation of centerline velocity.

Chapter 4
UNSTEADY BEHAVIOR

4.1. Introduction.

In the last chapter, the stages of development for gas jets into liquid were presented. It was noted that, under some conditions, the steady state is never achieved. Instead, the jet exhibits "chugging." While chugging is often associated with strong oscillations in the source reservoir, in the present case, this is not so. Here, chugging is a large-scale oscillation of the jet boundary which leads to the collapse of the gas column followed by an explosive outward burst of gas. The frequency and the amplitude of the oscillations are strongly dependent on the flow condition of the jet.

In this chapter, the unsteady behavior is discussed. In particular, three issues are addressed: (1) the character of the unsteady motion, (2) the conditions under which the unsteadiness occurs, and (3) the mechanism responsible for the behavior.

4.2. Character of Jet Unsteadiness - Chugging.

Figure 4.1 shows a sequence of frames from a high-speed movie of a nitrogen jet in water in which a single chugging event occurs. Actually, chugging rarely occurs as a single event; usually, it occurs as a series of intermittent events. Isolated events take place only when the jet is mildly unsteady. In this case, the exit Mach number is 2.02, and the operating pressure ratio is 5.08. The first (top) photograph in each vertical strip is frame (a); the middle and bottom photographs are frames (b) and (c), respectively. The frames are 0.25 msec apart, and the time corresponding to frame (a) in each strip is listed.

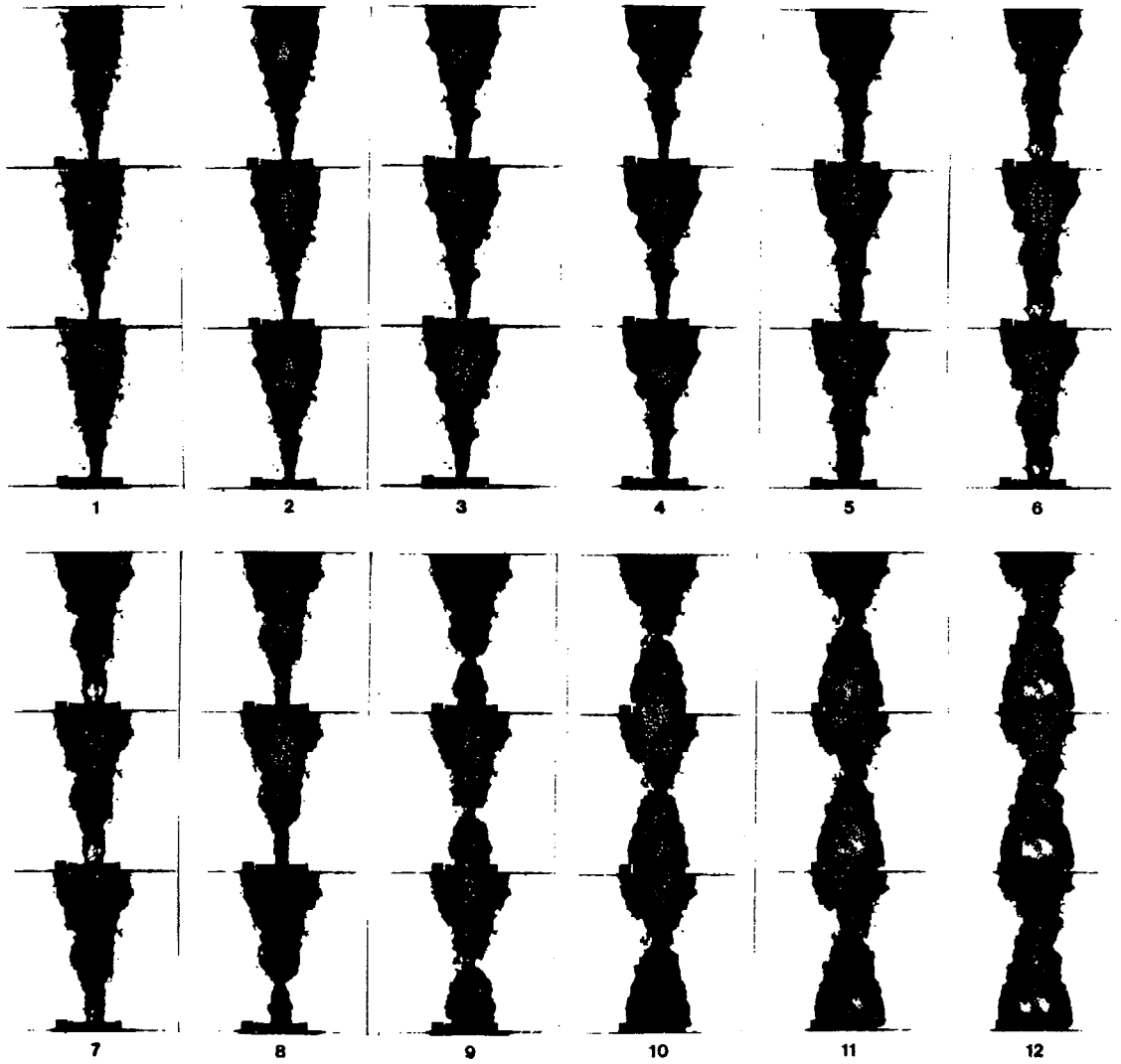

TIME (msec)

1a)	566.75
2a)	569.00
3a)	569.75
4a)	570.50
5a)	571.50
6a)	572.00
7a)	572.75
8a)	573.50
9a)	574.25
10a)	575.00
11a)	575.50
12a)	576.25

5cm

Figure 4.1 Chugging event for nitrogen jet at M_e = 2.02 and P_o/P_a = 5.08. Nozzle diameter = 0.42 cm.

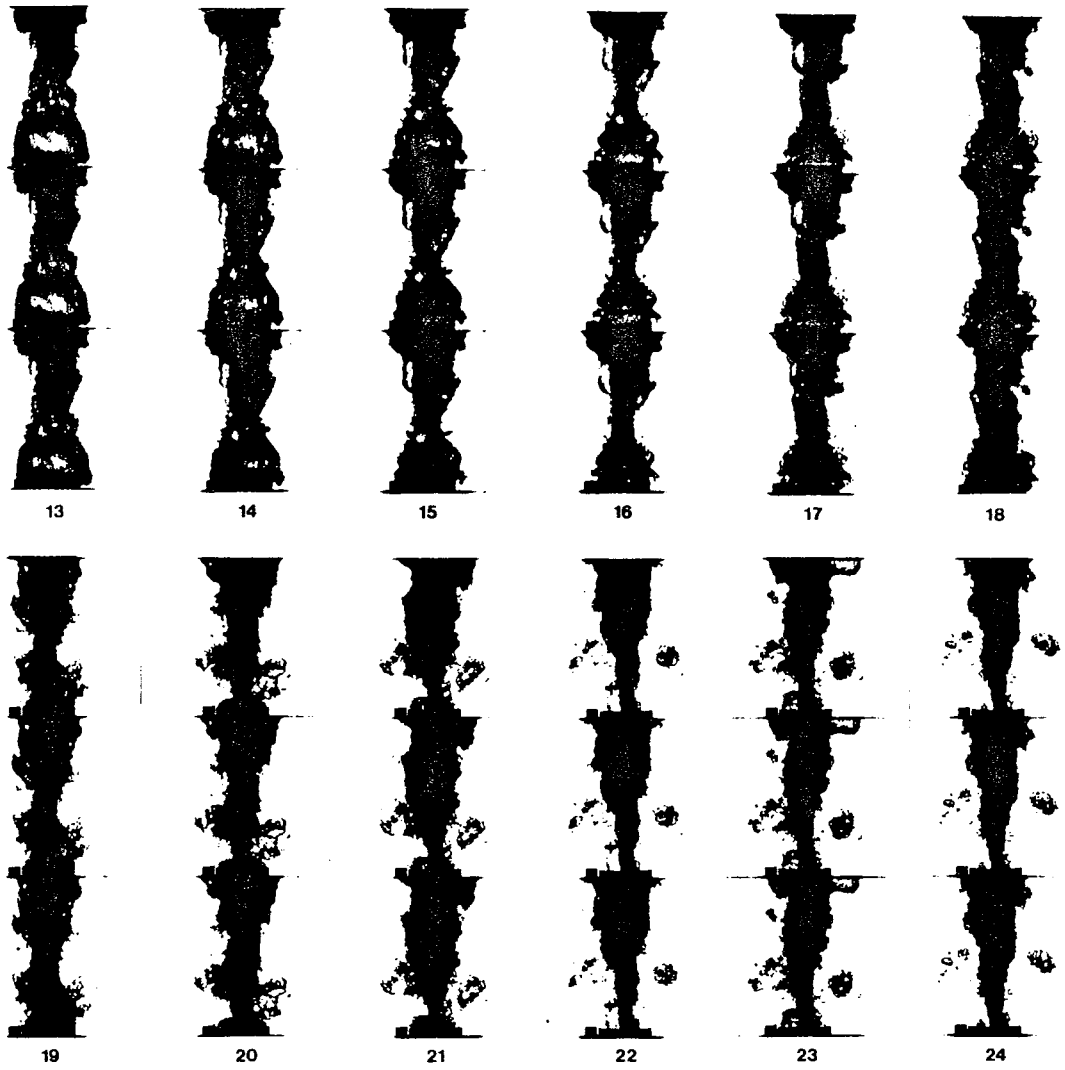

TIME (msec)	
13a)	577.00
14a)	577.50
15a)	578.50
16a)	579.25
17a)	580.50
18a)	582.00
19a)	589.75
20a)	600.00
21a)	611.75
22a)	624.75
23a)	651.00
24a)	675.25

Figure 4.1 continued

In the first six frames (1a-2c), the jet appears normal and steady, and the gas diffuses smoothly downstream of the nozzle with a spreading angle of 20 degrees. By frame 3a, however, the jet develops an atypical feature; it expands more widely than in the six previous photographs and produces a bulb-like structure approximately 2D in size immediately downstream of the nozzle exit. This structure quickly deflates, in less than 0.5 msec as illustrated in frames 3a-4a. As the gas column reaches its minimum diameter in frame 4a, the flow is constricted and pressure builds up locally. This overpressure causes a second expansion of the gas column, one that is much stronger than the first, as illustrated in frames 4c-8a. The enlargement grows to a maximum diameter of 5D and shows large-scale wrinkling on its surface. This outward motion of the jet is so severe that on the rebound, liquid is driven onto the axis and the jet completely collapses at one point, pinching off the flow (frame 9a) at a streamwise location of 6D. This pinchoff distance is comparable to the maximum jet width prior to collapse. The radially inward velocity of the interface is approximately 10 m/sec.

While the jet initial region expands and deflates (strips 3-7), the downstream portion appears to be unaffected. The gas column, say, in strips 5 and 6, has the appearance of a cylindrical channel of length about 10D, downstream of which the effective boundary of the channel diverges. This idealized shape will be used later to show how a pressure difference between the jet and surrounding liquid can arise, which can cause the jet to collapse and to pinchoff.

Once the pinchoff is complete, the residual gas moves downstream, and an inflating bubble is left at the nozzle exit (frame 9c). The jet then reinitiates under the influence of the high momentum gas from the nozzle (frames 10 and 11). By frame 11c, the startup bubble merges with the residual jet and forms a continuous path for the outgoing gas. The lateral growth ceases, and the size of the bubble base remains relatively constant at 7D (strips 12-13). The startup bubble gradually

deflates and is slowly entrained into the gas column (pictures 14-17). In frame 16, the jet appears to deflate beyond the equilibrium diameter, but in frame 17, it rebounds slightly. A cluster of bubbles is left behind, as shown in pictures 18-21. By strip 22, the jet returns to the steady state. The only sign of the collapse is the cloud of bubbles near the nozzle. The last few frames show little change, emphasizing the fact that the liquid outside the jet has become stationary. To the right of the jet, a large gas bubble, which has been shed into the liquid, moves slowly downstream, driven only by buoyancy.

The jet pinchoff occurs at nearly the same streamwise location for all gases and flow conditions. Plotted in Figure 4.2 is the jet pinchoff location as a function of the density ratio. The vertical lines represent the range of values observed for different realizations of the jet. Two features are evident from the figure. First, the range of pinchoff distances is broad, but in all case, the values fall between 4 and 10D. Second, the pinchoff distance increases slightly with increasing density ratio. Since this pinchoff height is about equal to the width of the jet prior to collapse, it would be expected that for lighter jets, chugging would be more violent; that is, the expansion of the gas column is wider and the collapse more severe. This expectation was confirmed by experiment; lighter jets do in fact exhibit greater lateral growth (see Figures 3.11 and 3.12) and stronger chugging than heavier jets.

4.2.1. Pressure Signal. Figure 4.3 shows the pressure history of the chugging event pictured in Figure 4.1; given is the pressure measured in the water near the nozzle exit normalized by the ambient pressure as a function of time. The numbers shown correspond to the strips of photographs in Figure 4.1. Prior to the onset of unsteadiness (before 569 msec, #2), the pressure is constant except for the small fluctuations of the turbulent jet, which are less than 5 percent. When chugging is initiated at 570 msec (#3), the pressure falls slightly

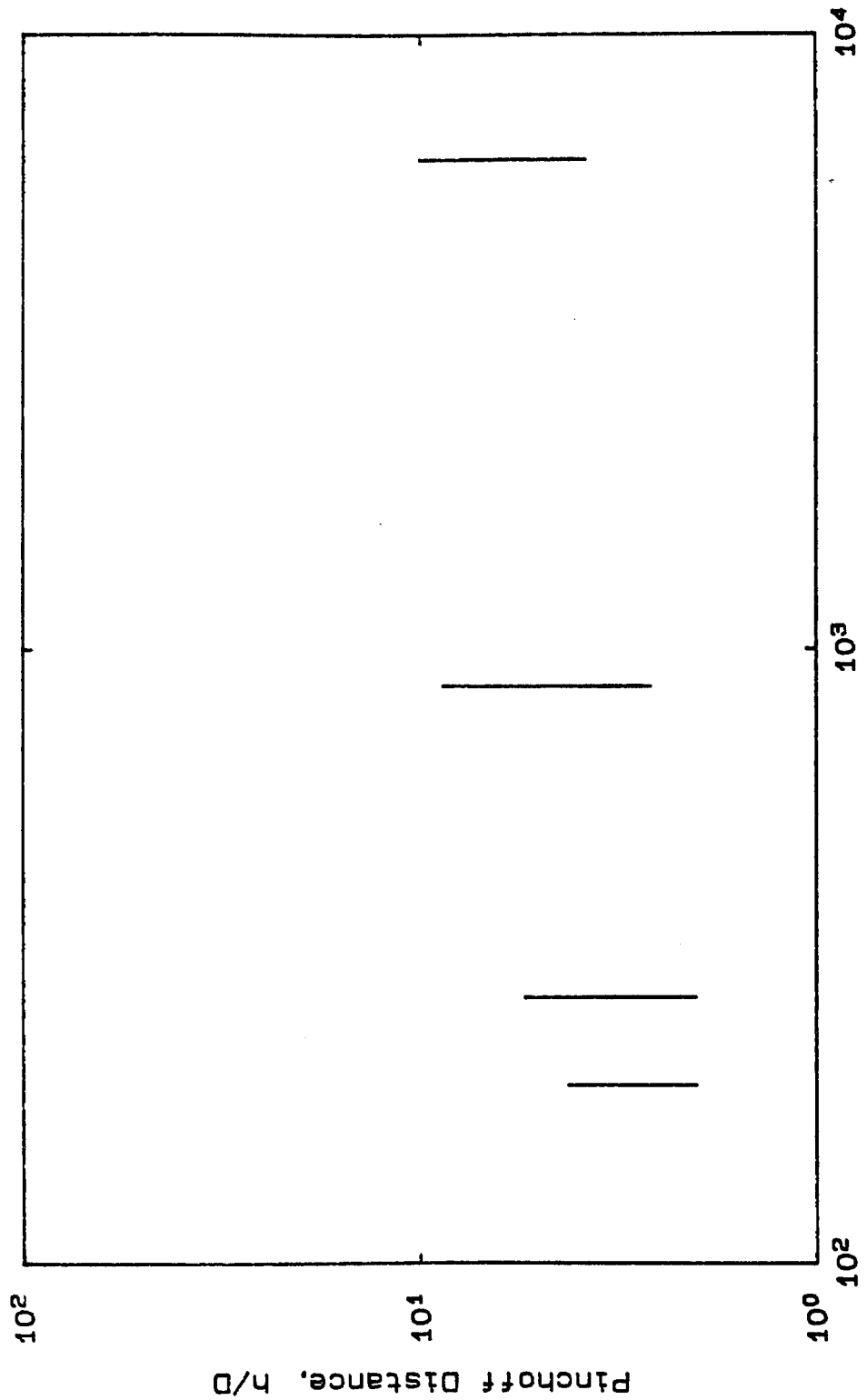

Figure 4.2 Pinchoff location as a function of density ratio.

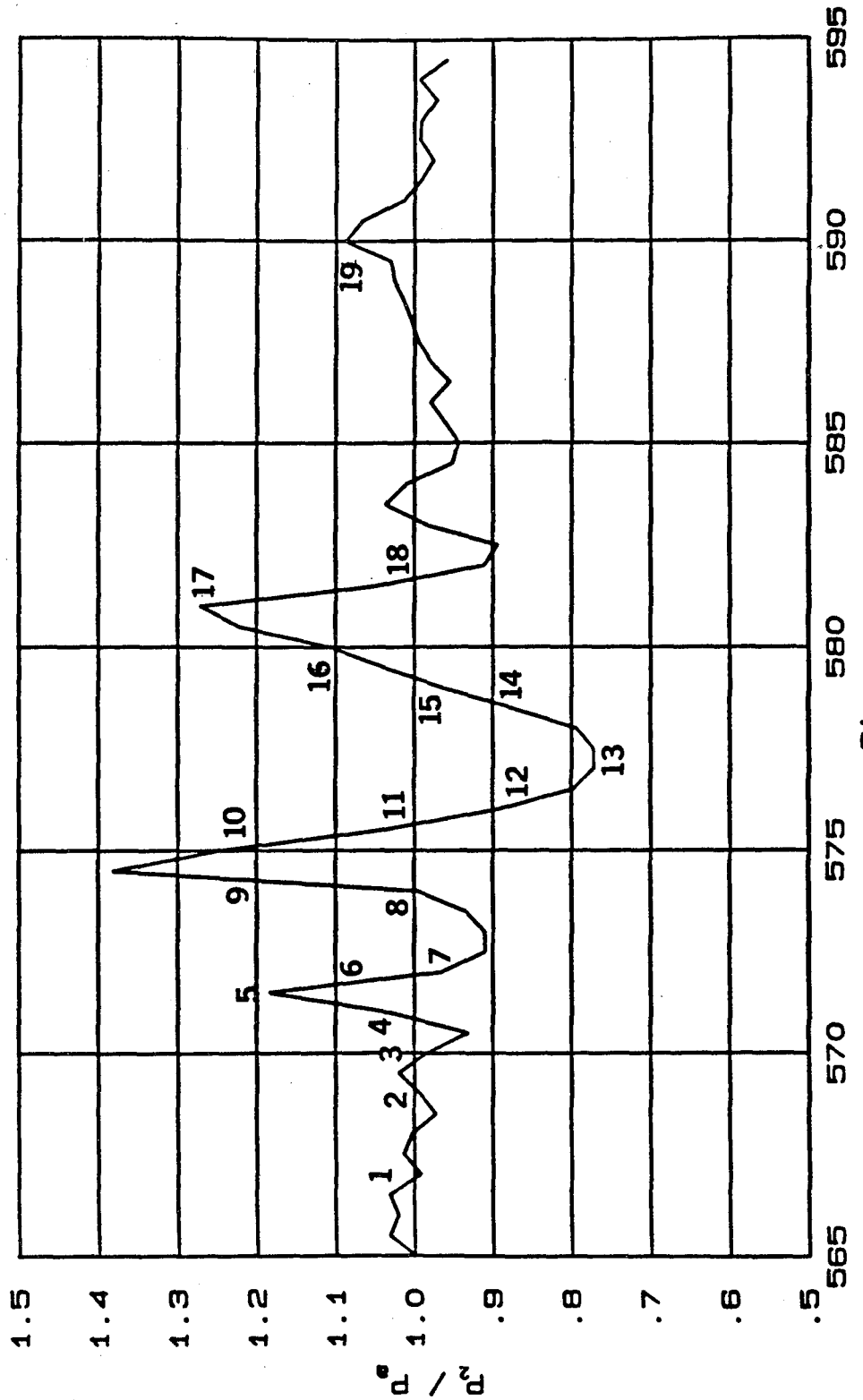

Figure 4.3 Pressure response of chugging event for nitrogen jet, $M_e = 2.02$, $P_o/P_a = 5.08$.

below the ambient, reflecting the first atypical expansion of the gas column. The pressure rise following this decrease coincides with the pressure buildup in the jet as the column deflates and reaches its minimum diameter at 571 msec (#5). The jet then expands, blowing the second bubble. As the bubble grows, the pressure rapidly falls below the ambient, reaching its minimum value of 0.9 as the bubble radius reaches its maximum of about 2.5D (#7). The bubble then collapses, and the pressure rises again (#8 and #9). The jet pinches off completely at 574.25 msec. The pinchoff constricts the flow of gas from the nozzle, causing the pressure to increase sharply, thus, producing the second peak in the signal. This increase to 40 percent overpressure provides the driving force for an explosive reinitiation of the jet. As the startup bubble develops, the pressure falls off rapidly. When the outgoing gas penetrates and merges with the residual jet at 576 msec (#12), the pressure reaches minimum. Then, as the flow becomes axially directed and as the startup bubble slowly deflates due to recirculation and entrainment, the pressure rises again, overshooting ambient pressure as the jet deflates slightly beyond the equilibrium diameter (#16 and #17). After approximately 10 msec, the jet restabilizes and the pressure returns to one atmosphere.

The three peaks in the pressure signal (Figure 4.3) are remarkably repeatable from one event to the next and can be conveniently used as a marker of chugging. For comparison, the pressure signals for four chugging events are given in Figure 4.4. Although each signal is the response of a different jet, the qualitative features of the traces are similar. For example, each signal shows three pressure peaks. In each case, the first peak is the smallest. It is followed by a second, much stronger spike, and then a third, broader fluctuation. The time scale for the chugging event, that is, the time from the first peak to the third, is nearly constant at approximately 7.5-9 msec.

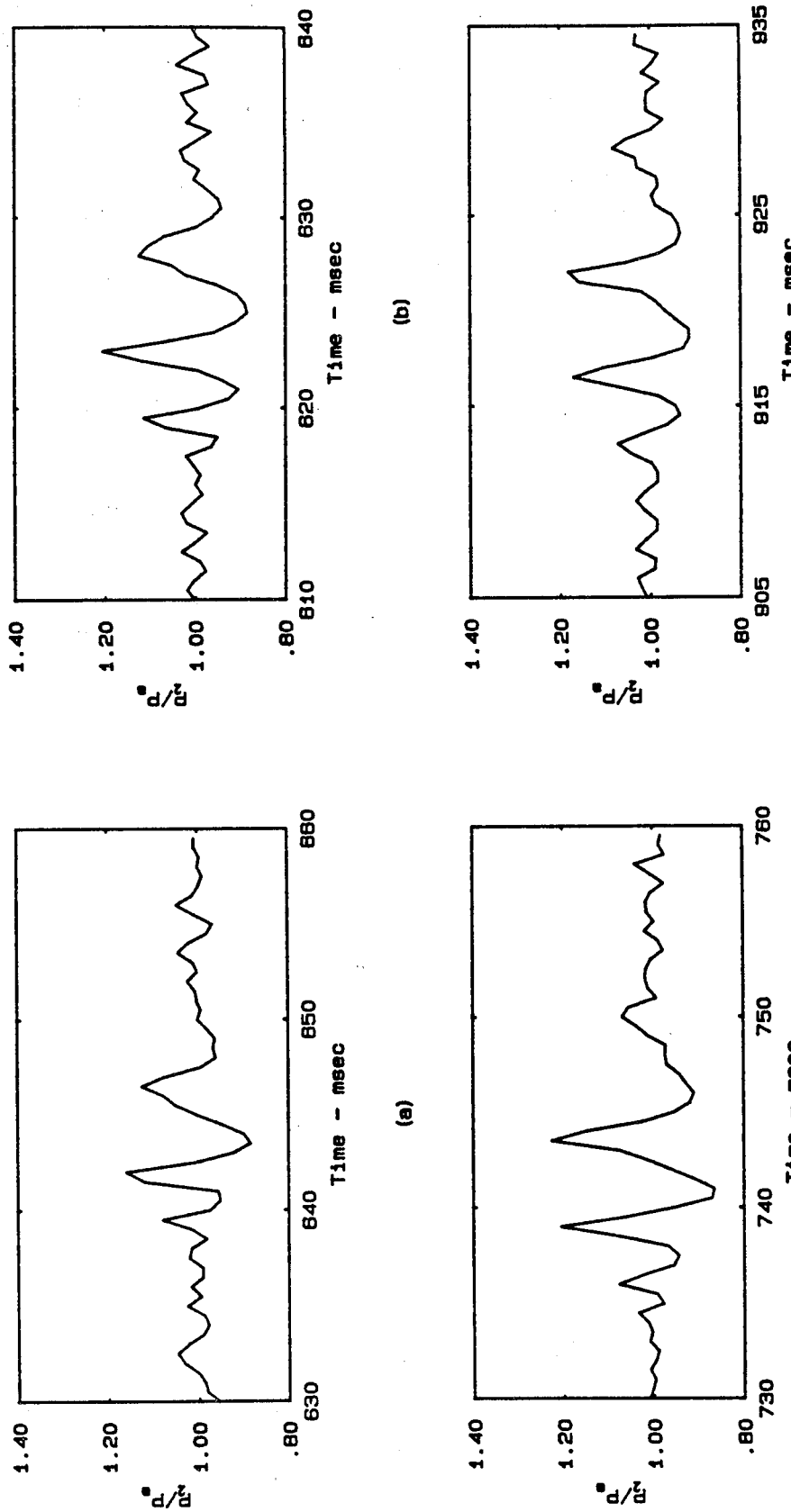

Figure 4.4 Comparison of pressure signals of chugging,
(a) R12 jet, P_o/P_a = 5.08 , (b) R22 jet, P_o/P_a = 3.72,
(c) N2 jet, P_o/P_a = 5.08 , (d) He jet, P_o/P_a = 3.72.

The typical pressure histories for an M_e = 1.0 nitrogen jet into water is shown in Figure 4.5 (compare with Figure 3.16 or 3.17). The most notable difference between Figures 3.16 and 4.5 is the large pressure fluctuations (some up to 25 percent) of the nitrogen jet appearing intermittently in the third trace. On close examination, they are found to be randomly spaced occurrences of three pressure maxima, signaling chugging events as described above. For example, one event is clearly distinguishable at 400 msec. Note that, although Figure 4.5(c) clearly shows chugging, the pressure signals at the reservoir and upstream of the nozzle throat (Figures 4.5(a) and (b)) show no fluctuations whatsoever: Both traces indicate nearly constant pressure except for the transient at the jet initiation.

There is no preferred frequency for the large fluctuations shown in Figure 4.5(c). This was found true for other jets at various test conditions. Some jets however, show larger and more frequent fluctuations; the tendency toward this behavior depends on the type of gas and on the flow conditions. In some cases, for example, for light jets, the fluctuations can often be as large as 70 percent, although more typically, the changes are on the order of 20 percent.

Experimental results indicate that high Mach number jets show many fewer chugging events and smaller pressure fluctuations than low Mach number jets. A comparison of the histories of the pressure just outside the exits of M_e = 1.86 and M_e = 1.0 nitrogen jets are shown in Figure 4.6. The M_e = 1.86 jet is clearly more steady than the sonic jet. While only about six events occur during the one second duration of the M_e = 1.86 jet, well over 10 occur in the same time span for the sonic jet. Also, the peak overpressure for the M_e = 1.86 is slightly less than that for the sonic jet (30 percent of the ambient pressure as compared with 38 percent, respectively).

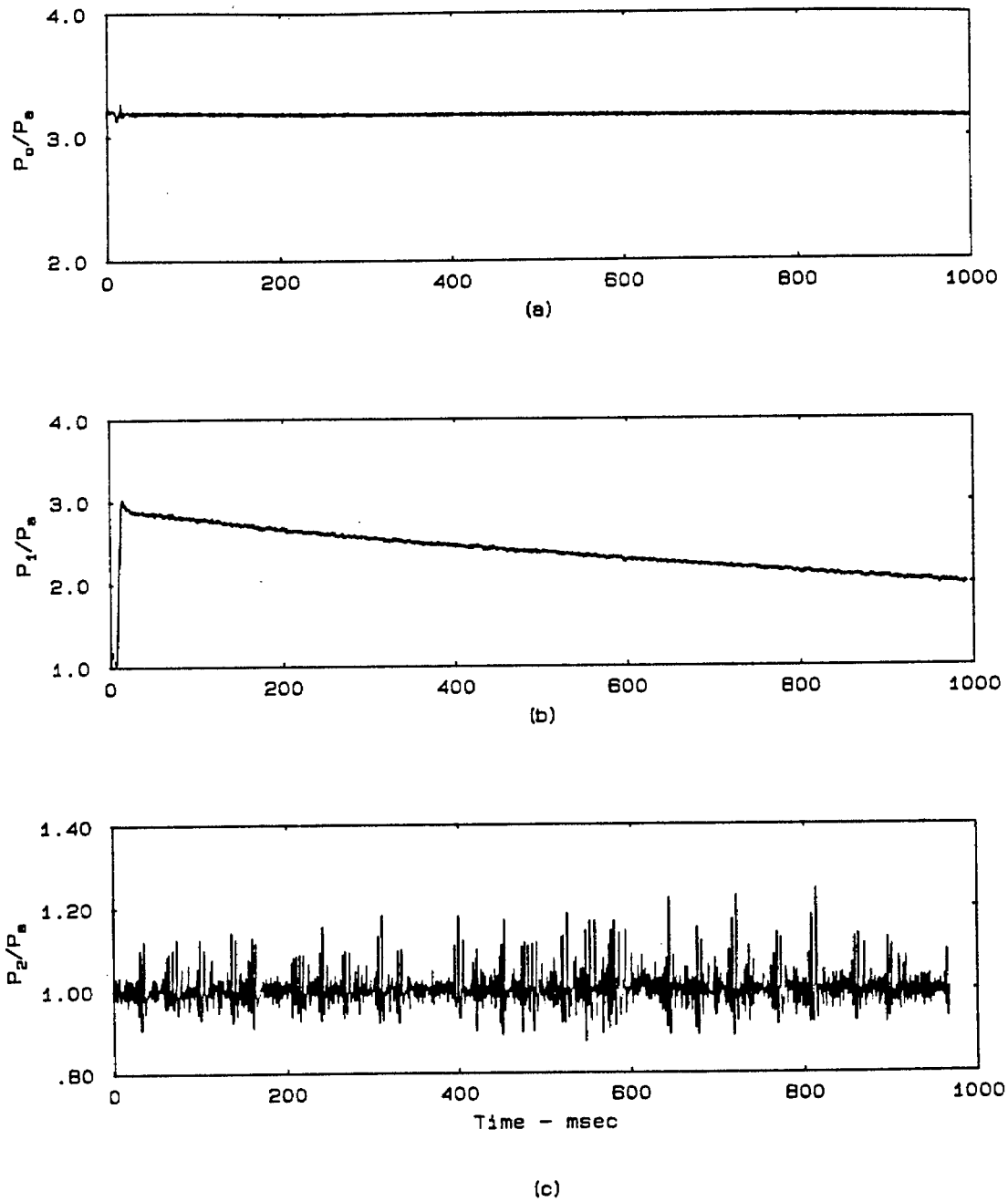

Figure 4.5 Pressure history of an M_e = 1.0 nitrogen jet,
(a) Reservoir pressure,
(b) Pressure upstream of nozzle throat,
(c) Pressure measured in water near nozzle exit.

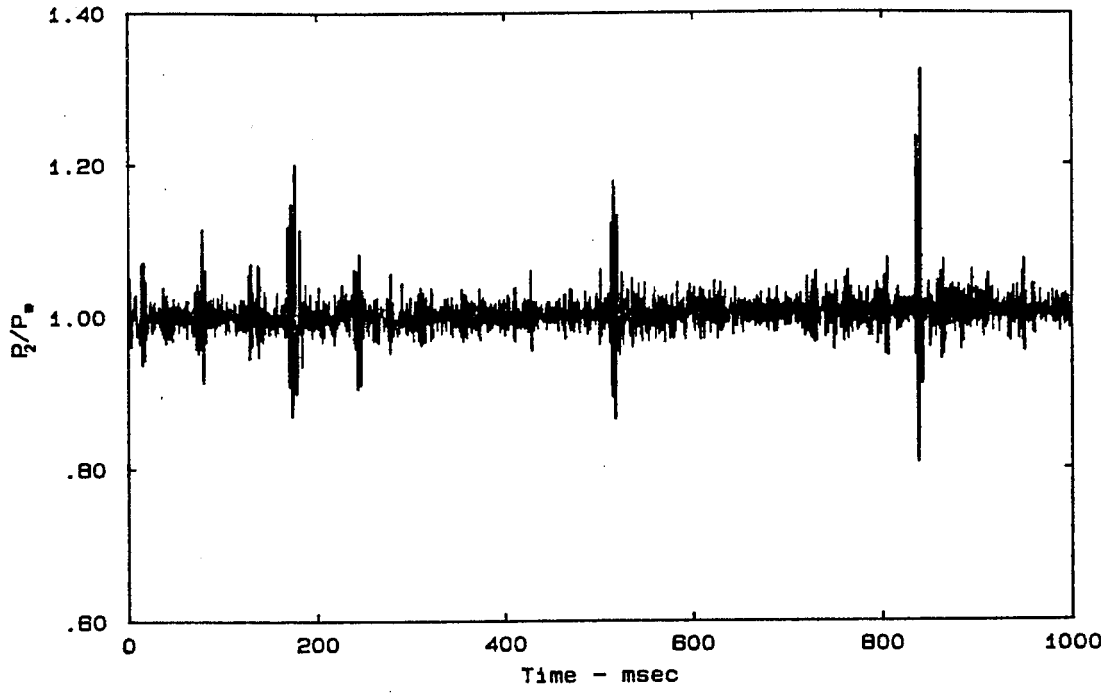

(a)

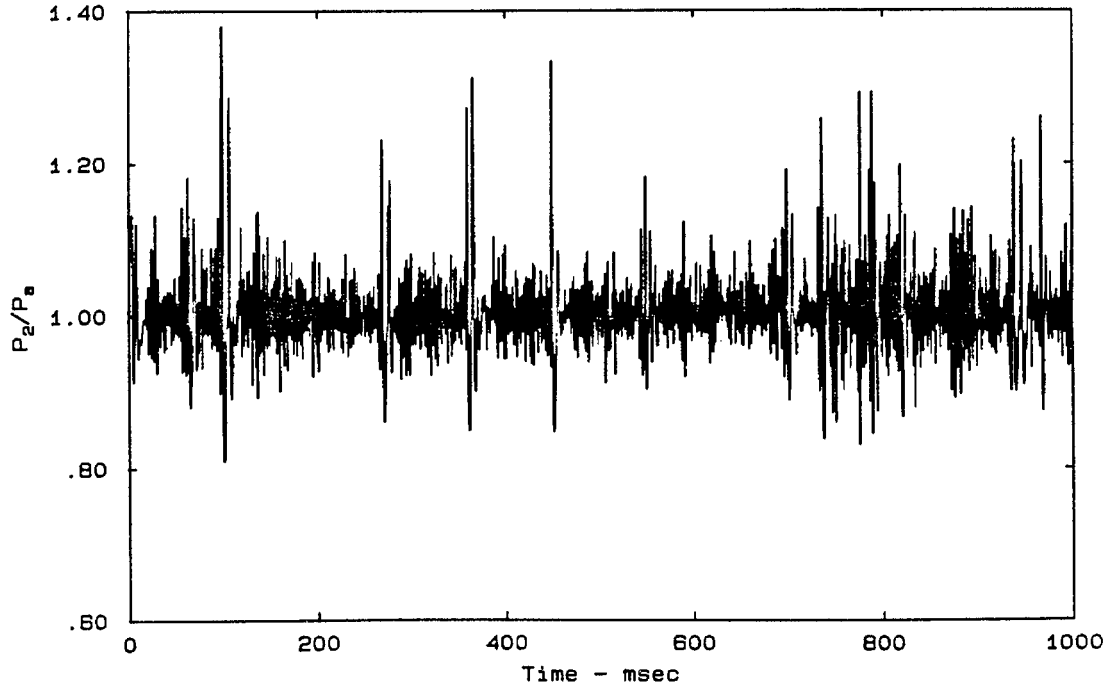

(b)

Figure 4.6 Comparison of pressure histories for nitrogen jets,
(a) M_e = 1.86,
(b) M_e = 1.00.

As the density ratio, ρ_a/ρ_j, increases, the frequency of chugging also increases. This is illustrated in Figure 4.7, where the pressure histories of $M_e = 1.0$ refrigerant-22 and nitrogen jets are compared. Large fluctuations in pressure occur nearly continuously for the nitrogen jet, while fewer fluctuations occur for the refrigerant-22 jet. Again, the peak overpressure associated with the more unsteady jet is larger.

4.3. Intermittency.

As mentioned previously, chugging rarely occurs as a single isolated event; usually it occurs as a series of intermittent events. The number of events and the strength are indications of the extent of jet unsteadiness. As already shown, both are strongly dependent on the flow conditions, in particular, on the liquid/gas density ratio, the operating pressure ratio, and the exit Mach number.

The intermittent nature of chugging can be used to quantify the conditions under which it occurs. In general, intermittency is defined as the fraction of the time a flow exhibits a certain behavior. For example, in studies of boundary layers and shear layers, intermittency is often used as a quantitative measure of the time the flow is turbulent or nonturbulent. In a similar manner, the concept of intermittency can be applied here to measure the fraction of the total time during which the jet is chugging. Specifically, the intermittency for the various jets can be computed and correlated with the flow parameters. This correlation gives an indication of the relative effect of each parameter on the jets tendency toward unsteadiness. In this section, we use measurements of intermittency to establish the operating conditions necessary for maintaining steady gas jets into liquids.

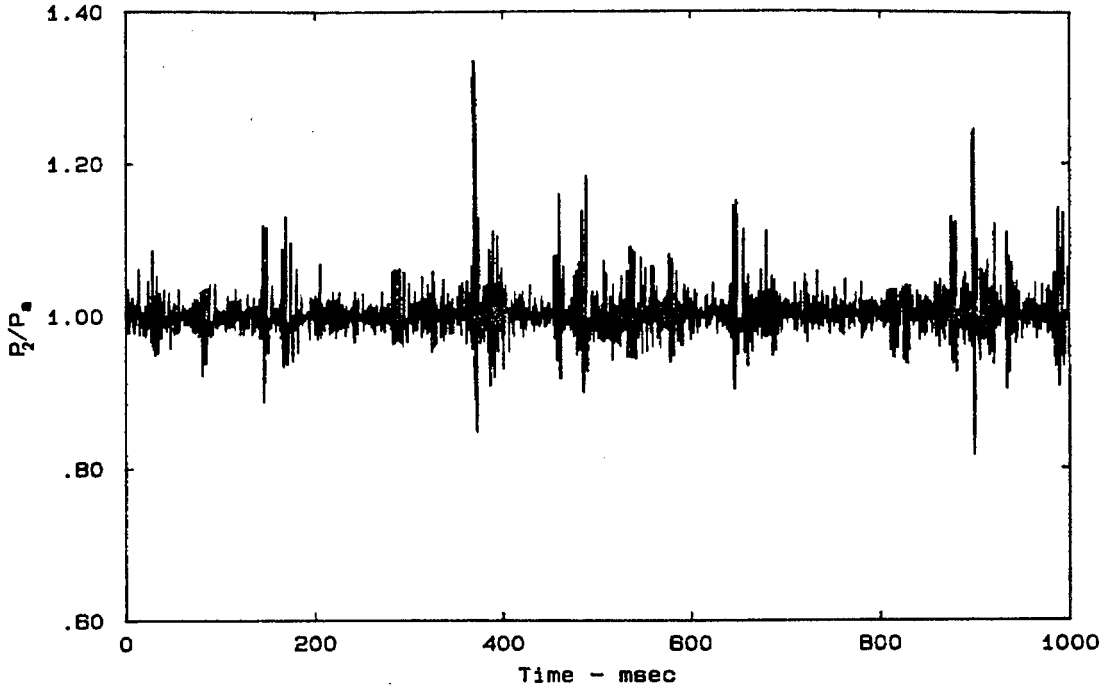

(a)

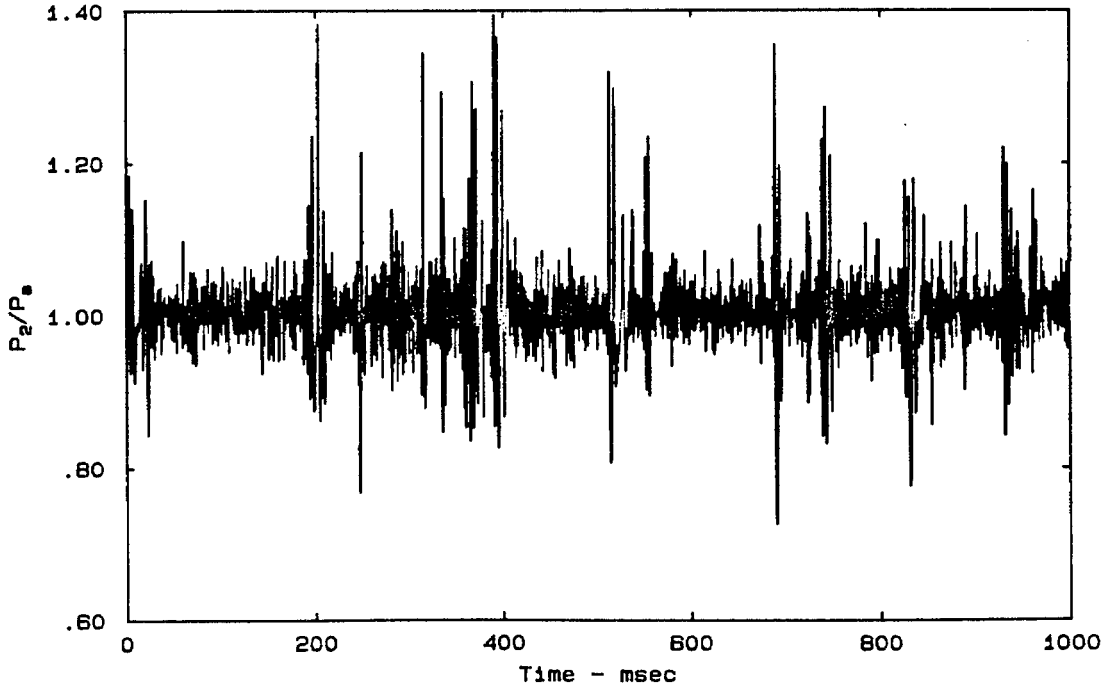

(b)

Figure 4.7 Comparison of pressure histories for sonic jets,
(a) R22,
(b) N2.

To determine intermittency, criteria are applied to the pressure signal to distinguish the portions of the signal that correspond to chugging and to steady flow. An intermittency function, defined as

$$I(t) = \begin{cases} 1 & \text{unsteady} \\ 0 & \text{steady} \end{cases} \tag{4.1}$$

is generated (Kovasznay et al., 1970). This function is a series of square pulses of varying widths that show the time distribution of steady and unsteady flow. The time-averaged value of I(t), known as the intermittency factor, Γ, or more commonly just intermittency, can then be computed from

$$\Gamma = \lim_{T\to\infty} \int_{t_o}^{t_o+T} I(t)dt = \frac{1}{T} \sum_{n=0}^{N} \Delta t_n \tag{4.2}$$

where T is the total run time, t_o is the starting time, Δt_n is the width of the nth pulse of I(t), and N is the total number of pulses. An intermittency of 1.0 signifies continuous chugging; Γ of zero signifies a steady jet.

To generate the intermittency function and thus compute intermittency, a set of criteria must be established to differentiate the steady and unsteady portions of the pressure signal. The following procedure was used to determine the intermittency of gas jets into liquid:

1. Given a pressure signal such as Figure 4.8(a), the absolute value of the pressure signal was taken. This was done to give equal weight to the positive and negative overpressures that occur as the gas column expands and deflates.

2. Next, the signal was smoothed five times by a five-point smoothing technique. This eliminated the pressure fluctuations associated with the high-frequency, small-scale motion of the jet boundary. A

Gaussian smoothing was also tried, but the resulting signal was not appreciably different from the signal filtered by the five-point method.

3. The threshold for chugging was set at 30 percent of the peak pressure fluctuation for that particular run. Above the threshold, chugging was assumed "on"; below the threshold, a steady jet was assumed. Note that the threshold level varies from one run to the next.

4. The initial rise in pressure at t = 0 was ignored. This change in pressure reflects the transient startup of the jet and is not an indication of chugging.

5. Finally, when many chugging events occurred close together, less than 0.5 msec apart, the multiple events were counted as a continuous event.

Figure 4.8(a-c) shows a typical measured pressure history, the smoothed signal, and the intermittency function.

Plotted in Figure 4.9 is the jet intermittency as a function of the dimensionless momentum parameter, J/J_e. The parameter, J/J_e, is defined as

$$\frac{J}{J_e} = 1 + \frac{P_e - P_a}{\rho_j U_e^2} = 1 + \frac{1 - \frac{P_a}{P_e}}{\gamma M_e^2}, \qquad (4.3)$$

and is simply the ratio of the jet momentum to the momentum that same jet would have if it were pressure-matched. This parameter is a measure of the under or overexpansion of the jet. A momentum factor greater than one indicates an underexpanded jet; less than one, an overexpanded jet. The above expression is particularly useful in characterizing the

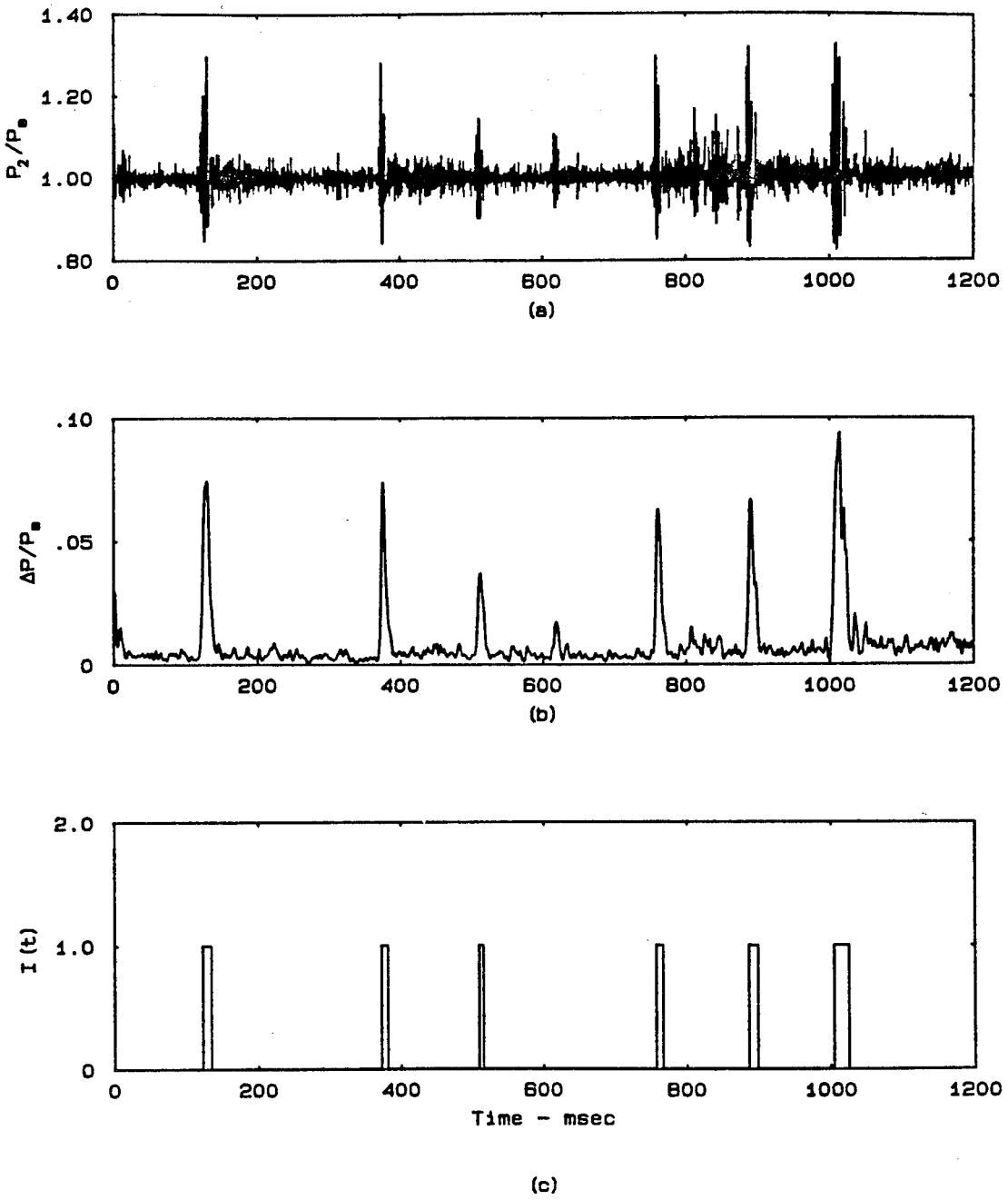

Figure 4.8 Intermittency,
(a) Pressure signal of R22 jet,
(b) Smoothed signal,
(c) Intermittency function.

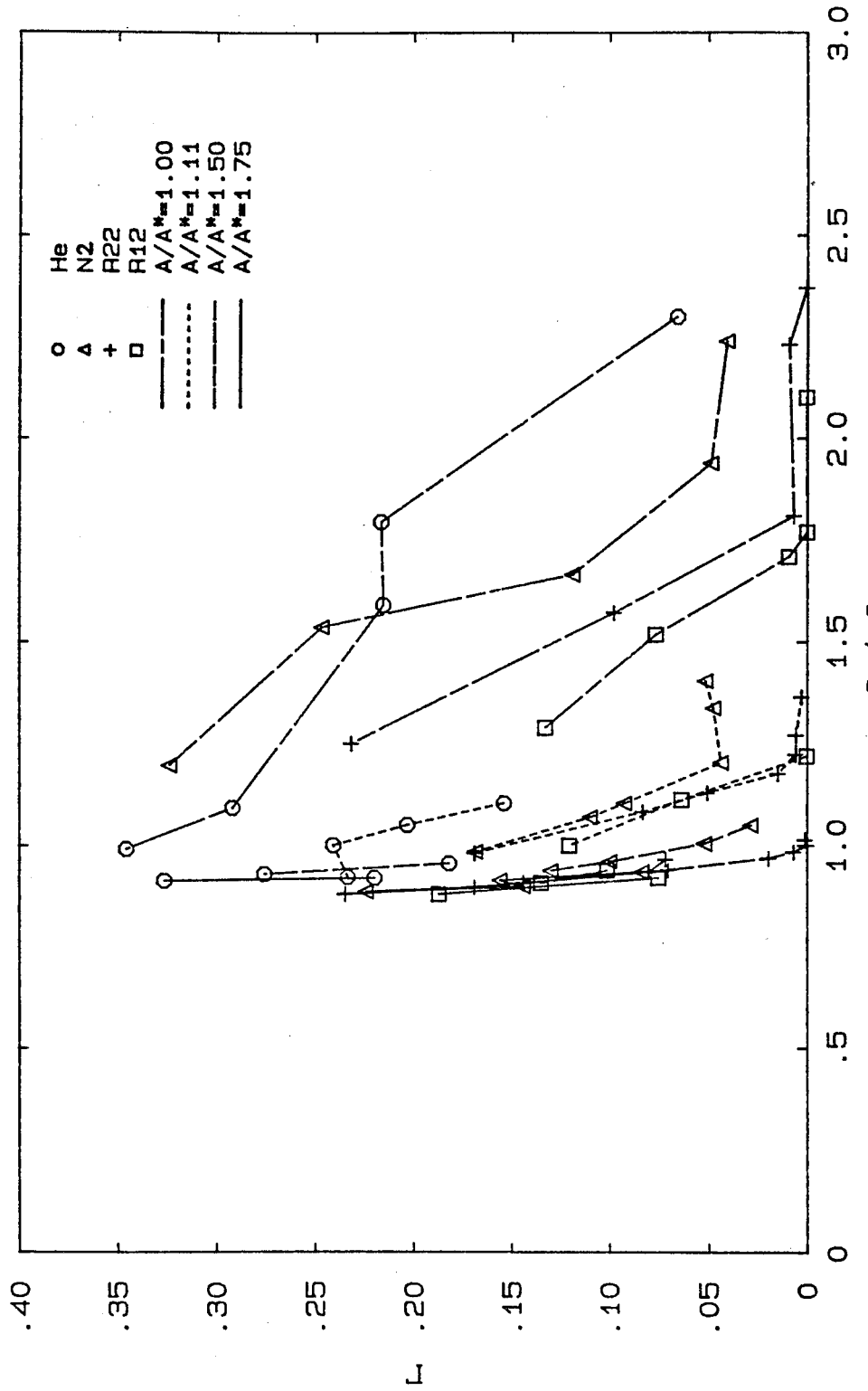

Figure 4.9 Distribution of Γ with J/J_e.

flow since the ratio includes all flow variables of significance to the problem, namely, the gas density, the jet velocity, and the exit pressure.

Figure 4.9 shows four sets of data, grouped by nozzle area ratio, A/A^*. Within each set, there are four curves, each corresponding to a different gas. Each point is the average of 8-10 different experiments, or about 14-20 seconds of jet run time. Three trends are indicated in Figure 4.9:

1. For a given J/J_e and A/A^*, the lighter jet is more unsteady. For example, from a convergent nozzle at $J/J_e = 1.0$, the helium jet is most intermittent, showing chugging approximately 35 percent of the time as compared to 30, 28, and 24 percent of the time for nitrogen, refrigerant-22, and refrigerant-12 jets, respectively. Similarly, from a nozzle of $A/A^* = 1.11$ at $J/J_e = 1.0$, the helium jet again is the most unsteady, showing Γ of 0.25 as compared to 0.17, 0.15, and 0.12 for the other jets.

2. The intermittency depends on the nozzle area ratio (i.e., the exit Mach number); the jet is less intermittent at larger nozzle area ratio. This trend is clearly evident in the displacement of the four sets of curves in Figure 4.9. For example, at $J/J_e = 1.0$, a nitrogen jet issuing from a nozzle of $A/A^* = 1.0$ would be intermittent about 28 percent of the time. The same jet from an $A/A^* = 1.11$ nozzle would be intermittent only 15 percent of the time.

3. A gas jet into liquid is sensitive to the operating pressure ratio. Even slight underpressure can cause the jet to be unsteady. An underpressure of just 10 percent increases intermittency from zero to well over 10 percent in an R12 jet from a deLaval nozzle with $A/A^* = 1.75$. On the other hand, overpressurizing is stabilizing. For example, from a convergent nozzle, a helium jet that

shows chugging at the pressure-matched condition is stabilized when it is overpressurized to $J/J_e \simeq 1.2$. The intermittency decreases from 0.35 to nearly zero.

These three trends imply that there are certain conditions under which gas jets into liquid are steady. Specifically, one can obtain steady jets in two ways: (1) by increasing the exit Mach number through the use of deLaval nozzles, or (2) by strongly overpressurizing the jet (i.e., operate the jet at large J/J_e). Figure 4.9 shows the overpressurization necessary. If an intermittency of 0.05 is taken as the criterion for a steady jet, then the various jets become stable at the operating conditions shown in Table 4.1.

Table 4.1. Necessary Operating Conditions, J/J_e, for Steady Jets

Gas		Nozzle Area Ratio, A/A^*			
		1.00	1.11	1.50	1.75
R12	J/J_e	1.60	1.12	1.00	1.00
	M_e	-	-	1.75	1.90
R22	J/J_e	1.66	1.12	1.00	1.00
	M_e	-	-	1.77	1.92
N2	J/J_e	1.92	1.18	1.00	1.00
	M_e	-	-	1.86	2.04
He	J/J_e	2.32	1.22	1.08	1.00
	M_e	-	-	-	2.20

As indicated in the table, the operating condition, J/J_e, must be greater than 1.6 for no chugging to occur for an R12 jet discharging

from a convergent nozzle. Operation at the pressure-matched condition is sufficient for an N2 jet from a deLaval nozzle of $A/A^* = 1.50$ to be steady.

The relationships among the significant flow variables - liquid/gas density ratio, operating pressure ratio, and exit Mach number - are nonlinear, and presently, it is not clear which universal scaling parameter might collapse the intermittency distributions shown in Figure 4.9 to a single curve. Until such a parameter is determined, Table 4.1 provides practical estimates of jet susceptibility to instability.

4.4. Model and Mechanism for Jet Column Collapse.

In this section, a model and a possible mechanism for jet column collapse are presented. It will be shown that the jet collapse resembles the collapse of a bubble in liquid and that a pressure difference between the jet and ambient fluid is the mechanism causing chugging.

4.4.1. Model. In an effort to characterize chugging, the collapse of a bubble in liquid is used to model the collapse of the jet column. This model is suggested by the similarity between the behaviors of the two systems; that is, chugging (oscillations and collapse of the gas column) resembles the oscillations and collapse of a bubble in liquid. The fact that chugging is localized to the jet initial region, and thus, it is sufficient to consider only the first several diameters, suggests that there is also a physical resemblance between the jet and bubble.

Just as a pressure difference between the gas and liquid drives bubble collapse, a pressure difference between the jet and surrounding liquid is speculated to be the cause of jet collapse. The magnitude and the process by which the pressure difference is generated will be discussed in the next section. To verify that the proposed model is

reasonable, comparisons of the jet collapse time measured from experiment can be made with the time required for the collapse of a bubble of the same diameter as the jet and with the same pressure difference.

Figure 4.10 shows the model of the jet. The spherical bubble has radius R_b and pressure P_b. The bubble is assumed submerged in liquid and is located near the nozzle exit. The time required for bubble collapse can be approximated by

$$t_b \simeq 0.910 \left[\frac{\rho_l R_b^2}{\Delta P}\right]^{1/2} \tag{4.4}$$

where ρ_l is the density of the liquid and ΔP is the pressure difference between the liquid and the vapor,

$$\Delta P = P_a - P_b.$$

Surface tension and viscosity are neglected. Equation (4.4) was derived by Rayleigh (1917) (see review of bubble dynamics by Plesset & Prosperetti, 1977) for bubble collapse driven by an impulsive rise in the liquid pressure. In the present case, bubble collapse is assumed to arise from a deficit in the bubble internal pressure; the liquid pressure remains constant.

To compute the bubble collapse time, it is necessary to know both the bubble radius and pressure. The bubble radius is equivalent to the jet half-width just prior to final collapse. For example, for the jet depicted in Figure 4.1, the bubble radius is about 2.5D (see frame 6c). The bubble pressure is the pressure inside the jet. This pressure was not directly measured in the experiment. However, pressure measurements were obtained of the jet overpressure at a distance of 1.6 cm from the jet centerline. Figure 4.10 shows schematically the location of the pressure measurement relative to the nozzle and bubble. Since it is

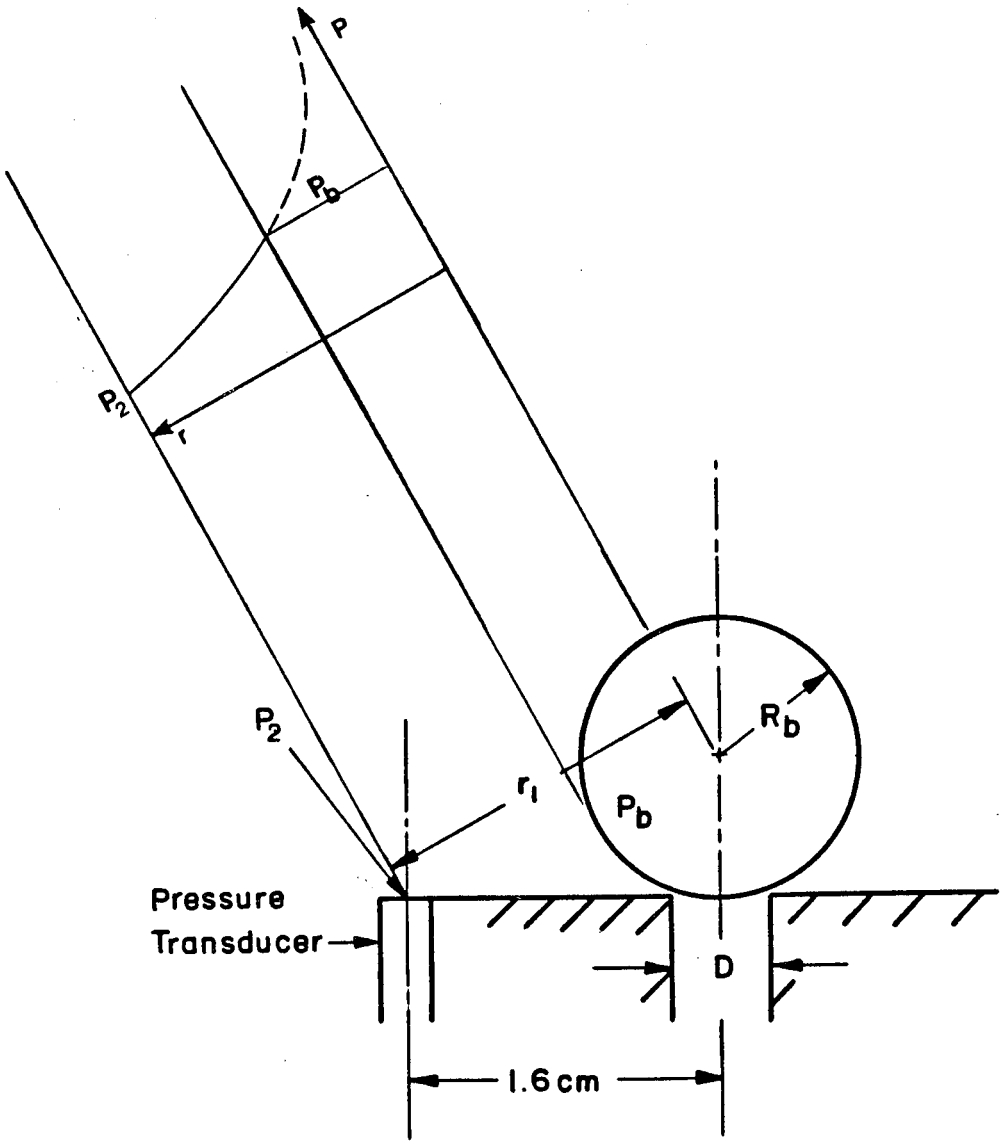

Figure 4.10 Model for jet column collapse.

well known that pressure varies inversely with distance from the source, the bubble pressure can be estimated by applying a 1/r correction to the known overpressure. Thus,

$$P_b = P_2\left[\frac{r_1}{R_b}\right] \tag{4.5}$$

where r_1 is the radial distance from the center of the bubble to the transducer and P_2 is the measured overpressure. In these experiments, P_b is typically between 0.8-0.9 atmospheres.

Plotted in Figure 4.11 is the ratio, t_b/t_j, as a function of a nondimensional momentum, J/J_e. t_j is the time for jet collapse (typically, 1-2 milliseconds), measured directly from films, that is, the time from when the jet has it widest diameter to complete pinchoff. As shown in Figure 4.11, the correlation of t_b/t_j is close to one for the nearly the entire range of J/J_e. There is, however, more scatter in the data for J/J_e less than one. The discrepancies at the lower values of J/J_e occur because in some cases, the gas column does not collapse completely; that is, the column continues to have a finite diameter after reaching its minimum. The bubble collapse time, however, was computed, assuming collapse to zero diameter. Therefore, the estimated time would overpredict the measured collapse time.

The fact that t_b/t_j is nearly one indicates that the jet and bubble collapse times are comparable. Thus, the bubble model is a reasonable one for the jet. Note that the type of gas does not enter into Equation (4.4) and was not considered in this comparison of characteristic times. Nevertheless, the collapse times correlate closely. Since gas density is negligible compared to liquid density, the effect of gas density on bubble motion is minimal. The liquid inertia and the pressure difference between the bubble interior and the surrounding liquid are the dominant parameters contributing to jet collapse.

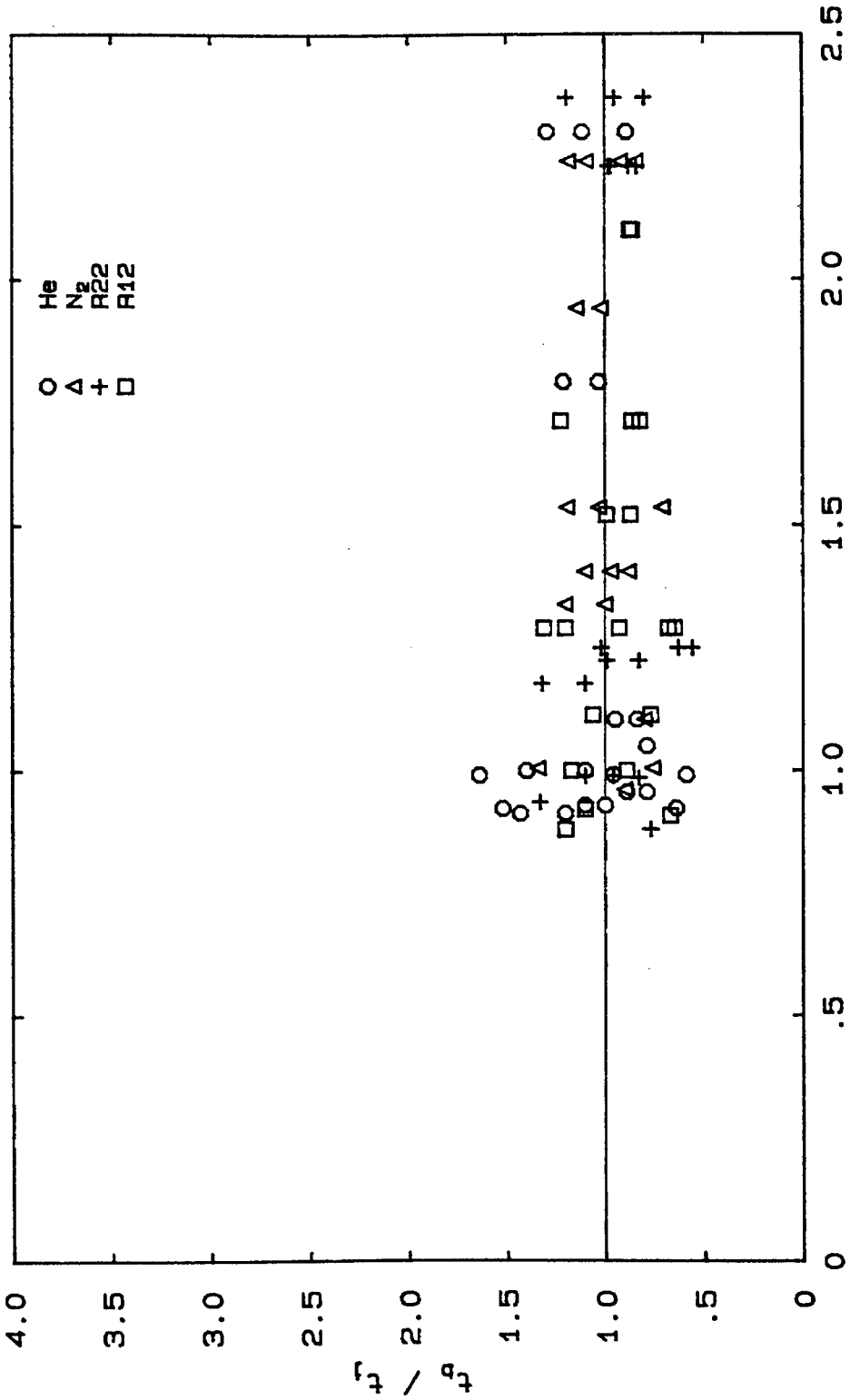

Figure 4.11 Correlation of collapse times.

4.4.2. Mechanism. We speculate that chugging, which, as shown above, resembles bubble oscillation and collapse, is the response of the jet boundary to a pressure difference between the jet and ambient fluid generated by the rapid expansion of a light fluid into a heavier one. As suggested in Section 4.2, in the early stages of a chugging event, the jet flow is analogous to the discharge of gas from a nozzle into a channel of larger cross section. This idealization is possible because when the ambient fluid is much denser than the jet fluid ($\rho_a/\rho_j>>1$), the jet flow time (typically tens of microseconds), is much less than the response time of the ambient liquid, and the gas/liquid interface acts as a nearly rigid channel. Figure 4.12(a) shows the typical structure of the jet just prior to jet column collapse. The jet is approximated as a duct of constant area in the streamwise direction but with a boundary that is slowly varying in time (Figure 4.12(b)). In this idealized configuration, the channel wall is equivalent to the gas/liquid interface; the shear layer is the jet boundary.

In such channel flows, the local pressure, P_w, in the base region immediately downstream of the area change, is significantly lower, due to gas entrainment at the jet boundary, than the pressure, P_e, just upstream of the area change. In response to the fact that P_w can be lower than the pressure in the surrounding liquid, the cylindrical interface moves radially inward on the second, slower time scale (the first, fast time scale is the gas flow time mentioned above). The cylindrical channel collapses violently and rebounds. Oscillations follow and increase in amplitude, apparently due to some feedback or resonance phenomenon. The time scale for this motion is on the order of the period for bubble collapse (typically milliseconds) as described in Section 4.4.1. The amplification of the oscillations eventually leads to the breakdown of the channel structure, often resulting in total collapse of the jet. After two or three oscillations, the jet reinitiates.

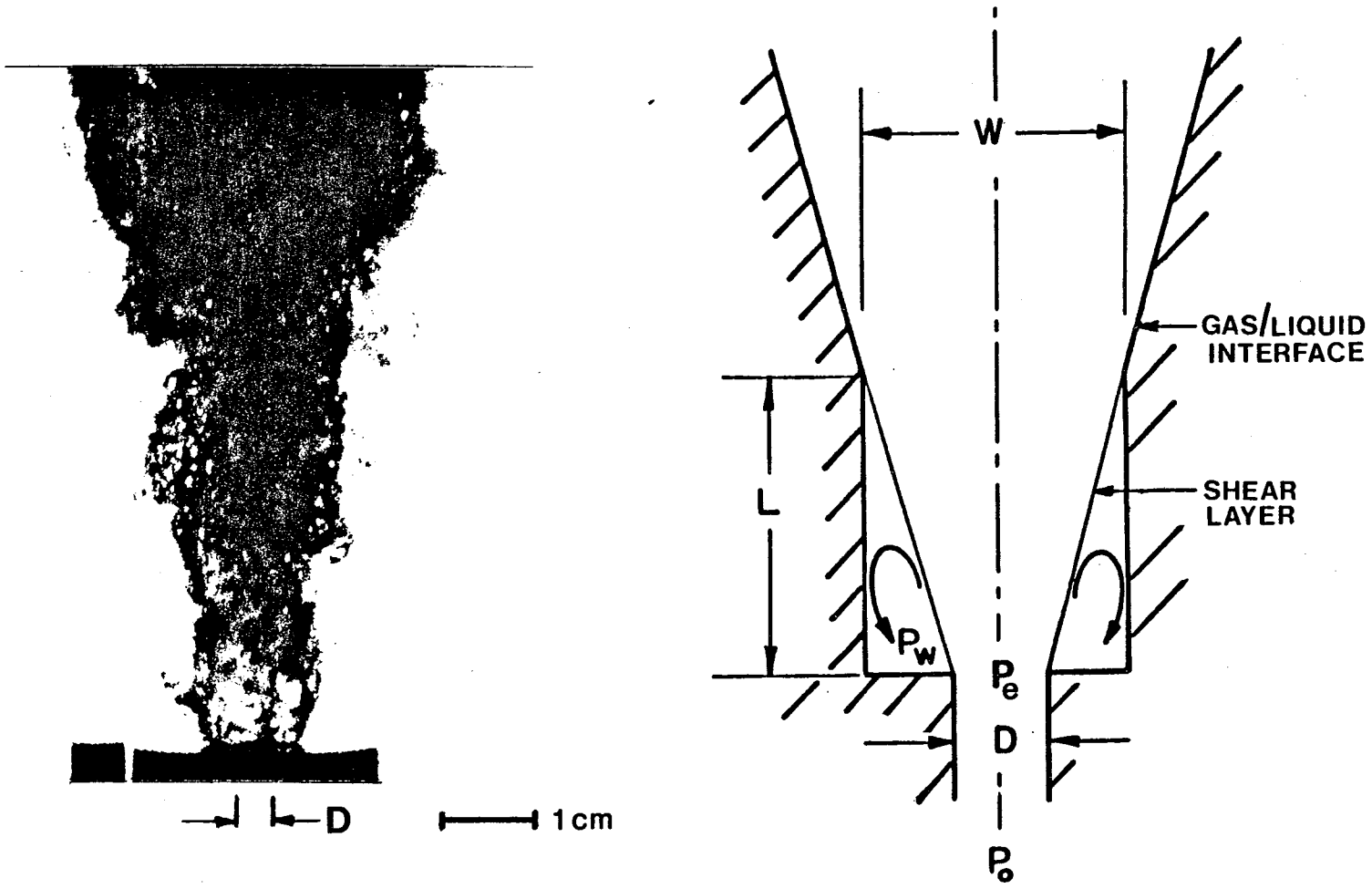

Figure 4.12 Jet flow configuration,
(a) Jet structure prior to collapse, D = 0.42 cm.
(b) Idealized configuration of jet flow.

It should be emphasized that the existence of the large density contrast between the jet and ambient fluid is crucial for the initiation of chugging. For jets where $\rho_a/\rho_j \simeq 1$, there is only one time scale associated with both expansion of the jet and response of the jet boundary to pressure fluctuations. Both occur on the short time scale which is on the order of the gas flow time, and therefore, no large-scale motion of the boundary reminiscent of chugging occurs. On this short time scale, the motion is the familiar high-frequency small-scale fluctuations observed in shear flows.

The proposed mechanism stimulates two important questions: (1) If it is assumed that the pressure difference between the jet and liquid is the result of flow given by Figure 4.12(b), how large a difference can be expected? How does it compare with experiment? (2) Given the pressure difference, how does the estimated time for the inward motion of the duct wall compare with the measured jet collapse time? The idealized configuration in Figure 4.12(b) has not been studied experimentally, even for fixed walls. However, studies of short length ducts of constant cross section, such as those by Jungowski (1969, 1978) and Witczak (1977), indicate that in some cases, P_w may be more than an order of magnitude less than P_e.

Shown in Figure 4.13 are some results for sonic discharge of air from a convergent nozzle into a duct with a larger cross section (Witczak, 1977). The schematic of the configuration Witczak investigated is given in Figure 4.13(a). ϕ is the ratio of the duct cross-sectional area to the nozzle area and P_o is the reservoir pressure. The normalized wall pressure, $\bar{P}_w = P_w/P_o$, is shown as a function of a normalized operating pressure, $\bar{P}_o$, where $\bar{P}_o$ is the ratio of the reservoir pressure to the reservoir pressure at the pressure-matched condition or $\bar{P}_o = 1/[1-(\rho U_e^2/P_o)(P_o/P_e)(J/J_e-1)]$ (where P_o/P_e is the design operating pressure). The pressure variation is shown for two geometries: $\phi = 0.222$ and 0.444. In the present work, a representative value of ϕ is 0.05. As indicated, for a fixed area ratio, the

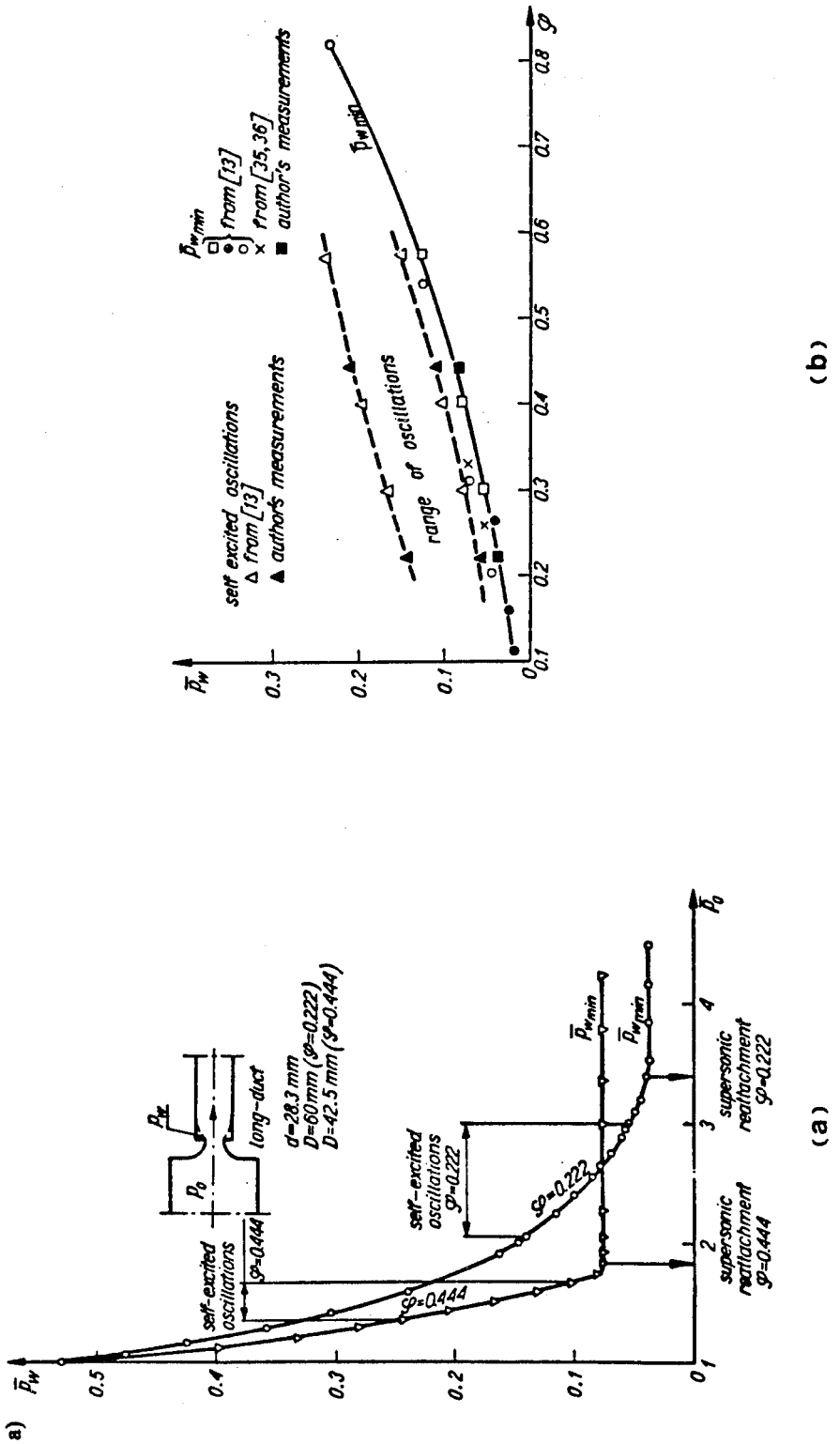

Figure 4.13 Variation of base pressure in duct flow (Witczak, 1977),
(a) Variation of $\bar{P}_w$ with $\bar{P}_o$,
(b) Variation of $\bar{P}_w$ with ϕ.

normalized wall pressure first decreases as the reservoir pressure increases and then remains constant. For example, for ϕ = 0.222 at the pressure-matched condition ($\bar{P}_o$ = 1), $\bar{P}_w$ is equal to the pressure at the nozzle exit, P_e/P_o = 0.528. As $\bar{P}_o$ increases to 3.4 and above, $\bar{P}_w$ decreases to 0.04, more than an order of magnitude less than the exit pressure ratio. For a duct of different area ratio, the same trend occurs: $\bar{P}_w$ again decreases with increasing $\bar{P}_o$ but to a different minimum value. The variation of the minimum base pressure, $(\bar{P}_w)_{min}$, with area ratio is shown in Figure 4.13(b).

Using the minimum wall pressures, it is possible to establish the upper limit of the pressure difference between the jet and the ambient fluid for a given area ratio. Listed in Table 4.2 (column 5) are the derived upper limits for the normalized pressure difference, $[P_a-(P_w)_{min}]/P_a$, for some sonic nitrogen (air) jets. Columns 2-4 show the jet operating pressure ratio; the area ratio, where the area ratio is taken to be the ratio of the measured jet cross-sectional area just prior to collapse to the nozzle exit area, and the measured pressure difference between the jet and liquid in the present experiments. Note that nearly all ϕ's from experiment are less than 0.1, below the range of area ratios where data for $(P_w)_{min}$ are available. However, by extrapolating the curve in Figure 4.13(b) to small ϕ, it is possible to estimate $(\bar{P}_w)_{min}$. Whether such extrapolation is a reasonable approximation and, indeed, whether there are better estimates for the actual base pressures at the conditions of the present work, remain to be determined by future experiments with a variety of gases in rigid channels.

As shown in Table 4.2, the derived pressure difference provides a comfortable limit on the pressure difference between the jet and liquid. The derived values indicate that differences above 90 percent are possible; however, the measured values indicate that differences of 10-45 percent are more likely. In any case, the upper bound indicates that significant pressure differences may exist. The experiments show

Table 4.2. Comparison of P_b and P_w and Jet Collapse Times

1	2	3	4	5	6	7	8
Gas	$\frac{P_o}{P_a}$	ϕ	$\frac{P_a-P_b}{P_a}$	$\frac{P_a-(P_w)_{min}}{P_a}$	t_j (msec)	t_b (msec)	t_w (msec)
N2	5.08	0.064	0.255	0.909	1.00	1.18	0.625
		0.044	0.228	0.960	1.75	1.46	0.935
		0.046	0.176	0.959	1.50	1.63	0.915
		0.069	0.285	0.930	1.13	1.04	0.709
	4.40	0.027	0.154	0.987	2.00	2.27	1.081
		0.032	0.210	0.976	1.75	1.79	0.789
	3.24	0.079	0.160	0.952	1.25	1.29	0.508
		0.022	0.310	0.987	2.50	1.77	0.947
		0.038	0.176	0.978	1.50	1.79	0.723
R22	5.08	0.069	0.140		1.49	1.42	
		0.250	0.240		0.75	0.60	
		0.094	0.162		1.25	1.19	
	4.40	0.131	0.166		1.13	1.00	
		0.250	0.118		0.88	0.85	
		0.038	0.278		2.25	1.43	
		0.122	0.174		1.03	1.00	
	2.36	0.069	0.132		1.50	1.53	
		0.078	0.225		1.75	1.11	
		0.062	0.179		2.50	1.39	
R12	4.06	0.107	0.174		1.25	1.07	
		0.059	0.156		1.75	1.53	
	3.24	0.117	0.124		1.00	1.25	
		0.077	0.119		1.50	1.53	
		0.028	0.259		2.00	1.72	
	2.36	0.038	0.250		2.30	1.50	
		0.059	0.137		1.75	1.63	
		0.093	0.163		1.75	1.19	
He	6.44	0.054	0.237		1.00	1.29	
		0.022	0.250		1.75	1.95	
		0.024	0.366		2.50	1.57	
	2.02	0.042	0.098		2.50	2.40	
		0.026	0.099		1.75	2.88	
		0.034	0.132		3.76	2.17	

that even a 30 percent difference can cause catastrophic jet collapse.

Table 4.2 also provides a comparison of jet column collapse times, including the collapse times measured from films, t_j; the estimated times, t_b, based on measured pressure and visually observed diameter (Equation 4.4); and the derived time t_w, based on $(\bar{P}_w)_{min}$ and visually observed diameter (again using Equation 4.4). Each value of t_w can be interpreted as a lower limit for the time required for the gas/liquid interface to move radially inward and collapse onto the axis. In all cases, t_w is below the experimental value, in fact, approximately half.

Finally, the operating conditions and the measured pressure difference and collapse times for sonic R22, R12, and He jets are also shown in Table 4.2. Base pressure data for these gases are not available. The experimental values are comparable to those for the nitrogen jet.

Chapter 5
CONCLUSION

An experimental investigation of the development of impulsively initiated high velocity gas jets into liquid was conducted in an effort to understand some of the physical processes that occur for a jet of very light fluid into a dense ambient atmosphere. Four gases, refrigerants 12 and 22, nitrogen, and helium were injected into water at exit Mach numbers ranging from 1.0 to 2.2, allowed to develop and reach steady state. Results show that there are at least three stages in the development of a gas jet in water: startup, transition, and global steady state. However, the most significant finding was that under some conditions, a gas jet into liquid never reaches steady state; instead, chugging occurs. In this study, the chugging process was documented and the conditions under which chugging occurs were quantitatively examined. Finally, a mechanism for the chugging was proposed. A summary of the main experimental results is given in the following, starting with a description of the different stages of jet development.

Startup is the first of three stages of jet development. This stage is characterized initially by bubble blowing, where the inertia of the liquid dominates and the directed momentum is small, so the motion of the gas/liquid interface is radially outward. The growth rate is reasonably well predicted by classical bubble growth theory. The bubble surface is subject to large radial accelerations, so distortions develop as a consequence of the Rayleigh-Taylor instability. These distortions first appear as longitudinal streaks and circumferential waves (typical length scales of 0.1-0.5D) and later develop into random perturbations. The general features of the startup phase remain unchanged even when the initial gas/liquid interface and flow Mach number are altered.

One interesting consequence of shock-initiated flow is the development of a secondary jet on the axis of the startup bubble. Its origin can be deduced from a geometric acoustics argument and the time of initiation can be estimated by ray tracing. The structure and growth of the secondary jet are reminiscent of the primary jet. For example, surface distortions similar to those found on the primary jet are observed on the secondary jet. The relative scales are also comparable.

The second stage of jet development is the transition phase. Transition is marked by the termination of radially outward bubble growth. The flow, which becomes axially directed, penetrates the stationary bubble and forms a cylindrical protrusion along the axis of symmetry. The gas/liquid interface is roughened by azimuthal structures that form on the tip of the growing jet and that propagate upstream, indicating strong recirculating gas flow between the jet and surrounding liquid. Small scale distortions can be seen superimposed on the azimuthal structures. The length scales of the large structures are on the order of 2D; the scales of the small distortions are ~0.1D. Entrainment by the jet deflates the bubble near the base. As the the gas/liquid interface closes in on the axis, the remnant of the bubble-growth phase lifts off and is swept downstream.

The third stage of jet development is steady state. The gas flow from the nozzle is steady, although the jet itself is not always steady. An instability of the jet boundary may cause chugging: large nonlinear oscillations of the jet that lead to the collapse of the gas column, pinchoff of flow, and jet reinitiation. The unsteadiness is much more violent than the familiar fluctuations typical of constant-density jets. The length scale of the unsteady motion is generally on the order of several jet diameters; the time scale is on the order of the period for the collapse of a bubble of diameter about 5D, driven by a pressure difference of order 30 percent of the ambient pressure.

In addition to chugging, there are local small-scale fluctuations of the jet boundary. On the short time scale, small bubbles are torn from the interface and shed into the liquid, and fine liquid droplets are entrained into the jet column. Instantaneous photographs show that in the first few jet diameters, there is a distinct interface separating the gas and liquid. However, farther downstream (beyond 5D), the jet appears as a mixture of gas bubbles and liquid droplets of varying sizes. Measurements of the droplet velocity along the jet centerline were made. Correlation with the scaled downstream distance, x/D^*, showed good agreement with data for conventional jets. In addition, time exposure photographs showed that the conical spreading angle of the jet was 18-25 degrees, also in agreement with conventional jets.

The character of the unsteady behavior (chugging) was described in detail. The collapse of a bubble in liquid was used to model the jet column collapse. The pressure fluctuations associated with the oscillations and gas column collapse were found to be typically 20% but in some case, were as large as 70% of the ambient pressure. The amplitude and frequency of the oscillations are strongly dependent on the gas density as well as on the flow conditions such as the exit Mach number and operating pressure.

The intermittent nature of the unsteadiness was exploited in an effort to assess the relative importance of the density ratio, ρ_a/ρ_j, the momentum parameter, J/J_e, and the nozzle area ratio, A/A^*, and to establish criteria for maintaining steady jets. Three trends were found:

1. For a given J/J_e and A/A^*, the jet with the higher density ratio showed stronger and more frequent chugging. Of all jets tested, helium was the most unsteady.

2. All other parameters constant, the jet operated at large J/J_e was more likely to be steady and to show less chugging.

3. Similarly, the jet issuing from a nozzle of larger A/A^*, was more likely to be steady.

It was found that steady jets can be achieved in two ways: by being discharged from deLaval nozzles (increasing exit Mach number) or by being strongly overpressurized (increasing J/J_e).

A mechanism for chugging was discussed. It was proposed that chugging is the response of the jet bound- ary to a pressure difference between the jet and ambient fluid. The pressure difference arises from the rapid expansion of the jet fluid in a base flow at the exit. The unsteady behavior involves two separate processes on two time scales. The first is the process by which the pressure difference arises; this occurs on the short time scale (typically tens of microseconds). The second process is the motion of the jet in response to the pressure difference; this occurs on the long time scale (typically milliseconds).

The large density contrast between the jet and ambient liquid plays a crucial role. On the short time scale, the motion of the liquid is slow and the gas/liquid interface acts as a nearly rigid channel due to the density contrast. Indeed, the observed shape of the jet suggests that the flow is similar to the discharge of gas from a nozzle into a channel of larger cross section. In such flows, the base pressure downstream of the area change is lower than the pressure upstream of the area change. This is due to gas entrainment. The base pressure may also be lower than the pressure in the surrounding liquid. Therefore, a pressure difference arises. The response of the jet boundary to this pressure difference occurs on the second, long time scale. An upper limit for the pressure difference was determined based on estimates of the minimum base pressure from channel flow.

Similarly, a lower limit for the time for jet column collapse was determined. All experimental values for the pressure difference and jet collapse time are within the limits.

The present study shows that the development of a high velocity gas jet into liquid is quite different from the development of a single-phase jet. The large density contrast of thé two-phase jet yields the unexpected property of chugging. Since chugging is not observed in jets with little density contrast, it would be useful to determine the lowest density ratio necessary for the unsteady behavior to occur. Presumably, the limiting density ratio is between 195 (the lowest ratio studied here) and about 30 (the largest ratios in studies of conventional jets). Quantitative analysis of the startup and transitional stage of jet development would also add greatly to the understanding of gas jets into liquids.

Appendix

STABILITY THEORY AND APPLICATION TO THIS EXPERIMENT

The stability of plane and axisymmetric interfaces between fluids of different density has been examined by many investigators, some of whom are mentioned in Chapter 1. However, few researchers have considered jets with large density contrast (such as gas jets into liquid) and none has predicted chugging. For high velocity gas jets into liquid as in the present work, both the compressibility of the gas and the large density contrast can significantly affect the behavior. In an effort to understand the influences of these parameters, the instability of a compressible axisymmetric jet is investigated by means of linear stability theory. The intent is to compare the spatial scale of chugging observed in gas jets into liquid, with the wavelengths of the most amplified disturbance predicted by theory. No attempt is made to develop a new stability theory; rather, the temporal analysis by Lessen et al. (1965) for the inviscid compressible axisymmetric jet is modified for application at the conditions tested in this study.

Mattingly & Chang (1974) and Watson (1962) have indicated that predictions of spatial stability theory are more appropriate than those of temporal theory for comparison with experiment since spatially growing disturbances conform more closely to what are observed experimentally. For that reason, the temporal analysis by Lessen et al. was modified and rederived for the spatial case. The temporal case was also examined; however, those results will only be briefly discussed.

The development of the theory is done in the usual manner, first by linearizing the equations of motion and then, by applying the boundary conditions. The main assumptions are that the perturbations in pressure, temperature, density, and the three components of velocity are small; the jet and surrounding fluids are perfect gases; and the

pressure is continuous across the boundary between the two fluids. Note that the perfect gas assumption is obviously not a good one for a gas/liquid system. However, since the equation of state for a liquid can be quite complex and not easily incorporated into the equations of motion and, since our interest is merely to understand the qualitative effects of the Mach number and density ratio on the jet stability, the perfect gas approximation is adequate.

A.1. Spatial Stability.

For a jet with parallel uniform velocity, U, into ambient fluid at rest, the spatial analysis yields a nondimensional eigenvalue equation

$$\left[1-\frac{\chi}{\gamma}\right]^2 = \beta\left[\frac{K_n(\chi\xi_a)I_n'(\chi\xi_j)}{K_n'(\chi\xi_a)I_n(\chi\xi_j)}\right] \qquad \text{(A.1a)}$$

where

$$\chi = \alpha R,$$

$$\gamma = \frac{\omega R}{U};$$

R is the nozzle radius, β is the density ratio (ρ_a/ρ_j), and ω is the frequency. The wavenumber, α, is complex,

$$\alpha = \alpha_r + i\alpha_i,$$

where the real part, α_r, is the wavenumber, and the imaginary part, α_i, is the amplification rate. The variables $I_n()$ and $K_n()$ are the modified Bessel functions of the first and second kinds and n refers to the mode. The prime symbol denotes differentiation with respect to the variable R. The effects of jet Mach number, M, and sound speed, a, are contained in the two terms,

$$\xi_j = \left[1-M^2\left(1-\frac{Y}{\chi}\right)^2\right]^{1/2} \qquad \text{(A.1b)}$$

and

$$\xi_a = \left[1-M^2\left(\frac{a_j}{a_a}\right)^2\left(\frac{Y}{\chi}\right)^2\right]^{1/2} \qquad \text{(A.1c)}$$

where the subscripts a and j refer to the ambient and jet fluids, respectively. The normalized frequency, Y, is shown in Equation (A.1a) as an implicit function of χ. The equation can be solved numerically for Y for a given χ by a variety of methods. Here, Newton's method was used to solve for the axisymmetric mode (n=0) of disturbance.

Figure A.1 shows a normalized amplification rate, $-\alpha_i U/\omega$, as a function of the nondimensional frequency, Y, for nitrogen and refrigerant-12 jets at different Mach numbers. The choice of axes is consistent with those used by other authors (see Michalke, 1984). The figure shows the influence of both the exit Mach number and the liquid/gas density ratio on the jet stability. The effect of increasing Mach number is stablizing, for both the range of unstable frequencies and the growth rate are reduced. For example, an M = 1.3 nitrogen jet is unstable to disturbances of frequencies Y = 0 to 0.078, while an M = 2.0 jet is unstable only to those frequencies Y = 0 to 0.02. The maximum amplification rate decreases from 5.5 to 2.5. Also, note that the maximum growth rate is displaced to a lower frequency as the Mach number increases. This result is consistent with those found by Michalke (1970) for constant-density jets.

Increasing the density ratio has the same effect as increasing the Mach number. The range of unstable frequencies is reduced and shifted to lower values. For example, the predicted frequency of the most amplified disturbance for a M = 2 refrigerant-12 jet is 0.032, while

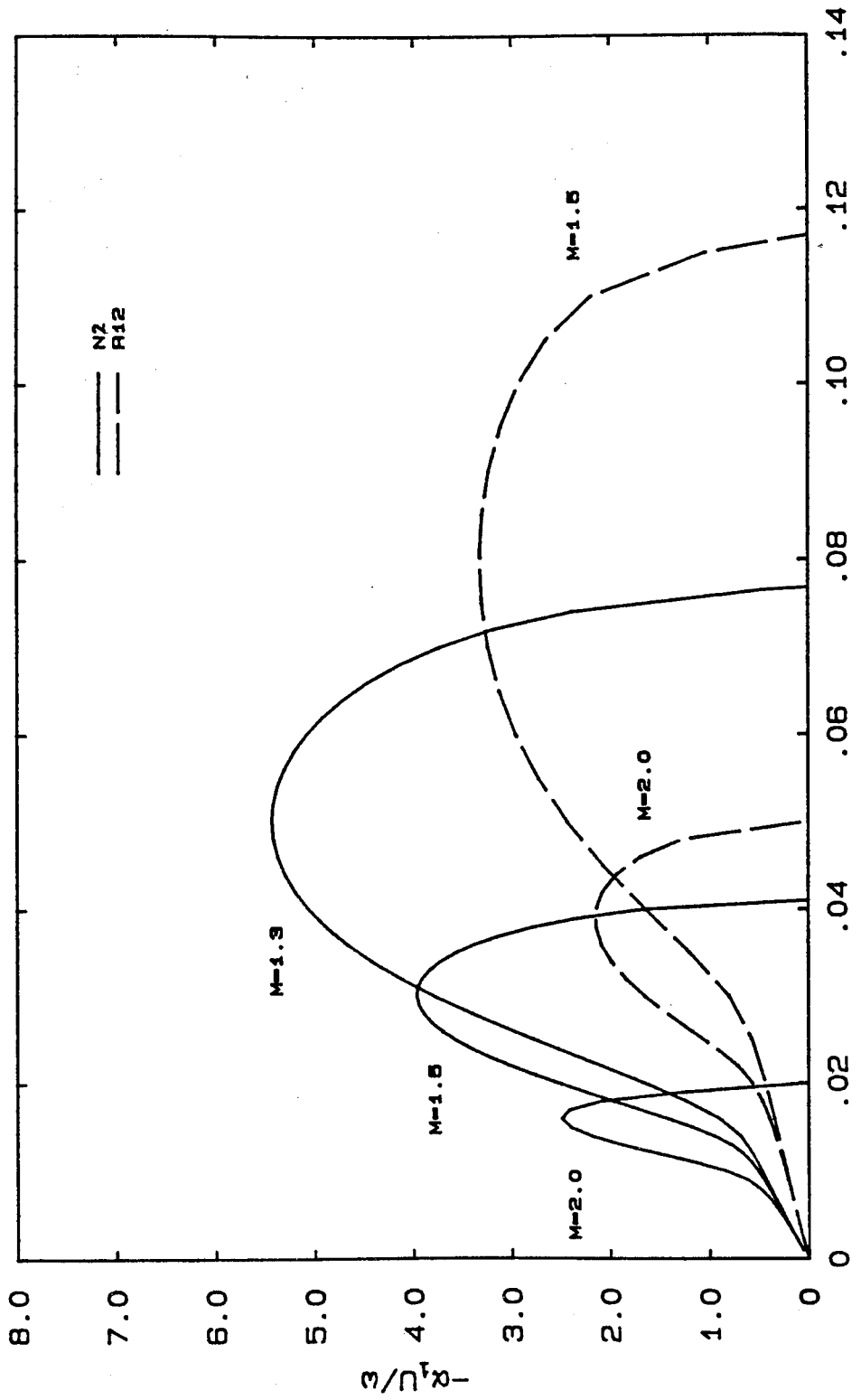

Figure A.1 Spatial amplification ratio of axisymmetric (n=0) disturbances versus frequency.

the most amplified frequency for the nitrogen jet is 0.018, only about half that for the refrigerant-12 jet. However, unlike the effect of increasing the Mach number, increasing the density ratio does not appreciably change the maximum growth rate. For example, the growth rates for M = 2 refrigerant-12 and nitrogen jets are nearly equal at 2.2 and 2.5, respectively. Similar results as those found here for the density effect, have been obtained by Michalke for the "hot" circular jet (i.e., for jets where the jet temperature is higher than the ambient temperature, or, in other words, the jet density is less than the ambient density) and by Maslowe & Kelly (1971) for the heated plane shear layer. Their findings indicated that the most amplified disturbance of the hot jet (or layer) occurs at a lower frequency and has a slightly larger growth rate compared to that for the isothermal jet (or shear layer). Heating also reduces the range of unstable frequencies.

Plotted in Figure A.2(a) is the growth rate, $-\alpha_i R$, as a function of the nondimensional wavenumber, $\alpha_r R$, for nitrogen jets at M = 1.3, 2, and 5. The figure shows the same results as Figure A.1 for the nitrogen jet, but the unstable wavenumbers are emphasized. An enlarged view of Figure A.2(a) at small $\alpha_r R$ is given in Figure A.2(b). Again, the stabilizing influence of increasing Mach number is clearly shown by the reduction in the growth rate. The figure also indicates that, for a particular Mach number, there may be more than one growth rate for a given wavenumber. For example, for M = 1.3 at $\alpha_r R = 0.005$, there are three growth rates, 0.0014, 0.12, and 0.1. Each growth rate corresponds to a different type of disturbance. Disturbances may be subsonic or supersonic relative to both the jet and ambient fluids, supersonic relative to the jet but subsonic relative to the ambient fluid, or supersonic relative to the ambient fluid but subsonic relative to the jet. Figure A.3 shows the qualitative distribution of the different types.

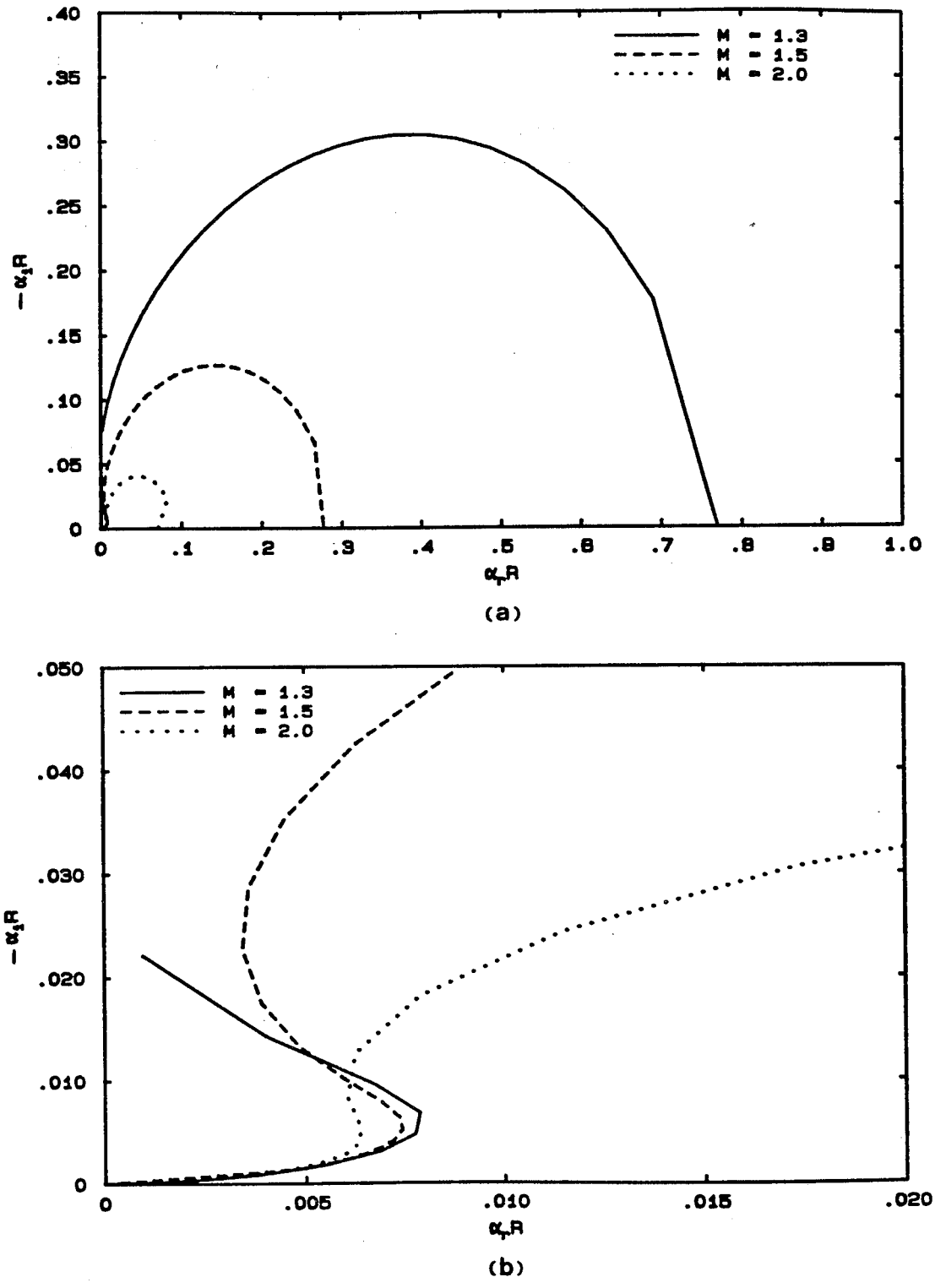

Figure A.2 Spatial stability prediction of amplification rates for nitrogen jet, β = 869.8, mode n=0; (b) is enlarged view at small $\alpha_r R$.

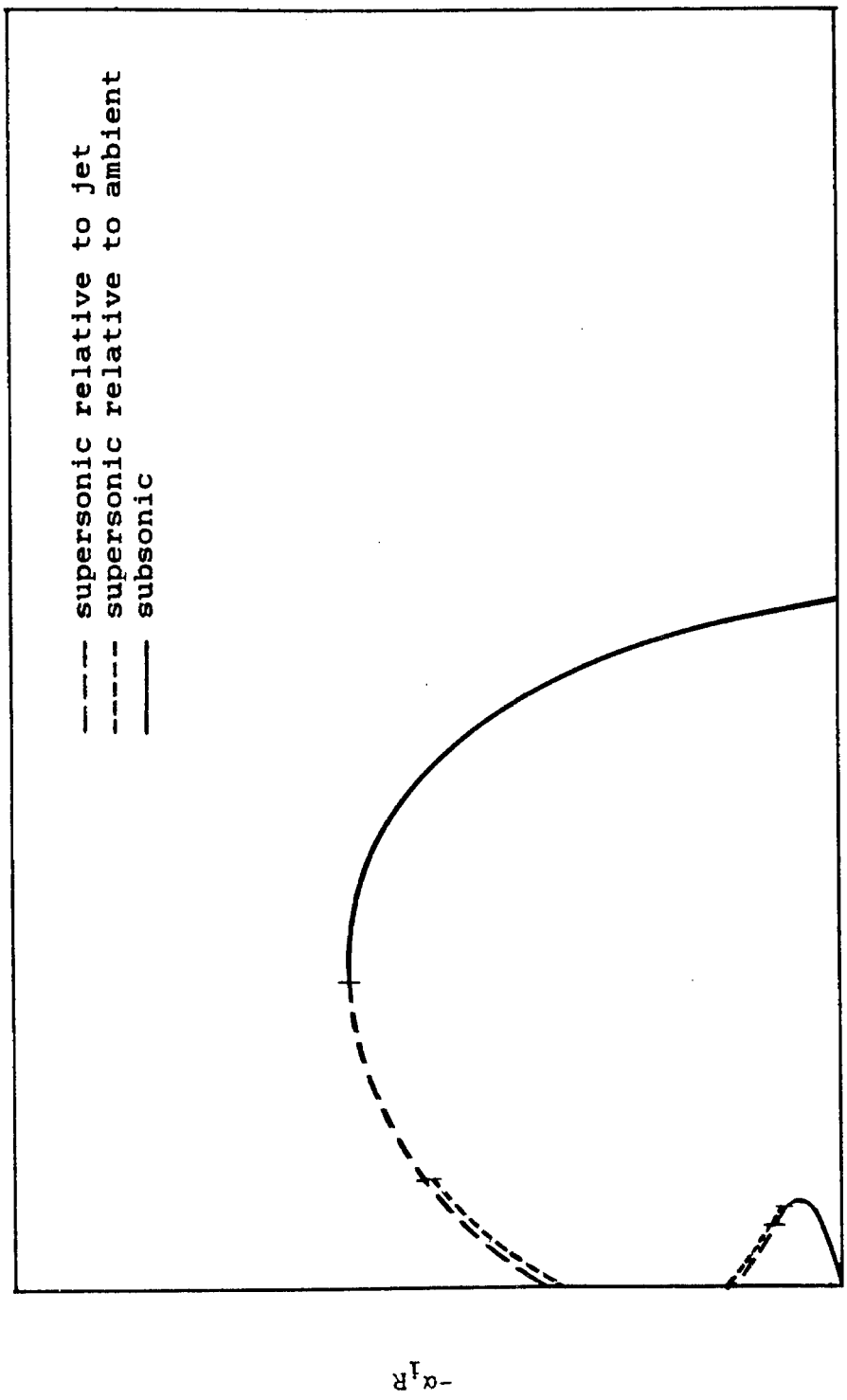

Figure A.3 Qualitative distribution of subsonic and supersonic disturbances.

For comparison with experiment, Figure A.4 shows the nondimensional wavenumber as a function of Mach number. The neutrally stable and the most amplified wavenumbers from theory are indicated; the range of jet pinchoff locations are also given. The experimental values for $\alpha_r R$ were determined from high speed films where the measured locations of the jet pinchoff were assumed to be the half-wavelength of the disturbance. The wavelengths were then converted to nondimensional wavenumbers. Figure A.4 indicates that only a small range of possible unstable wavenumbers was actually observed experimentally. At lower Mach numbers, the experimental values of $\alpha_r R$ are below the predicted most amplified disturbances; at higher Mach numbers, the experimental values are larger than the predicted. For example, at M = 1.2, the most amplified wavenumber is $\alpha_r R = 0.92$; the experiments show $0.24 < \alpha_r R < 0.52$. At M = 2.0, theory predicts $\alpha_r R = 0.6$; experiments show $0.01 < \alpha_r R < 0.24$.

Note the range Mach numbers at which the experimental wavenumbers intersect the neutral stability curve. For example, for the refrigerant-12 jet (Figure A.4(b)), the intersection occurs at M ~ 1.6-1.7. According to Table 4.1, the refrigerant-12 jet is stable when the exit Mach number is increased above 1.75. Indeed, this estimate of M = 1.75 is in good agreement with the theoretical value of 1.6-1.7. However, for the nitrogen, the results do not compare as well. The intersection of the experimental wavenumbers with the neutral stability curve occurs at M ~ 1.4-1.55. Table 4.1 shows nitrogen jet to be stable at exit Mach numbers above 1.86.

Discrepancies between experimental and theoretical results are not unexpected in light of the simplifying assumptions made in the development of the theory. For one, while the stability theory is valid only for small perturbations, the jet collapse and pinchoff phenomenon is obviously nonlinear. Also, it is unlikely that the jet profile remains "top hat." More probable, the profile is parabolic, since in photographs of the developing gas jets, particularly of the lighter jets, a

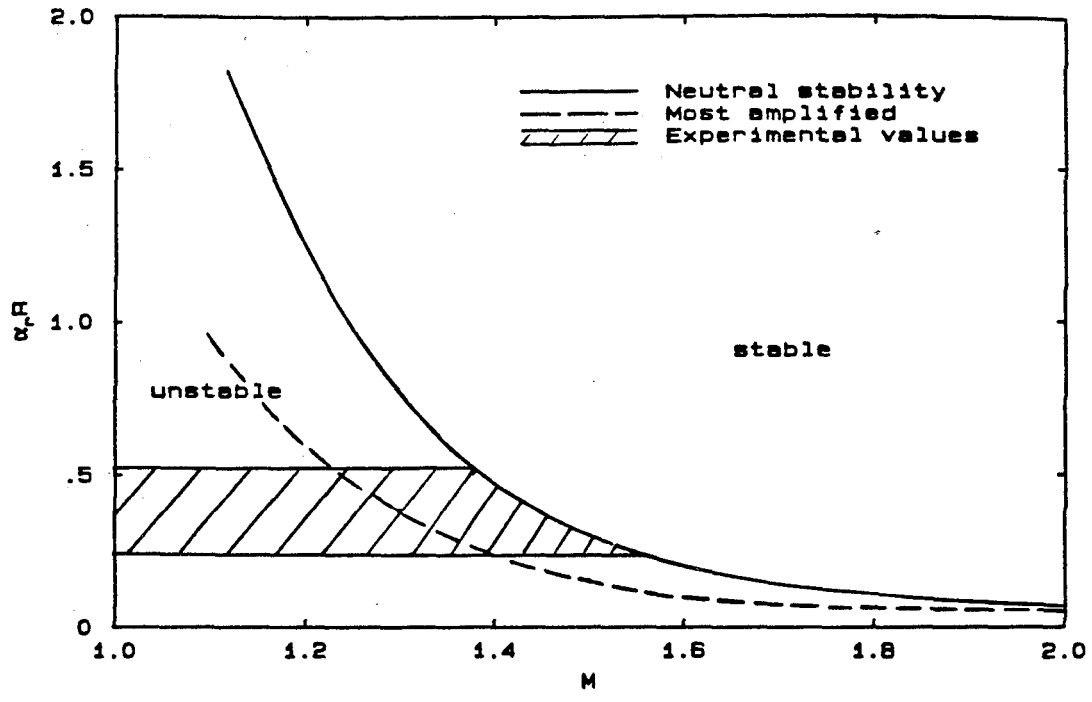

(a)

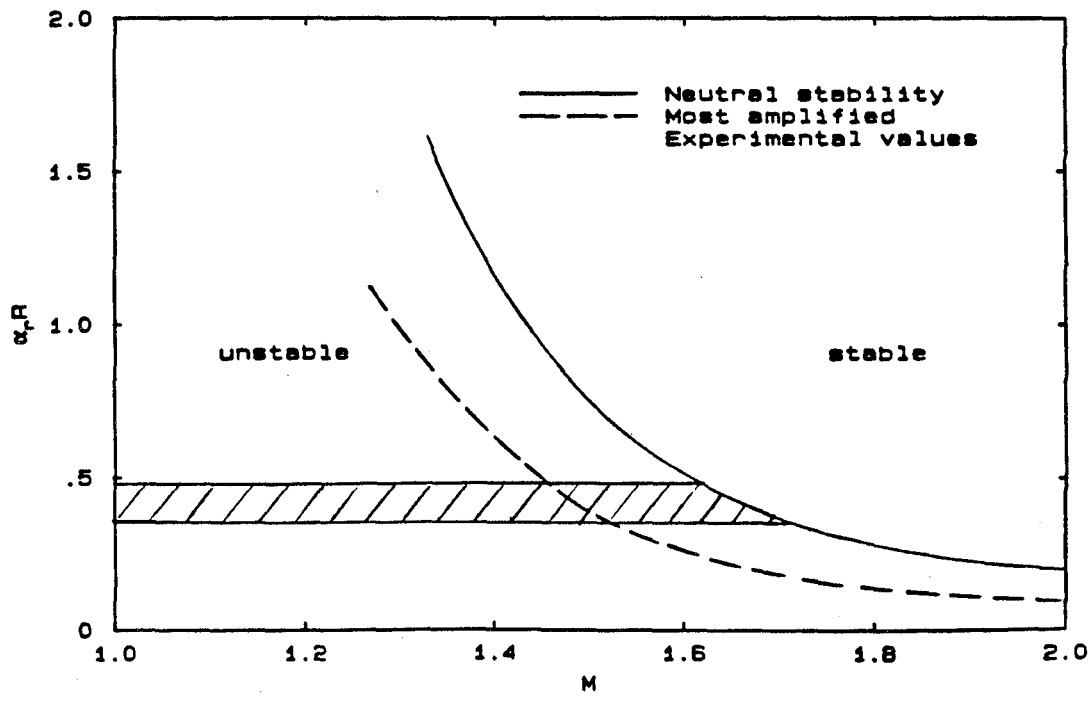

(b)

Figure A.4 Comparison of experimental and theoretical wavenumbers, spatial stability, mode n=0, (a) N2 jet, (b) R12 jet.

wide shearing region is observed between the jet and ambient fluids.

A.2. Temporal Stability.

In addition to the spatial stability, the temporal stability of the compressible vortex sheet was also considered. The eigenvalue equation closely resembles the spatial one except that, in this case, the frequency, c, is complex. The relevant equations are

$$\left[1-\frac{1}{z}\right]^2 = \beta\left[\frac{K_n(\chi\xi_a)I_n'(\chi\xi_j)}{K_n'(\chi\xi_a)I_n(\chi\xi_j)}\right] \tag{A.2a}$$

where

$$\chi = \alpha R,$$

$$z = \frac{c}{U} = \frac{\omega}{\alpha U},$$

$$\xi_j = \left[1-M^2(1-z)^2\right]^{1/2}, \tag{A.2b}$$

$$\xi_a = \left[1-M^2z^2\left[\frac{a_j}{a_a}\right]^2\right]^{1/2}, \tag{A.2c}$$

and

$$c = c_r + ic_i$$

where c_r is the wavespeed and c_i is the amplification rate. Again, Equation (A.2a) shows the normalized frequency, z, as an implicit function of χ. In a similar manner to the spatial case, Newton's method can be used to compute z for each χ. Although both the symmetric (n=0) and antisymmetric (n=1) modes of disturbance were examined, only the results for the symmetric mode is presented here.

Figure A.5 shows the distributions of normalized wavespeed, c_r/U, and amplification rate, c_i/U, as functions of χ for nitrogen and refrigerant-12 jets into water at three different Mach numbers. The combined effect of increasing M and β is to shift the most amplified disturbances to smaller wavenumbers. The figure indicates that, at high Mach numbers, both the nitrogen and refrigerant-12 jets are unstable to a smaller range of disturbance frequencies. In particular, the refrigerant-12 jet is unstable to disturbances of wavenumber less than 0.2 (i.e., wavelengths greater than 15D); nitrogen is unstable to disturbances of wavenumber less than 0.07.

Summarized in Figure A.6 are the wavenumbers of the most amplified disturbances predicted by theory, χ at $(c_i/U)_{max}$, for four different gas jets in water. Listed in the table adjacent to Figure A.6 are the experimental values of $\alpha_r R$. Although quantitatively the most unstable wavenumbers predicted by theory do not compare well with experiment, some qualitative trends appear consistent. Light jets are more unstable than heavier ones, particularly to longer wavelength disturbances. For all jets, increasing the Mach number is stabilizing.

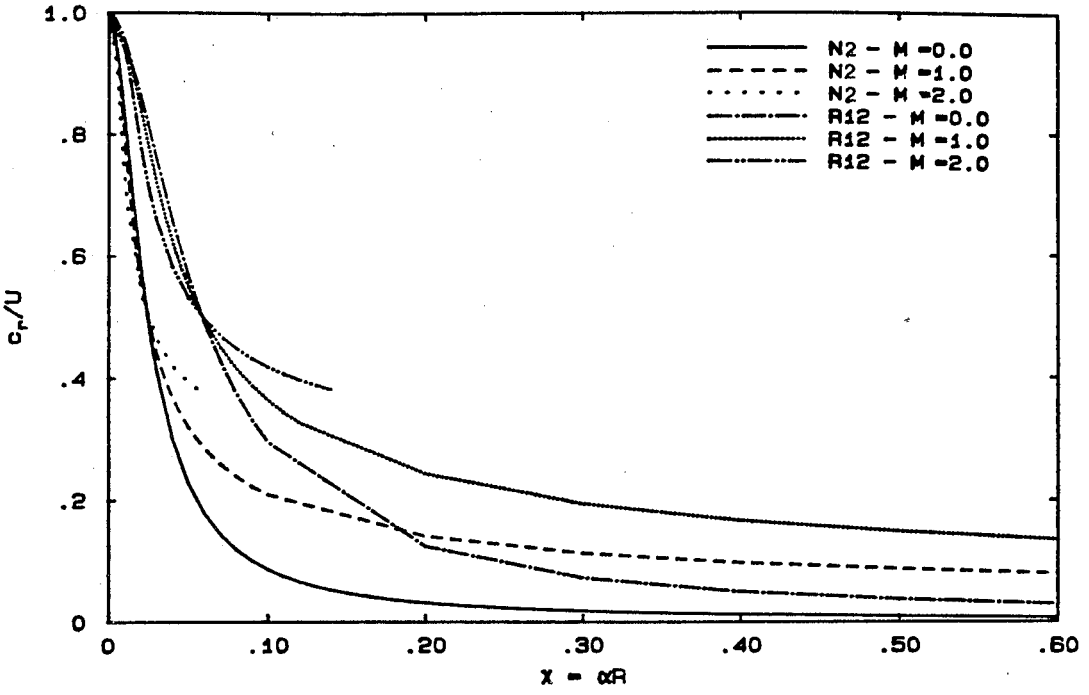

(a)

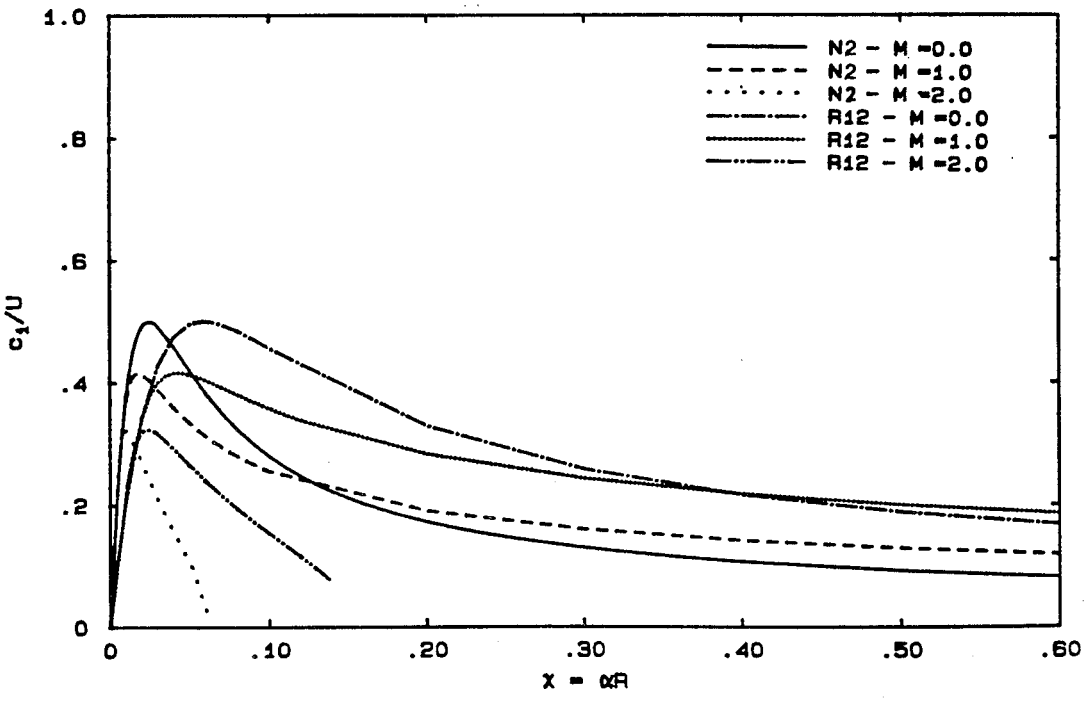

(b)

Figure A.5 Theoretical wavespeeds and amplification rates for N2 and R12 jets, temporal analysis.

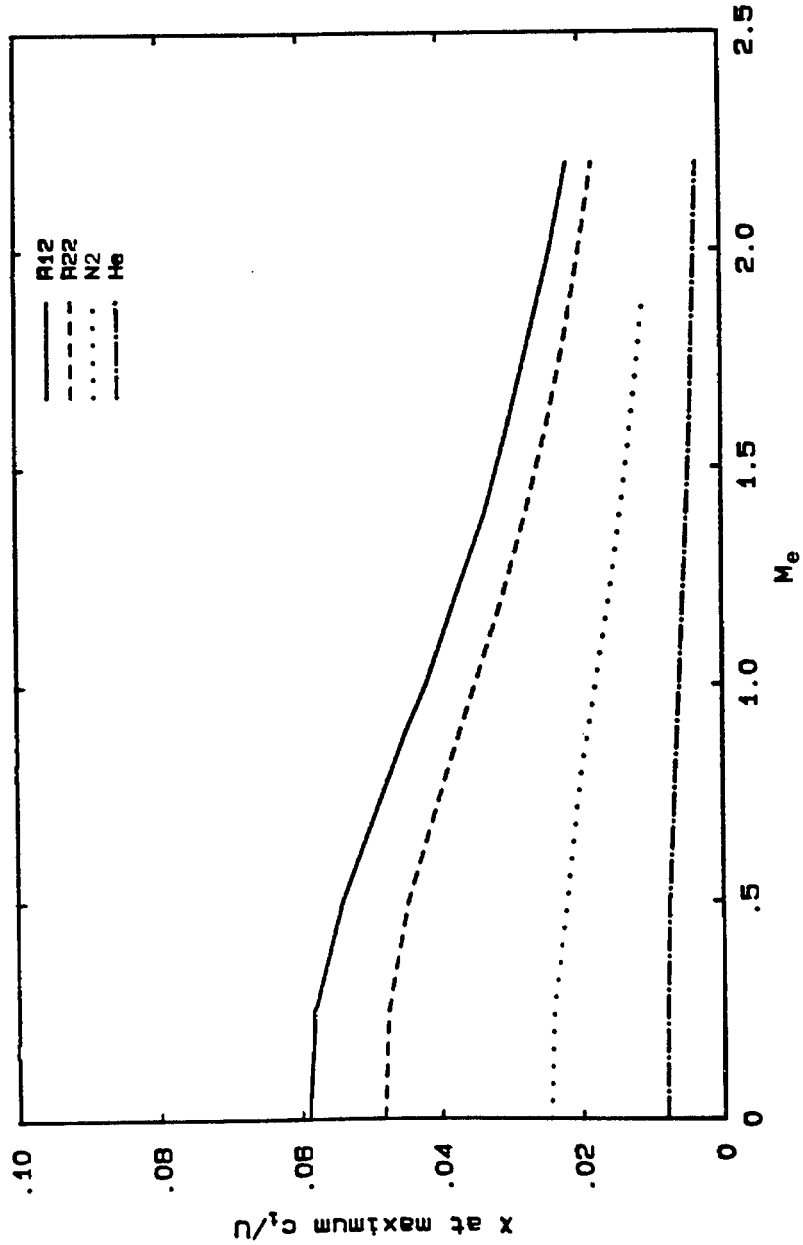

Experimental Values (M=1.0-2.0)	
Gas	X
R12	0.37-0.49
R22	0.29-0.49
N2	0.25-0.53
He	0.18-0.39

Figure A.6 Comparison of most amplified disturbance wavenumbers with exit Mach number.

References

ABRAMOVICH, G. 1963 The Theory of Turbulent Jets , MIT Press, Cambridge, Mass.

AVERY, J.F. & FAETHE, G.M. 1974 Combustion of a submerged gaseous oxidizer jet in a liquid metal. The 15th International Symposium of the Combustion Institute, 501-512.

BATCHELOR, G.K. & GILL, A.E. 1963 Analysis of the stability of axisymmetric jets. J. Fluid Mech., 14, 529-551.

BELL, R., BOYCE, B.E., & COLLIER, J.G. 1972 The structure of a submerged impinging gas jet. British Nuclear Energy Society, 11, 183-193.

BROWN, G. & ROSHKO, A. 1974 On density effects and large structure in turbulent mixing layers. J. Fluid Mech., 64, 775-816.

CALDERBANK, P.H. 1956 Gas-liquid contacting on plates. Trans. Instn. Chem. Engrs., 34, 79-90.

CHANG, I.D. & RUSSELL, P.E. 1965 Stability of a liquid layer adjacent to a high-speed gas stream. Phys. of Fluids, 8, 1018-1026.

CHAWLA, T.C. 1975, The Kelvin-Helmholtz instability of the gas-liquid interface of a sonic gas jet submerged in a liquid. J. Fluid Mech., 67, 513-537.

CHEN, C.J. & RODI, W. 1980 Vertical Turbulent Buoyant Jets - A Review of Experimental Data, Pergamon Press, New York.

CHENG, I.P. 1984 Instability of a gas jet in liquid. Phys. of Fluids, 28, 2614-2616.

COLES, D. 1957 The laminar boundary layer near a sonic throat. Proc. of 1957 Heat Transfer and Fluid Mech. Inst.

GILL, A.E. 1965 Instabilities of "top-hat" jets and wakes in compressible fluid. Phys. of Fluids, 8, 1428-1430.

IGWE, B.U.N., RAMACHANDRAN, S., & FULTON, J.C. 1973 Jet penetration and liquid splash in submerged gas injection. Metallurgical Transactions, 4, 1887-1894.

JACKSON, R. 1964 The formation and coalescence of drops and bubbles in liquids. Chem. Eng., 42, 107-118.

JUNGOWSKI, W.M. 1969 On the flow in a sudden enlargement of a duct. Fluid Dynamics Transactions, 4, 231-241.

JUNGOWSKI, W.M. 1978 Some self induced supersonic flow oscillations. Prog. Aerospace Sci., 18, 151-175.

KERNEY, P.J., FAETHE, G.M., & OLSON, D.R. 1972 Penetration characteristics of a submerged jet. A.I.Ch.E. Journal, 18, 548-553.

KICENIUK, T. 1952 A preliminary investigation of the behavior of condensable jets discharged into water. CIT Report No. E-24.6.

KOVASZNAY, L.S.G., KIBENS, V., & BLACKWELDER, R.F. 1970 Large-scale motion in the intermittent region of a turbulent boundary layer. J. Fluid Mech., 41, 283-325.

LEIBSON, I., HOLCOMB, E.G., CASOSO, A.G., & JACMIC, J.J. 1956 Rate of flow and mechanics of bubble formation from single submerged orifices. A.I.Ch.E. Journal, 2, 296-306.

LESSEN, M., FOX, J.A., & ZIEN, H.M. 1965 The instability of inviscid jets and wakes in compressible fluid. J. Fluid Mech.,21, 129-143.

MASLOWE, S.A. & KELLY, R.E. 1971 Inviscid instability of an unbounded heterogeneous shear layer. J. Fluid Mech., 65, 405-415.

MATTINGLY, G.E. & CHANG, C.C. 1974 Unstable wave on an axisymmetric jet column. J. Fluid Mech., 23, 541-560.

MICHALKE, A. 1970 A note on the spatial jet-instability of the compressible cylindrical vortex sheet. Deutsche Luft- und Raumfahrt, DLR-FB 70-51.

MICHALKE, A. 1977 Instability of a compressible circular free jet with consideration of the influence of the jet boundary layer thickness. English translation NASA Tech. Memo. 75190.

MICHALKE, A. 1984 Survey on jet instability theory. Prog. Aerospace Sci., 21, 159-199.

MORTON, B.R. 1965 Modeling fire plumes. The 10th International Symposium of the Combustion Institute, 973-932.

PLESSET, M.S. & PROSPERETTI, A. 1977 Bubble dynamics and cavitation. Ann. Rev. Fluid Mech., 7, 145-185.

RAYLEIGH, S.L. 1892 On the instability of cylindrical fluid surfaces. Phil. Mag.

RICOU, F.P. & SPALDING, D.B. 1961 Measurements of entrainment by axisymmetrical turbulent jets. J. Fluid Mech., 11, 21-32.

SQUIRE, H.B. & TROUNCER, J. 1944 Round jets in a general stream. Aeronautical Research Committee; Reports and Memoranda, No. 1404.

THEMELIS, N.J., TARASSOFF, P., & SZEKELY, J. 1969 Gas-liquid momentum transfer in a copper converter. Trans. Metallurgical Society of AIME, 245, 2425-2433.

TOMBACH, L.H. 1969 Velocity measurements with a new probe in inhomogeneous turbulent jets. Ph.D. Thesis, Caltech.

TROSS, S.R. 1974 Characteristics of a turbulent two-phase, submerged, free jet. M.S. Thesis, The Pennsylvania State University.

WATSON, J. 1962 On spatially-growing finite disturbances in a plane Poiseuille flow. J. Fluid Mech., 14, 211-221.

WITCZAK, K.J. 1977 Self-excited oscillations. Nonlinear Vibration Problems, 18, 146-206.

WHITE, F.M. 1974 Viscous Fluid Flow, McGraw-Hill, New York.

ZAK, M., KENDALL, J., & WANG, T. 1984 private communication.